TECHNISCHE UNIVERSITÄT MÜNCHEN

Lehrstuhl E23 für Technische Physik

Walther-Meißner-Institut für Tieftemperaturforschung
der Bayerischen Akademie der Wissenschaften

Gradiometric tunable-gap flux qubits in a circuit QED architecture

Manuel Johannes Schwarz

Vollständiger Abdruck der von der Fakultät für Physik der Technischen Universität München zur Erlangung des akademischen Grades eines

Doktors der Naturwissenschaften

genehmigten Dissertation.

Vorsitzender:	Univ.-Prof. Dr. M. Zacharias
Prüfer der Dissertation:	1. Univ.-Prof. Dr. R. Gross
	2. Univ.-Prof. J. J. Finley, Ph.D.

Die Dissertation wurde am 10.11.2014 bei der Technischen Universität München eingereicht und durch die Fakultät für Physik am 03.02.2015 angenommen.

Contents

Chapter 1

Introduction

'The first commercial quantum computer' sold by the Canadian company *D-Wave Systems Inc.*, attracted a lot of attention among scientists as well as among a broader public in recent years. From the beginning, however, quantum physicists doubted, whether this special type of a quantum annealer [1] could compete with their vision of a universal quantum computer [2], or whether this device is *quantum* at all [3]. As it turns out, skeptics seem to be right after all, as no quantum speedup of the D-Wave device compared to conventional computers has been demonstrated so far [4]. Nevertheless, the success of D-Wave Systems in selling several of their devices can be considered an incentive for the research towards a working universal quantum computer. Before the latter will be realized, a lot of progress needs to be made [5], also concerning its basic building block, the quantum bit (qubit). The physical system used by D-Wave is a specific type of superconducting flux qubit. The comparably poor coherence properties of these qubits are in fact not so detrimental to quantum annealing. For the much more promising universal quantum computer, however, good coherence properties are of great importance. The refinement of (another version of) a flux qubit in this respect is the essence of this thesis. Although our work is motivated rather by experiments on fundamental light-matter interaction [6] or quantum simulations [7–9] than by the challenging, long-term task of building a quantum computer, the basic requirements on qubits are essentially the same: combining large in situ tunability with sufficient qubit coherence time. The gradiometric tunable-gap flux qubit constitutes one step in this direction.

The persistent current flux qubit is one example of a superconducting quantum circuit, whose main characteristic is macroscopic quantum coherence: Although macroscopic in size, containing many billions of atoms, these systems have discrete energy levels, resulting in experimentally observable phenomena such as macroscopic quantum tunneling [10]. Due to the existence of discrete quantum states just as for electronic states in atoms, we can refer to these quantum circuits as *artificial atoms*. In particular, a quantum two-level system – a qubit – can be realized when the two lowest energy levels are well separated from higher levels due to the presence of a strong nonlinearity causing an anharmonic

potential. For superconducting circuits, this task is taken over by the Josephson junction (JJ).

This nonlinear tunnelling junction is the common ingredient of several types of Josephson qubits. The most popular superconducting qubits are the Cooper pair box [6, 11], the transmon qubit [12–14], the phase qubit [15–17], the fluxonium [18], and the persistent current or flux qubit [19–22]. The coupling of these qubits to linear quantum systems, such as superconducting resonators, has been particularly fruitful, leading to the rapid development of the prospering field of circuit quantum electrodynamics (QED). The name circuit QED was coined, because, there, artificial atoms formed by electronic circuits replace the natural atoms in cavity QED systems.

In general, circuit QED systems benefit from their high degree of tunability, both in situ and by fabrication, and from the large achievable coupling strength. More precisely, the combination of high electromagnetic field strength (small mode volume) inside quasi-1D transmission line resonators and the large magnetic or electric dipole moments of the macroscopic superconducting qubits allows us to reach the interesting strong coupling regime straightforwardly. In this regime, the coupling strength is larger than all decoherence rates, and a coherent exchange of excitations between qubit and resonator becomes observable [23]. Circuit QED systems were also used, for example, to generate non-classical states of light [12, 15], to establish single artificial atom masing [24], to realize controlled symmetry breaking [25, 26], or to demonstrate quantum teleportation [27], quantum gates [13, 28] and quantum computing protocols [29–31].

For the implementation of circuit QED experiments, mostly transmon and phase qubits were used for the following reasons. First, the relevant qubit parameters can be controlled within sufficiently narrow margins in the fabrication process. Second, a controlled coupling/decoupling to a microwave resonator acting as a quantum bus is possible by a fast change of the qubit transition frequency. Third, the coherence properties of the qubit do not strongly degrade during such operations. Unfortunately, the original design of the persistent current flux qubit [20] consisting of a superconducting loop intersected by three Josephson junctions cannot fulfill these requirements simultaneously. First, although the flux qubit transition frequency ω_q can be varied over a wide range by applying an external magnetic flux, the coherence time of the flux qubit rapidly decreases when tuning the qubit away from a particularly favorable operating point, the so-called degeneracy point, with minimum transition frequency $\omega_\mathrm{q} = \Delta$, the qubit gap. Only at this point, the flux qubit is well protected from the relevant $1/f$-noise and coherence times exceeding $1\,\mu\mathrm{s}$ can be reached [32, 33]. Second, for the flux qubit the minimal energy splitting $\hbar\Delta$ between the ground and excited state depends exponentially on the critical current and capacitance of the Josephson junctions [22] and therefore is difficult to precisely control in fabrication. This does not allow to control the point of optimum coherence

to a sufficient degree during fabrication. On the other hand, flux qubits have specific advantages. First, their anharmonicity, that is, the separation between the qubit states and the third level, is by one or two orders of magnitude larger than for transmon and phase qubits. This property allows for fast qubit operations without leakage to higher states. Second, flux qubits can be coupled ultrastrongly to resonators. Relative coupling strengths $g/\omega_\mathrm{r} > 0.1$, where ω_r is the resonator frequency and g the coupling strength, were successfully demonstrated [34–36].

In order to overcome the drawback of the fixed minimum energy splitting in superconducting flux qubits, Orlando *et al.* [22] proposed a modified design, which subsequently has been implemented by Paauw *et al.* [37] and meanwhile successfully used in several experiments, either in gradiometric [33, 37, 38] or non-gradiometric design [39–42]. In this *tunable-gap* flux qubit one of the Josephson junctions, the so-called α-junction, is replaced by a small loop with two Josephson junctions. This dc superconducting quantum interference device (SQUID) acts as a junction whose critical current can be controlled *in situ* by the flux threading the SQUID loop. As a consequence, also the qubit gap Δ can be tuned in such a configuration. The additional control allows for a fast variation of the qubit transition frequency, while still operating the flux qubit at its degeneracy point [33, 37, 38]. In this manner, a tunable-gap flux qubit was coupled to a lumped-element LC resonator [33, 35] and to an ensemble of electron spins in diamond [42].

This thesis presents the realization of a tunable-gap qubit in a gradiometric design and the first integration of such a qubit into a circuit QED environment by coupling it to a superconducting transmission line resonator.

Thesis outline

A summary of the fundamental theory relevant for superconducting circuits is given in Chapter 2, including a description of the Josephson junction, the dc SQUID and the superconducting resonator. Then, we introduce the persistent current flux qubit in Chapter 3. We explain the details of a tunable gap and of the gradiometric design. Also, we combine flux qubit and superconducting resonator in the description of circuit QED. With this theoretic background, we turn to the experimental techniques in Chapter 4, presenting our methods for sample pre-characterization and the setups for the measurements of the two following chapters. Chapter 5 deals with the flux qubit alone. We characterize the stepwise evolution from a standard non-tunable flux qubit to a gradiometric version and to the gradiometric tunable-gap qubit. In Chapter 6, we couple the gradiometric tunable-gap qubit to a transmission line resonator. In particular, we analyze the qubit-resonator coupling and investigate the tunability of the qubit gap with respect to the resonator. After summarizing the results of this thesis, we give an outlook

on future experiments with gradiometric tunable-gap flux qubits in Chapter 7.

Chapter 2

Basics of superconducting quantum circuits

This chapter is aimed at introducing the superconducting quantum circuits used in this work and at recapitulating some basic physical concepts necessary to understand these systems. Why do we use superconducting circuits in order to investigate quantum physics despite the need to cool these systems to low temperatures? The answer is found in some unique benefits of superconducting materials stemming from the quantum mechanical nature of superconductors. On the one hand, superconductors possess an energy gap, protecting their ground state from electronic excitations, they obey flux quantization and can have a significant kinetic inductance. On the other hand, superconductors allow for the formation of Josephson junctions, whose nonlinear properties make them unique quantum devices. For a conclusive description, we start with the macroscopic quantum model of superconductivity in Sec. 2.1, leading to the phenomenon of flux quantization in Sec. 2.2, where we also discuss the influence of kinetic inductance. In Sec. 2.3 the physics of a Josephson junctions is introduced, followed by a description of the dc superconducting quantum interference device (SQUID) in Sec. 2.4. After that we continue with the quantum mechanical description of superconducting circuits in Sec. 2.5 and explain as first example superconducting transmission line resonators in Sec. 2.6.

2.1 The macroscopic quantum model of superconductivity

The BCS theory [43, 44] constitutes a groundbreaking microscopic explanation of superconductivity in metals and has also verified the phenomenological macroscopic quantum model of superconductivity. The latter is very adequate to describe flux quantization and the Josephson effect in the following sections. The macroscopic quantum model is based on the one main assumption that the ensemble of Cooper pairs forming the super-

conducting state can be described by one space- and time-dependent macroscopic wave function

$$\Psi(\mathbf{r},t) = \sqrt{n_\mathrm{s}(\mathbf{r},t)} \cdot e^{i\theta(\mathbf{r},t)}, \tag{2.1}$$

where the density of Cooper-pairs $n_\mathrm{s}(\mathbf{r},t)$ provides normalization and $\theta(\mathbf{r},t)$ is the macroscopic phase of the wave function. Using some basic relations of quantum mechanics and electrodynamics such as Schrödinger and continuity equation, the quantum mechanical supercurrent density

$$\mathbf{J}_\mathrm{s} = \frac{q_\mathrm{s}\hbar}{2m_\mathrm{s}i}\left(\Psi^*\nabla\Psi - \Psi\nabla\Psi^*\right) - \frac{q_\mathrm{s}^2}{m_\mathrm{s}}\Psi\Psi^*\mathbf{A}, \tag{2.2}$$

can be deduced. Here, $q_\mathrm{s} = -2e$ and $m_\mathrm{s} = 2m_\mathrm{e}$ are charge and mass, respectively, of a Cooper pair, e is the elementary charge and m_e the electron mass. $\mathbf{A}$ denotes the magnetic vector potential linked with the magnetic flux density $\mathbf{B} = \nabla \times \mathbf{A}$. Applying the macroscopic wave function from Eq. (2.1) to the supercurrent density of Eq. (2.2) yields

$$\mathbf{J}_\mathrm{s}(\mathbf{r},t) = \frac{\hbar q_\mathrm{s} n_\mathrm{s}(\mathbf{r},t)}{m_\mathrm{s}} \underbrace{\left\{\nabla\theta(\mathbf{r},t) - \frac{q_\mathrm{s}}{\hbar}\mathbf{A}(\mathbf{r},t)\right\}}_{\equiv\gamma} \tag{2.3}$$

with the gauge invariant phase difference γ. With this expression, one can easily deduce the London equations for the case $n_\mathrm{s} = \mathrm{const}$ and thus explain the two fundamental footprints of superconductivity, namely the vanishing electrical resistance and the Meissner-Ochsenfeld effect. Moreover, and more relevant for this work, the macroscopic quantum model allows for the formal description of flux/fluxoid quantization.

2.2 Fluxoid quantization

Based on the quantum coherent properties of the superconducting state as discussed above, a formal consideration results in the quantization of the magnetic flux inside multiply connected superconductors. This has first been proposed by London and then experimentally been proved by Doll and Näbauer at WMI [45] and, independently, by Deaver and Fairbanks [46]. Since the quantitative analysis of these experiments involves a superconducting charge $q_\mathrm{s} = -2e$, they constitute the first proof of the existence of Cooper pairs, which are one main ingredient of the BCS theory. Besides this importance of flux quantization for the progress of the theory of superconductivity, it is also of great practical relevance for loop-shaped devices such as SQUIDs and, especially, the gradiometric qubits studied in this work. The latter not only underly flux quantization but actively make use of it to trap magnetic flux quanta for a magnetic bias. Equivalently to the microscopic description of electronic states in atoms leading to the quantization of the

electrons' angular momentum, the macroscopic wave function of a superconductor needs to interfere constructively along a closed contour which leads to flux quantization for multiply connected superconductors as shown in Fig. 2.1**a**. In this toroidal superconductor two examples for stationary wave functions (black and red lines) are depicted.

Formally, flux quantization becomes evident when integrating the supercurrent density of Eq. (2.3) along a closed contour C (represented also by the black line in Fig. 2.1**a**). Introducing the London coefficient

$$\Lambda = m_\mathrm{s} / \left(n_\mathrm{s} q_\mathrm{s}^2\right) = \mu_0 \lambda_\mathrm{L}^2, \tag{2.4}$$

which is also linked to the London penetration depth λ_L , the path integral reads

$$\oint_C \Lambda \mathbf{J}_\mathrm{s}(\mathbf{r},t) \cdot \mathrm{d}\mathbf{l} + \oint_C \mathbf{A}(\mathbf{r},t) \cdot \mathrm{d}\mathbf{l} = \frac{\hbar}{q_\mathrm{s}} \oint_C \nabla\theta(\mathbf{r},t) \cdot \mathrm{d}\mathbf{l}. \tag{2.5}$$

The second integral on the left hand side can be evaluated using Stoke's theorem to

$$\oint_C \mathbf{A}(\mathbf{r},t) \cdot \mathrm{d}\mathbf{l} = \int_F \mathbf{B} \cdot \mathrm{d}\mathbf{F} = \Phi$$

with the magnetic flux Φ penetrating the area F enclosed by the contour C. The path integral on the right hand side of Eq. (2.5) over the gradient of the scalar θ is not zero, as the macroscopic phase θ of the same start and end point are not necessarily the same. In fact, the macroscopic phase can take an infinite number of values

$$\theta(\mathbf{r},t) = \theta_0(\mathbf{r},t) + 2\pi n, \qquad n \in \mathbb{Z}\,. \tag{2.6}$$

and still fulfills the necessary uniqueness of the wave function of Eq. (2.1). Finally, the integral of Eq. (2.5) leads to

$$\oint_C \Lambda \mathbf{J}_\mathrm{s}(\mathbf{r},t) \cdot \mathrm{d}\mathbf{l} + \int_F \mathbf{B} \cdot \mathrm{d}\mathbf{F} = \frac{\hbar}{q_\mathrm{s}} 2\pi n = n\,\Phi_0, \tag{2.7}$$

which expresses the quantization of the so called fluxoid [left hand side of Eq. (2.7)] in terms of the magnetic flux quantum $\Phi_0 \equiv \frac{h}{2e} = 2.067833758(46) \times 10^{-15}\,\mathrm{Vs}$. This very general expression Eq. (2.7) also includes the case of simply connected shapes of superconductors such as solid cylinders or spheres. Then, the contour C and area F can become infinitesimally small and the integrals in Eq. (2.7) vanish, approving that there is no fluxoid quantization in simply connected superconductors. For multiply connected shapes, the integrals in Eq. (2.7) are in general non-zero and the quantization condition holds. However, there are two cases that need to be distinguished: flux quantization and fluxoid quantization.

Flux quantization

If the dimensions of the multiply connected superconductor are large compared to the London penetration depth, e.g., in a hollow cylinder with sufficient wall thickness, the whole integration path C can be located in the field- and current-free region of the material. Then, the integral over the supercurrent density $\mathbf{J}_\mathrm{s}$ in Eq. (2.7) is zero leading to the flux quantization condition

$$\int_F \mathbf{B} \cdot \mathrm{d}\mathbf{F} = \Phi = n\,\Phi_0. \tag{2.8}$$

This flux quantization is observed when applying a magnetic flux before cooling the superconductor below the critical temperature. In the superconducting state the resulting flux is always quantized according to Eq. (2.8), which is the essence of these first experiments by Doll/Näbauer and Deaver/Fairbanks.

Fluxoid quantization

However, for the nanoscale superconducting devices used in this work, dimensions fall below the London penetration depth of the material. Our aluminum films are less than one hundred nanometers thick, whereas the penetration depth is several hundred nanometers [47, 48]. Then, the finite supercurrent density contributes to the integral in Eq. (2.7) and not the flux alone, but the fluxoid is quantized. In other words, the quantized fluxoid consists of the total magnetic flux

$$\Phi = \Phi_\mathrm{ex} + \Phi_\mathrm{g} + \Phi_\mathrm{k} \tag{2.9}$$

composed of the flux Φ_ex due to external magnetic field and the flux Φ_g induced by the circulating current I associated with a magnetic field and a part Φ_k generated by the charge carriers of the supercurrent. These two latter parts are also linked to the geometric and the kinetic inductance.

Kinetic inductance

A superconductor not only comes with a geometric inductance but also with kinetic inductance. The common geometric inductance L_g is related to the magnetic field energy $E_\mathrm{mag} = \frac{1}{2} L_g I^2$ of a conductor with electrical current I and induces a magnetic flux $\Phi_\mathrm{g} = L_\mathrm{g} I$. However, the charge carriers also have a kinetic energy $E_\mathrm{kin} = \frac{1}{2} N_\mathrm{s} m_\mathrm{s} v^2 = \frac{1}{2} L_k I^2$, where N_s and v are the number and mean velocity of the charge carriers and L_k is the kinetic inductance. The latter is also linked to the London coefficient in Eq. (2.4) and

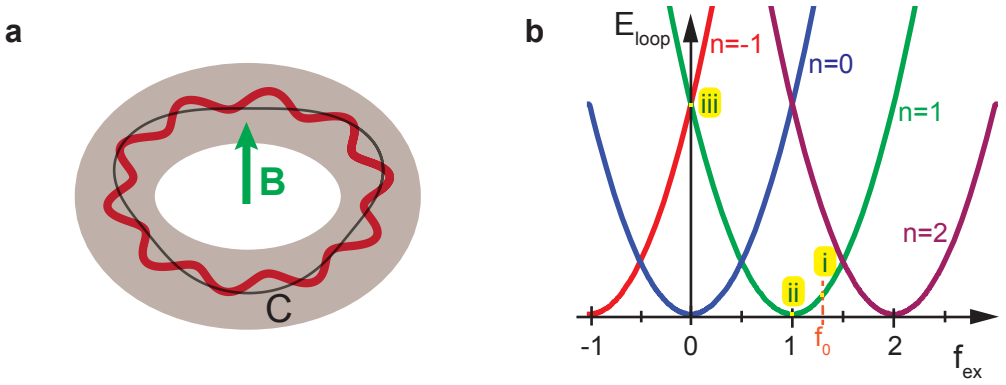

Figure 2.1: **a** Sketch illustrating fluxoid quantization in a multiply connected superconductor. Red and black lines represent constructively interfering macroscopic wave functions. **b** Energy consideration of flux trapping: In the normal-conducting state a frustration f_0 is applied (i). After cooling below the critical temperature energy is minimized by trapping an integer number of flux quanta, in this example $n_0 = 1$ (ii). With the removal of the external magnetic field the loop energy increases (iii).

the first term of Eq. (2.7) via

$$\oint_\Gamma \Lambda \mathbf{J}_s \cdot \mathrm{d}\mathbf{s} = \frac{\Lambda s}{A} I = L_\mathrm{k} I \equiv \Phi_\mathrm{k} \,, \tag{2.10}$$

where s and A denote length and cross-sectional area of the conductor, respectively.

For normal metals the effect of kinetic inductance can be neglected (except for high frequency ac currents) due to the high scattering rate of the charge carriers. However, for the dissipation-free dc currents in superconductors the kinetic inductance can become significant and even exceed the geometric inductance. From Eq. (2.10) it is obvious that the kinetic inductance increases with decreasing cross-sectional area of the conductor; therefore kinetic inductance is relevant for our aluminum wires with dimensions of only a few hundreds of nanometers. With this knowledge on kinetic and geometric inductance we can now evaluate Eq. (2.7) to

$$\underbrace{2\pi \frac{L_\mathrm{k} I}{\Phi_0}}_{\phi_\mathrm{k}} + \underbrace{2\pi \frac{L_\mathrm{g} I}{\Phi_0}}_{\phi_\mathrm{g}} + 2\pi \underbrace{\frac{\Phi_\mathrm{ex}}{\Phi_0}}_{f_\mathrm{ex}} = 2\pi n \,, \tag{2.11}$$

where the right hand side is the phase difference of Eq. (2.6). Therefore we can also define two terms on the left hand side as a kinetic phase difference ϕ_k and a geometric phase difference ϕ_g. Also, the magnetic frustration $f_\mathrm{ex} = \frac{\Phi_\mathrm{ex}}{\Phi_0}$ of the superconducting loop is introduced. It is discussed in more details in Sec. 3.3.2 that the ratio between geometric and kinetic inductance determines how much magnetic flux can penetrate a superconducting loop. Note that with negligible kinetic inductance, the induced flux always compensates a change in the external flux, meaning that we cannot adjust the

total flux inside the loop at will. Therefore a more detailed understanding of the relative size of kinetic and geometric inductance is of great practical importance for our flux based devices.

Energy consideration of flux trapping

As explained above, a superconducting ring with a circulating current I possesses both a potential energy linked with the geometric inductance and a kinetic energy linked with the kinetic inductance. In total, the energy of the loop reads

$$E_{\mathrm{loop}} = \frac{1}{2}(L_{\mathrm{k}} + L_{\mathrm{g}})I^2 = \frac{\Phi_0^2}{2(L_{\mathrm{k}} + L_{\mathrm{g}})}(f_{\mathrm{ex}} - n)^2, \tag{2.12}$$

where Eq. (2.11) is used to eliminate the current I. With this energy the trapping of magnetic flux can be illustrated in Fig. 2.1**b**. First a magnetic frustration $f_{\mathrm{ex}} = f_0$ is applied to the normal conducting loop. When cooling it to the superconducting state, a circulating current is induced to fulfill fluxoid quantization. Owing to energy minimization the induced current is such that the number of flux quanta n takes the integer value n_0 closest [1] to f_0. After removing the external frustration, the loop keeps the state of n_0 trapped flux quanta and its energy is higher due to the circulating current generating n_0 flux quanta. A change of n in the superconducting state is, in principle, also possible. Such a phase slip process is inhibited by an energy barrier $E_{\Delta \mathrm{n}} = I_{\mathrm{c,w}}\Phi_0$ [49–51], where $I_{\mathrm{c,w}}$ is the critical current of the wire. However, with a critical current on the order of 1 mA, the energy barrier corresponds to a temperature $T_{\mathrm{slip}} > 10\,000$ K. This condition makes a phase slip very unlikely.

2.3 The Josephson junction

The Josephson junction (JJ) is the most fundamental building block of superconducting quantum circuits due to its nonlinear nature. It is named after Brian D. Josephson who first described the physics of such a junction theoretically [52]. A JJ consists of two superconducting electrodes separated by a normal conducting or insulating layer. If this barrier is thin enough (i.e., several nanometers), Cooper pairs can tunnel through this layer. Although this Cooper pair tunnelling seems very unlikely from a statistical point of view, it is as likely as single electron tunnelling due to the quantum coherent properties of the superconducting state. In other words, the macroscopic wave functions of the two electrodes overlap in the region of the barrier and thus enable a tunnelling current of the superconducting carriers.

[1] To achieve a trapping of n_0 flux quanta, f_0 needs to fulfill $|f_0 - n_0| < 0.5$.

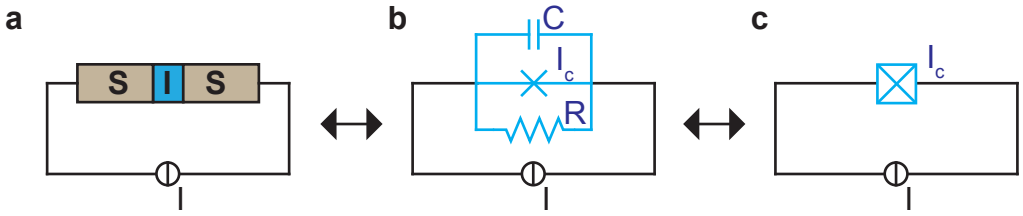

Figure 2.2: **a** Schematic of a Josephson junction (JJ) consisting of two superconductors (S) separated by a thin insulating layer (I). **b** Equivalent circuit of a JJ within the RCSJ model. **c** Simplified wiring symbol of a JJ.

2.3.1 Josephson equations

It can be derived from Eq. (2.3), that the dc supercurrent I_s through a JJ is then given by the first Josephson equation,

$$I_\mathrm{s} = I_\mathrm{c} \sin\phi, \tag{2.13}$$

where ϕ denotes the gauge invariant phase difference between the two superconductors [i.e., the path integral of the gauge invariant phase gradient of Eq. (2.3)]. I_c is the maximum supercurrent that can be reached by tunnelling of Cooper pairs only. Above I_c, also single electrons contribute to the current through the junction, which causes a voltage drop, which is described by the second Josephson equation,

$$\frac{\partial\phi}{\partial t} = \frac{2\pi}{\Phi_0} V, \tag{2.14}$$

linking the time evolution of the phase difference with the voltage drop V. Integrating this equation over time and inserting it into Eq. (2.13) yields an ac supercurrent

$$I_\mathrm{s} = I_\mathrm{c} \sin(2\pi \frac{V}{\Phi_0} t + c') \tag{2.15}$$

through the junction with frequency $\nu = \frac{V}{\Phi_0}$ and an integration constant c'.

2.3.2 Josephson inductance

Evaluating the time derivative of the first Josephson equation, Eq. (2.13), and inserting the second one, Eq. (2.14), yields

$$\frac{dI_\mathrm{s}}{dt} = I_\mathrm{c} \cos\phi \cdot \frac{2\pi}{\Phi_0} V, \tag{2.16}$$

which makes evident that the JJ can be assigned a nonlinear inductance

$$L_\mathrm{J} = \frac{\Phi_0}{2\pi I_\mathrm{c} \cos\phi}. \tag{2.17}$$

This Josephson inductance is unique in the sense that it can take, depending on ϕ, also negative values, which causes the oscillating supercurrent at a constant voltage drop as discussed above. Yet, it is of more general importance that the strong nonlinearity of the Josephson inductance is an essential property for the formation of qubits consisting of superconducting circuits containing JJs. Moreover, it must be noted that the Josephson inductance for the devices of this work is typically on the order of a few nanohenry (example: $I_\mathrm{c} = 1\,\mu\mathrm{A} \Rightarrow L_\mathrm{J} \gtrsim 0.3\,\mathrm{nH}$) and thus dominates the total inductance ($L_\mathrm{k} + L_\mathrm{g} \simeq 10\,\mathrm{pH}$) of the superconducting lines connected to the JJ. Since – from an electrotechnical point of view – an inductance usually allows for the storage of energy, we consider the characteristic energies of a JJ next.

2.3.3 Characteristic energy scales

The energy linked with the Josephson inductance is the Josephson coupling energy E_J. It can be interpreted as the binding energy between two weakly coupled superconductors similar to the coupling of two atoms to a molecule. Although a JJ causes no direct energy dissipation in the zero-voltage state, energy is needed to accelerate the superconducting charges. Therefore, a finite voltage is supplied by an external current source, which is typically connected to a JJ. The potential energy of a JJ is thus the electrical power supplied by the external source integrated over time and reads

$$U(\phi) = \int_0^{t'} V I_\mathrm{s} \cdot \mathrm{d}t = \int_0^{t'} \frac{\Phi_0}{2\pi} \frac{\mathrm{d}\phi}{\mathrm{d}t} I_\mathrm{c} \sin\phi \cdot \mathrm{d}t = \frac{\Phi_0 I_\mathrm{c}}{2\pi} \int_0^{\phi(t')} \sin\phi \cdot \mathrm{d}\phi \tag{2.18}$$

and finally yields

$$U(\phi) = \frac{\Phi_0 I_\mathrm{c}}{2\pi}(1 - \cos\phi) = E_\mathrm{J}(1 - \cos\phi) \tag{2.19}$$

with the Josephson coupling energy E_J. Its name stresses the analogy to the coupling of two atoms to a molecule as, in both cases, this is based on the overlap of the corresponding wavefunctions.

Besides, a JJ also possesses an energy linked with the charge carriers on the JJ capacitor. The total field energy is given by

$$E_\mathrm{field} = \frac{Q^2}{2C} = \frac{(2Ne)^2}{2C} = 4E_\mathrm{c}N^2, \tag{2.20}$$

where C is the capacitance of the JJ, $Q = 2Ne$ is the total charge of N Cooper pairs and

$$E_\mathrm{c} \equiv \frac{e^2}{2C} \tag{2.21}$$

is the characteristic charging energy corresponding to a single electron charge located on

one of the capacitor plates.

2.3.4 RCSJ model and mechanical analog

The resistively and capacitively shunted junction (RCSJ) model [53, 54] constitutes a very convenient approximation of an actual JJ in order to easily understand its dynamic properties. Essentially, the JJ is represented by an ideal JJ with its nonlinear inductance L_J [cf. Eq. (2.17)] shunted with a voltage-independent normal tunnelling resistance R and the capacitance C between the electrodes. Applying Kirchhoff's law, this parallel resonant circuit can then be described by the differential equation

$$\underbrace{\left(\frac{\Phi_0}{2\pi}\right)^2 C}_{M}\frac{\mathrm{d}^2\phi}{\mathrm{d}t^2}+\underbrace{\left(\frac{\Phi_0}{2\pi}\right)\frac{1}{R}}_{\eta}\frac{\mathrm{d}\phi}{\mathrm{d}t}+\underbrace{I_\mathrm{c}\left[\sin\phi-\frac{I}{I_\mathrm{c}}\right]}_{\frac{\mathrm{d}}{\mathrm{d}\phi}U}=0, \tag{2.22}$$

which is equivalent to the dynamics of a particle with mass M and damping η in a potential

$$U(\phi,I)=E_\mathrm{J}\left(1-\cos\phi-\frac{I}{I_\mathrm{c}}\phi\right). \tag{2.23}$$

This so-called tilted washboard potential extends the Josephson potential energy from Eq. (2.19) by the bias current I as external driving force causing the tilt (cf. Fig. 2.3**a**). For $I<I_\mathrm{c}$ the phase particle is trapped in a local potential minimum where it oscillates with its plasma frequency $\omega_\mathrm{p}=\,=\sqrt{8E_\mathrm{J}E_\mathrm{c}}/\hbar$. Since, in this case, the time average of ϕ is constant, this situation represents the zero-voltage state. Only by quantum tunneling or by thermal activation ("shaking of the washboard potential") the particle can escape a local minimum unless the bias current reaches I_c. Then, potential barriers can be overcome and the phase particle moves down the potential, thereby generating a voltage drop. When the bias current is again reduced below I_c the phase particle only gets immediately trapped in a minimum if its kinetic energy is decreased by strong damping. Otherwise, a voltage drop still persists below I_c, leading to a hysteretic current-voltage characteristic. In order to distinguish these cases, one uses the Stewart-McCumber parameter [53]:

$$\beta_C=\frac{2\pi}{\Phi_0}I_\mathrm{c}R^2C\begin{cases}\ll 1 & \text{strongly overdamped}\\ \gg 1 & \text{strongly underdamped.}\end{cases} \tag{2.24}$$

With this understanding of the underlying physics we now discuss a typical current-voltage (IV) characteristic of a JJ.

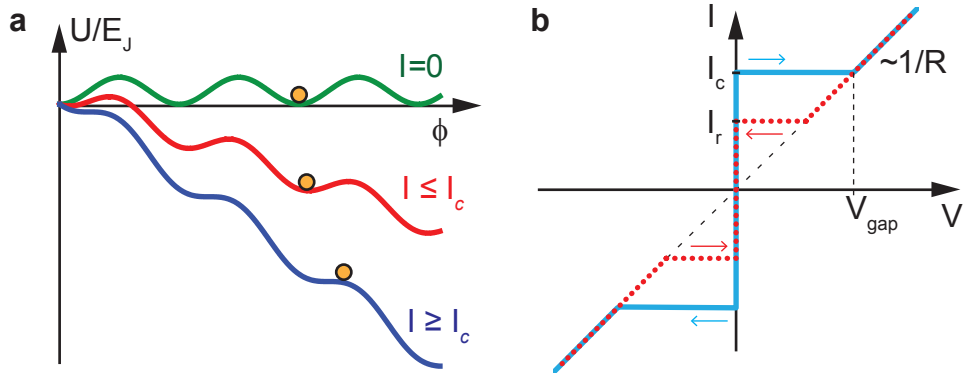

Figure 2.3: **a** Tilted washboard potential of a JJ according to Eq. (2.23) for three values of bias current I. When $I \geq I_\mathrm{c}$ the phase particle (yellow dot) starts moving down the potential. **b** Current-voltage characteristic of an underdamped JJ with hysteretic switching behavior.

2.3.5 Current-voltage characteristic of a JJ

The IV characteristic of a JJ, schematically shown in Fig. 2.3**b**, enables valuable insight into the physical parameters determining the JJ properties. When the current I through the JJ provided by an external constant-current-source is increased from zero, this current is carried by tunnelling of Cooper pairs [cf. Eq. (2.13)] without a voltage drop up to I_c. Above this maximum supercurrent value, quasiparticles tunnel through the JJ and a finite voltage drop develops. Considering the gap in the energy density of states of quasiparticles in a superconductor, it is clear that this voltage is approximately given by the so-called gap voltage

$$V_\mathrm{gap} = \frac{2\Delta_0}{e}, \tag{2.25}$$

where $\Delta_0 = 1.764\, k_\mathrm{B} T_\mathrm{c}$ denotes the superconducting energy gap within the BCS theory with the Boltzmann constant k_B and the critical temperature T_c of the superconductor. The theory of Ambegaokar and Baratoff [55] gives an upper limit for I_c with the value

$$I_\mathrm{c}^\mathrm{AB} = \frac{\pi}{4}\frac{V_\mathrm{gap}}{R}. \tag{2.26}$$

Moreover, the IV curve approaches the linear slope corresponding to the normal resistance R for currents $I \gg I_\mathrm{c}$. When decreasing the current bias again, a hysteretic behavior is possible for the case of low damping ($\beta_C \gg 1$). Even below I_c the phase particle possesses enough kinetic energy to overcome the now existing potential barrier (cf. Fig. 2.3**a**) and there is still a voltage drop at the JJ. In the case of strong damping ($\beta_C \ll 1$), however, already at I_c the kinetic energy is dissipated and the phase particle gets re-trapped, yielding the zero-voltage state and the same curve as for increasing current.

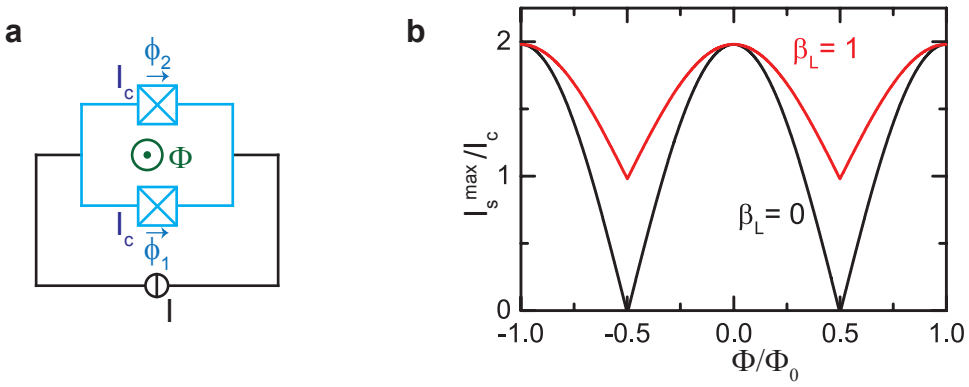

Figure 2.4: **a** Schematic of a current biased dc-SQUID consisting of two JJ in parallel. **b** Flux dependence of the maximum supercurrent of a dc-SQUID. Modulation is maximal for negligible loop inductances (black curve).

2.4 The dc-SQUID

The first JJ-based circuit that is described here is the direct current superconducting quantum interference device (dc-SQUID). It is widely used as a highly sensitive magnetometer [56, 57]. In this work, we use it to read out the state of a persistent-current flux qubit (see Sec. 4.3) and as an effective JJ with a tunable I_c.

The dc-SQUID consists of a parallel circuit of two (identical) JJs as depicted in Fig. 2.4**a**. In the absence of a magnetic field, the dc-SQUID can then simply be understood as one JJ with effective parameters[2] $R' = R/2$, $C' = 2C$ and $I_c' = 2I_c$ and the IV characteristic looks like in Fig. 2.3**b**.

However, the unique physical properties of this device are not only based on the Josephson equations but also on fluxoid quantization, which comes into play when a magnetic flux is applied to the area of the SQUID loop. Assuming that the two JJ are identical they have in particular the same I_c. Yet, the gauge invariant phase differences of the two JJ are not independent. They are connected via the fluxoid quantization condition given in Eq. (2.5), which finally yields the relation

$$\phi_2 - \phi_1 = \frac{2\pi}{\Phi_0}\Phi\,. \tag{2.27}$$

Note that, here, Φ is again the total flux $\Phi = \Phi_{ex} + (L_g + L_k)I_{circ}$ with the current I_{circ} circulating in the SQUID loop. The contributions of geometric and kinetic inductance depend on the wire geometry. For the case of negligible flux contribution due to I_{circ}, i.e., $\Phi = \Phi_{ex}$, the SQUID exhibits a maximum supercurrent

$$I_s^{max} = 2I_c \left|\cos\left(\pi\frac{\Phi_{ex}}{\Phi_0}\right)\right| \tag{2.28}$$

[2]This assumption holds for negligible screening, $\beta_L \ll 1$, see below.

before switching to the voltage state. Since the periodicity of this flux dependence, shown in Fig. 2.4**b**, is given by the elementary flux quantum, an adequate technical implementation enables the measurement of very small magnetic fields. The more general case of non-negligible inductance can no longer be calculated analytically but numerically [58] and yields the same flux dependence. Only the modulation of the maximum supercurrent is reduced depending on the so-called screening parameter

$$\beta_L = \frac{2LI_\mathrm{c}}{\Phi_0} \tag{2.29}$$

with the total loop inductance $L = L_\mathrm{g} + L_\mathrm{k}$. This screening parameter quantifies the flux induced by a circulating current $I_\mathrm{circ} = I_\mathrm{c}$ in units of $\Phi_0/2$. In Fig. 2.4**b**, the red curve represents the case of $\beta_L = 1$, where the modulation depth is reduced to 50 percent. For $\beta_L \gg 1$, the modulation depth further decreases linearly with $1/\beta_L$ [58]. For the application of a SQUID as a magnetometer a maximum modulation, i.e., $\beta_L = 0$, is desirable for best flux sensitivity. Moreover, we need to fulfill $\beta_L \lesssim 2/\pi$ in order to avoid a hysteretic flux dependence of the maximum supercurrent of the SQUID [59]. However, for the practical SQUIDs used in this work, especially for the SQUIDs as tunable α-JJ of the qubit, the screening may become relevant in a quantitative analysis as discussed in Sec. 6.4.

Finally, it must be emphasized that the switching of both a single JJ as well as a dc-SQUID into the voltage state is a statistical process. It occurs when the phase particle escapes the local potential minimum or metastable state by thermal activation or quantum tunneling. Hence, for a large number of repeated measurements the switching current underlies a distribution around a mean value $\overline{I}_\mathrm{sw}$ with a standard deviation σ. If the switching is dominated by thermal activation, the distribution broadens and its mean value is slightly lowered. If the escape is dominated by quantum tunnelling, the standard deviation σ depends on the plasma frequency ω_p and, hence, on the mass M of the phase particle. For higher mass, the plasma frequency, which corresponds to the attempt frequency for the escape, and thus the escape rate of the phase particle decrease. As a result, the switching current distribution gets narrower and the sensitivity of the magnetometer improves. In practice, the mass of the phase particle is often increased by enlarging the capacitance $C \propto M$ by additional shunting capacitors (cf. Sec. 4.3).

2.5 Superconducting quantum circuits

The above discussion on JJs and SQUIDs is based on the macroscopic quantum model of superconductivity. However, apart from the assumption of a macroscopic wave function, the description of these elements is classical in the sense that the relevant variables

such as the phase difference are described by classical equations of motion. But for the investigation of qubits and resonators in the following a quantum mechanical treatment needs to account for quantized energy levels and the exchange of single excitations. To follow the usual path of quantum mechanics, first, the Hamiltonian of the system is derived from classical energies and then, classical variables are replaced by their quantum operator equivalents. As it turns out [60, 61], the operators $\hat{\Phi}$ and $\hat{Q}$ for flux and charge, respectively, are canonically conjugate variables and obey the commutation relation

$$\left[\hat{\Phi}, \hat{Q}\right] = i\hbar \tag{2.30}$$

just as position and momentum operators in mechanics. Consequently, the standard deviations of flux and charge operators $\Delta\Phi$ and ΔQ, respectively, also need to fulfill the Heisenberg uncertainty relation

$$\Delta\Phi\Delta Q \geq \frac{\hbar}{2}. \tag{2.31}$$

The equations of motion are now found via the Schödinger or von Neumann equation. It is easy to see how to bring simple superconducting circuits into the quantum regime. Certainly, one needs to suppress thermal fluctuations below the energy level spacing by cooling. For a Josephson junction, we additionally need to determine whether the energy

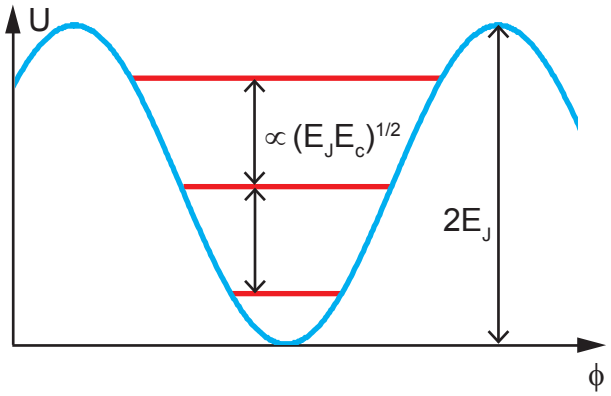

Figure 2.5: Discrete energy levels within the Josephson potential. For small junction size, the quantum regime with well separated levels is reached.

levels inside one well of the Josephson potential are densely spaced (classical) ore well-separated (quantum), as depicted in Fig. 2.5. To this end, we form the ratio between the height of the Josephson potential and the level spacing, $E_\mathrm{J}/\hbar\omega_\mathrm{p} \approx \sqrt{E_\mathrm{J}/E_\mathrm{c}}$. Since this ratio is proportional to the junction area, we conclude that small junctions are more "quantum" than large junctions. In practice, JJ with submicron dimensions are required for the construction of superconducting quantum circuits. However, before discussing quantum bit circuits including JJ, the simplest quantum integrated circuit is introduced: the quantum harmonic LC oscillator.

2.6 Superconducting resonators

In this section, superconducting resonators are introduced as an import building block for superconducting circuits. They feature, on the one hand, the capability to store microwave quantum states due to their better coherence properties as compared to superconducting qubits. On the other hand, the ability to couple superconducting resonators and qubits strongly, promises to use them for qubit readout or as a quantum bus. Specifically, a superconducting resonator is an alternative readout device for a flux qubit in the experiments of Chapter 6 as compared to the SQUID readout used in Chapter 5. Although this is important from an experimental point of view, this wording would, however, ignore the great importance of both, qubits and resonators in the fascinating field of circuit QED (cf. Sec. 3.4). In the following, we first introduce the specific realization of our superconducting resonator, followed by a description of it in terms of a quantum harmonic oscillator.

2.6.1 Coplanar waveguide resonators

A coplanar waveguide resonator is the solid-state analog to an optical cavity in the field of quantum optics, where laser light is reflected between to highly reflective mirrors and thus forms a standing electromagnetic wave inside this resonator. Analogously, a superconducting resonator is built from a transmission line interrupted by two capacitors (cf. Fig. 2.6**a**). While the line is matched to $50\,\Omega$, the capacitors cause a high impedance mismatch and therefore behave as semitransparent mirrors for a signal propagating along the transmission line. Among different geometric realizations of superconducting transmission lines, we focus on the coplanar waveguide (CPW) layout, which can be considered as a 2D-version of a coaxial cable (cf. Fig. 2.6**a**). It consists of an inner conductor of width w separated on both sides by a distance s from large ground planes. A CPW is very well-suited for our purposes due to several reasons. CPW transmission lines can be reliably matched to a characteristic impedance $Z_0 = 50\,\Omega$ by adjusting the size of w and s. The resonant frequency of a CPW resonator depends on the length of the resonator, i.e., the distance between the two capacitors, and can be designed to match typical transition frequencies of the flux qubit, which range from $1-10\,\mathrm{GHz}$. With a superconducting resonator material such as niobium, relatively high resonator qualities can be reached. Most importantly, only the length scale along the CPW is on the order of the wavelength, whereas the dimensions in transverse directions are much smaller than the wavelength. For this quasi-1D element the mode volume V_{mod} of the standing electromagnetic field is very small. As a consequence, much higher vacuum magnetic field strengths $B_{\mathrm{vac}} \propto 1/\sqrt{V_{\mathrm{mod}}}$ as compared to optical cavities allow for stronger coupling to the magnetic dipole moment of flux qubits in circuit QED (cf. Sec. 3.4).

The capacitors implicate the boundary condition of nodes of the supercurrent at the resonator ends. Consequently, the ground mode of the resonator with length l is a $\lambda/2$-mode as visualized in Fig. 2.6**a**. The wavelength λ of the fundamental mode of the standing wave obeys the relation $l = \lambda/2$. The different resonant modes come with resonant frequencies

$$\omega_n = n\frac{c}{2l\sqrt{\epsilon_{\text{eff}}}} = n\frac{\pi}{l\sqrt{\ell\tilde{c}}} \tag{2.32}$$

where ϵ_{eff} is the effective dielectric constant of the CPW, ℓ is the inductance per unit length, $\tilde{c}$ the capacitance per unit length, and $n = 1,2,...$ is the mode number starting with the fundamental mode $n = 1$. Via its capacitors, the CPW resonator is coupled to an input and an output transmission line, which are also $50\,\Omega$ matched CPWs. With these, the frequency dependence of the power transmitted through the resonator can be measured. The resonator manifests itself in transmission maxima at its resonance frequencies. The Lorentzian shape of such a resonance is shown in Fig. 2.6**b**. The FWHM (full width at half maximum) linewidth of the resonance equals the decay rate κ_n of the photons in mode n, which determines the quality factor

$$Q_n = \frac{\omega_n}{\kappa_n} \tag{2.33}$$

of the nth mode. The quality factor determined in this way from a measured spectrum is, to be more precise, the loaded quality factor Q_{L} given by

$$\frac{1}{Q_{\text{L}}} = \frac{1}{Q_{\text{int}}} + \frac{1}{Q_{\text{ext}}} \tag{2.34}$$

where Q_{int} and Q_{ext} are the internal and external quality factors, respectively. The internal quality is limited by resistive, radiative and, predominantly, dielectric losses. The latter are believed to be caused at millikelvin temperatures and small photon numbers in the resonator by two-level systems (TLS) in the substrate absorbing energy from the resonator's electromagnetic field. The external quality is mainly determined by the coupling capacitors and can thus be adjusted. Typically, internal losses are dominant for our resonators so that $Q_{\text{L}} \approx Q_{\text{int}}$ (cf. Sec. 6.2.1).

From an electrotechnical point of view such a distributed resonator can also be modeled as a lumped-element resonator, which is depicted in Fig. 2.6**c**. Near resonance, a CPW resonator behaves as a parallel LCR circuit [62], that is on both sides connected via a coupling capacitor C_κ to an external load R_{L}. This representation is the basis for the quantum mechanical treatment of a superconducting resonator in the following subsection.

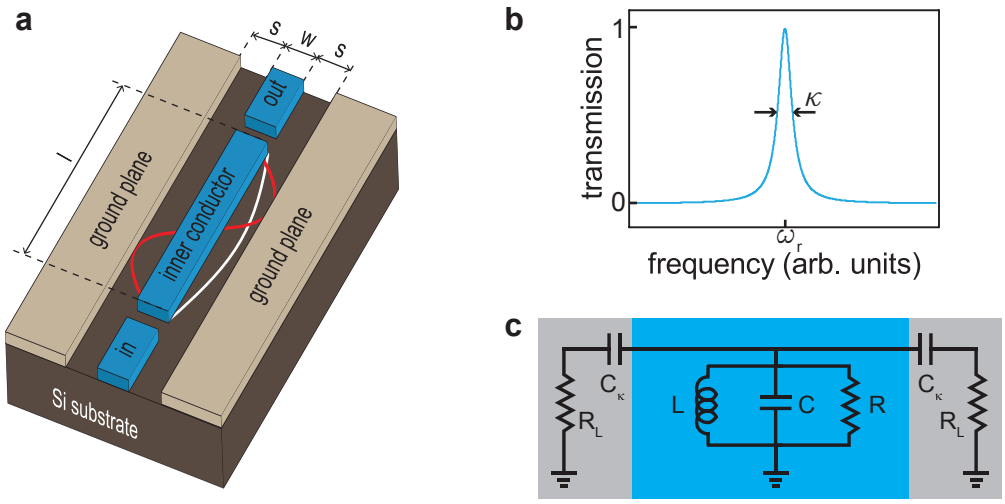

Figure 2.6: **a** Schematic layout of a $\lambda/2$ coplanar waveguide (CPW) resonator. Fundamental $\lambda/2$-mode (white) and λ-mode (red) of the standing wave resonator current are illustrated. **b** Theoretical power transmission spectrum of a CPW transmission line resonator. Near a resonant frequency $\omega_n/2\pi$, transmission exhibits a peak of Lorentzian shape with full width at half maximum $\kappa_n/2\pi$. Away from resonance, the CPW resonator is a strong transmission filter. **c** Equivalent circuit diagram of a CPW resonator: Near resonance it can be modeled as a parallel LCR circuit that is capacitively coupled (via C_κ) to an external load R_L of input and output line.

2.6.2 The quantum harmonic oscillator

Following the recipe given in Sec. 2.5, a superconducting transmission line resonator can be described as a quantum harmonic oscillator. In the lumped-element representation of Fig. 2.6**c** we neglect the normal resistance R and end up with a parallel LC circuit with a classical Hamiltonian

$$H = \frac{1}{2}LI^2 + \frac{1}{2}CV^2 = \frac{\Phi^2}{2L} + \frac{Q^2}{2C} = \frac{\Phi^2}{2L} + \frac{1}{2}L\omega_\mathrm{r}^2 Q^2 \tag{2.35}$$

where $\Phi = LI$ is the magnetic flux in the inductor, $Q = CV$ is the charge on the capacitor, and $\omega_\mathrm{r} = 1/\sqrt{LC}$ is the resonant frequency of an LC circuit. It can easily be seen that $\partial H/\partial Q = -\dot{\Phi}$ and $\partial H/\partial \Phi = \dot{Q}$, meaning that Q and Φ correspond to the generalized canonical position and momentum variables. Furthermore, Eq. (2.35) can be considered an analog to the standard quantum harmonic oscillator with the substitutions $x \to Q$, $p \to \Phi$ and $m \to L$. Consequently, these variables Q and Φ are replaced by quantum mechanical operators $\hat{Q}$ and $\hat{\Phi}$ that can be expressed by

$$\hat{Q} = \sqrt{\frac{\hbar}{2\omega_\mathrm{r}L}}(\hat{a}^\dagger + \hat{a}) \quad \text{and} \quad \hat{\Phi} = i\sqrt{\frac{\hbar\omega_\mathrm{r}L}{2}}(\hat{a}^\dagger - \hat{a}) \tag{2.36}$$

with the bosonic creation and annihilation operators $\hat{a}^\dagger$ and $\hat{a}$, that fulfill the commutation relation $\left[\hat{a}^\dagger, \hat{a}\right] = 1$. Substituting Eq. (2.36) in Eq. (2.35) finally yields the Hamiltonian of a quantum harmonic oscillator

$$\hat{H}_\mathrm{r} = \hbar\omega_\mathrm{r}\left(\hat{a}^\dagger\hat{a} + \frac{1}{2}\right) \tag{2.37}$$

with the photon number operator $\hat{N} \equiv \hat{a}^\dagger\hat{a}$. Finally it must be noted that the quantum mechanical behavior described here can only be observed in an experimental regime of negligible thermal excitations, i.e., $k_\mathrm{B}T \ll \hbar\omega_\mathrm{r}$. For the resonator we use in Chapter 6 with $\omega_\mathrm{r}/2\pi \simeq 5\,\mathrm{GHz}$, this scenario is achieved by cooling to temperatures of only $T \simeq 20\,\mathrm{mK}$. Furthermore, a resonator occupation on the order of only one photon is desirable for circuit QED experiments (cf. Sec. 6.2.3).

Chapter 3

The gradiometric and tunable-gap flux qubit

This chapter concentrates on the theoretical description of the different types of persistent current flux qubits that are investigated in this work. First, the standard 3-JJ flux qubit is described with its potential energy and quantum mechanical behavior in Sec. 3.1. The tunability of the qubit gap is explained and thus, the tunable-gap flux qubit is introduced in Sec. 3.2. Then, we focus in Sec. 3.3 on the specific features that come along with a gradiometric layout of a flux qubit. Finally, we bring together the flux qubit with superconducting resonators as discussed in Sec. 2.6 to the field of circuit quantum electrodynamics in Sec. 3.4. [1]

3.1 The flux qubit

The simplest version of the flux qubit (cf. Fig. 3.1) consists of a small superconducting loop with a diameter on the order of 10 µm intersected by three JJs with lateral dimensions on the order of 100 nm [20]. While two of these JJs have the same area A_J and, hence, the same critical current (typically, $A_\mathrm{J} \simeq 0.03\,\mu\mathrm{m}^2$ and $I_\mathrm{c} \simeq 600\,\mathrm{nA}$), the third JJ, the so-called α-junction, has a reduced area $A_\alpha = \alpha A_\mathrm{J}$ with $\alpha \simeq 0.6{-}0.8$, resulting in a reduced critical current $I_{\mathrm{c},\alpha} = \alpha I_\mathrm{c}$ and a reduced junction capacitance $C_\alpha = \alpha C_\mathrm{J}$. As discussed in more detail in the following subsections, for $\alpha \simeq 0.6{-}0.8$, the two-dimensional potential energy landscape of the flux qubit can be simplified. At the symmetry point, where the magnetic flux through the loop is equal to $(n+\frac{1}{2})\Phi_0$, with n being an integer, the potential can be reduced to a one-dimensional double well [22]. The two minima of this potential are associated with two degenerate persistent current states, corresponding to clockwise and counter-clockwise circulating persistent currents $\pm I_\mathrm{p}$. Due to the finite tunnel coupling of these states, their degeneracy is lifted. The resulting symmetric and

[1] Some parts of this chapter follow the author's work in Ref. [63]

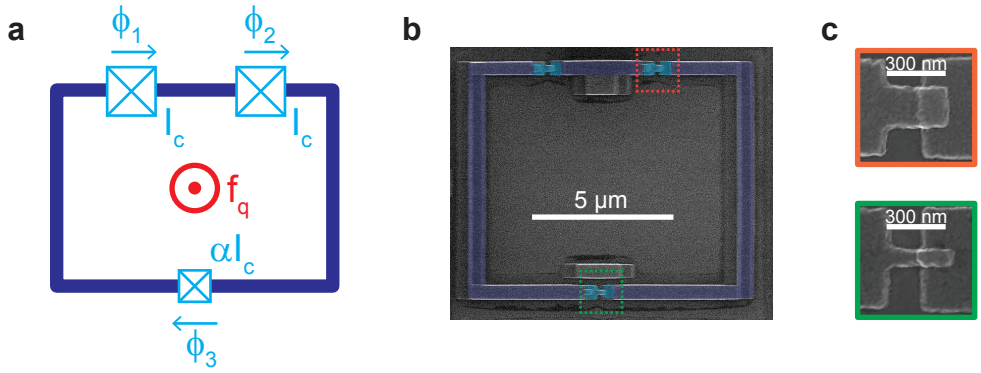

Figure 3.1: Fixed-gap non-gradiometric 3-JJ flux qubit. **a** Circuit schematic: a superconducting loop (dark blue) with two JJs (light blue boxes) of area A_J and a third one with reduced area αA_J. For an applied magnetic frustration $f_q \neq 0$, dc screening currents are induced. **b** Scanning electron microscope (SEM) image. The color code corresponds to **a**. The dashed rectangles mark closeup regions. **c** Closeups on one regular JJ (orange) and the α-junction.

anti-symmetric superposition states form the ground and excited state of the flux qubit separated by the minimal energy splitting $\hbar\Delta$.

3.1.1 Potential energy of the flux qubit

Because of the negligible loop inductance [2], the potential energy of the 3-JJ flux qubit is given by the sum over the Josephson energies [cf. Eq. (2.19)] of its 3 junctions,

$$U_q(\phi_1,\phi_2,\phi_3) = E_J[(1-\cos\phi_1)+(1-\cos\phi_2)+\alpha(1-\cos\phi_3)]. \tag{3.1}$$

Similar to the situation for a dc-SQUID (cf. Sec. 2.4) the flux qubit as a superconducting ring only intersected by JJs needs to obey fluxoid quantization and Eq. (2.11) is extended with the phase differences across the JJs to yield [3]

$$\phi_1+\phi_2+\phi_3+\phi_g+\phi_k+2\pi f_q = 2\pi n. \tag{3.2}$$

Since the loop is small, the phase differences linked to geometric and kinetic inductance, ϕ_g and ϕ_k, can be neglected again. Due to the 2π-periodicity of the Josephson potential, we only consider the case $n=0$ without loss of generality. Inserting Eq. (3.2) into Eq. (3.1), we obtain [22]

$$U_q(\phi_1,\phi_2,f) = E_J[2+\alpha-\cos\phi_1-\cos\phi_2-\alpha\cos(2\pi f_q+\phi_1+\phi_2)]. \tag{3.3}$$

[2] Note that the assumption, that inductive energies of the loop are negligible in comparison with the JJ energies is valid, regardless of the fact that the contributions of geometric and kinetic inductances need to be considered for loops not directly containing JJs (cf. Sec. 2.2).

[3] Note that, in the literature, the phase difference ϕ_2 is often defined with opposite sign.

This 2π-periodic qubit potential energy has the shape of an egg carton where each cell has some substructure. In particular, near $f_\mathrm{q} \simeq n + 0.5\,(n \in \mathbb{Z})$ and for $0.5 < \alpha < 1$, two stable minima are only separated by a small potential barrier and thus form a double-well potential (cf. Fig. 3.2). The two minima are located at $(\phi_1,\phi_2) = (-\phi^*,-\phi^*)$ and $(\phi_1,\phi_2) = (+\phi^*,+\phi^*)$, respectively, where $\cos\phi^* = 1/(2\alpha)$. Considering the first Josephson equation, Eq. (2.13), shows that the minima are associated with circulating persistent currents of opposite direction. There also exists a double-well potential containing two minima of neighboring unit cells, illustrated as well in Fig. 3.2. However, for $\alpha < 1$ the potential barrier for the intracell tunnelling is lower and, thus, the tunnelling rate is higher than for the case of tunnelling between neighboring cells. The circulating current at the respective minimum can be calculated from Eq. (3.3). For $f_\mathrm{q} = 0.5$, one finds [4]

$$\pm\, I_\mathrm{p} = \left.\frac{\partial U_\mathrm{q}}{\partial \Phi_\mathrm{q}}\right|_{\phi_1=\phi_2=\pm\phi^*} = \pm I_\mathrm{c}\sqrt{1-1/(2\alpha)^2}. \tag{3.4}$$

This symmetric constellation where the two minima are degenerate in energy and correspond to persistent currents of opposite sign but with the same absolute value is only given for $f_\mathrm{q} = n + 0.5$, which is referred to as the degeneracy point. Going slightly away from this point lifts the degeneracy and makes the one or the other local minimum energetically favorable (cf. Fig. 3.3**a**) and the total current circulating in the loop becomes finite (cf. Fig. 3.3**b**). Far away from the degeneracy point, only one stable minimum (with a current $+I_\mathrm{p}$ or $-I_\mathrm{p}$, respectively) exists.

So far, our analysis was completely classical. In the next section, we proceed with a quantum description of the flux qubit.

3.1.2 Quantum two-level system

Near the degeneracy point of the flux qubit, $f_\mathrm{q} \approx n + 0.5$, the two (almost) degenerate discrete energy levels of the double-well potential couple via a quantum tunnelling process. This leads to the formation of new, non-degenerate superposition states. Formally, the two-level system near the degeneracy point is described by a Hamiltonian

$$\hat{\mathcal{H}} = \frac{1}{2}\hbar\varepsilon\hat{\sigma}_z - \frac{1}{2}\hbar\Delta\hat{\sigma}_x = \frac{\hbar}{2}\begin{pmatrix}\varepsilon & \Delta\\ \Delta & -\varepsilon\end{pmatrix}. \tag{3.5}$$

Here, $\hat{\sigma}_z$ and $\hat{\sigma}_x$ are the Pauli spin operators. The flux-dependent magnetic energy bias

$$\hbar\varepsilon = 2\frac{\partial U_\mathrm{q}}{\partial \Phi_\mathrm{q}}\delta\Phi_\mathrm{q} = 2I_\mathrm{p}\delta\Phi_\mathrm{q} \tag{3.6}$$

[4] Remember that, in general, $\frac{\partial U}{\partial \Phi} = \frac{\partial U}{\partial I}\frac{\partial I}{\partial \Phi} = \frac{\partial(0.5LI^2)}{\partial I}\frac{\partial(\Phi/L)}{\partial \Phi} = I$.

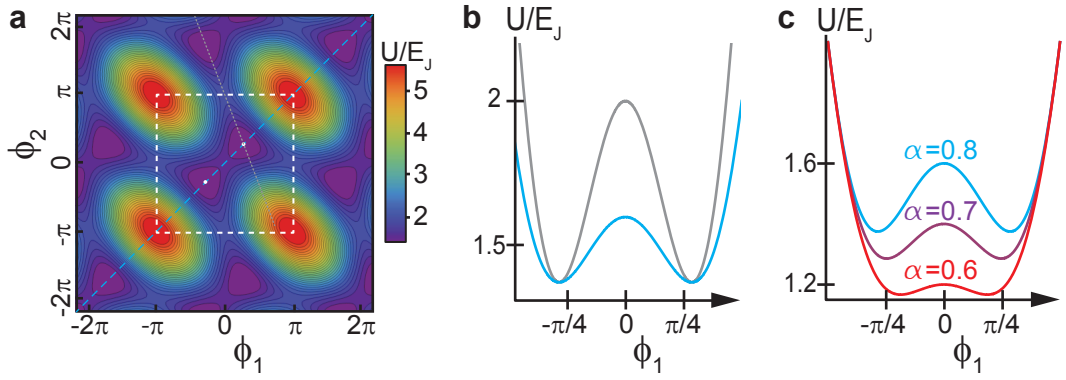

Figure 3.2: Qubit potential energy. **a** 2D plot of the potential energy for $f_q = 0.5$ and $\alpha = 0.8$. The white dashed rectangle marks the unit cell of the periodic potential. The blue line ($\phi_2 = \phi_1$) marks the scenario of intracell tunnelling. The gray line [$\phi_2 = \phi_1(\phi^* - \pi)/\phi^* + \pi$] corresponds to intercell tunnelling. **b** 1D potential energy for intercell (gray line) and intracell (blue line) tunneling corresponding to the cuts in **a**. **c** Double-well potential for $f_q = 0.5$ and different values of α.

with $\delta\Phi_q = \Phi_0[f_q - (n + \frac{1}{2})]$ is linked with the potential energy of Eq. (3.3) and the classical persistent current states $|+I_p\rangle$ and $|-I_p\rangle$. The off-diagonal (tunneling) matrix element Δ causes the coupling of these classical persistent current states. As a consequence, the energy eigenstates of Eq. (3.5) are separated by $\hbar\Delta$ at the degeneracy point. That is why we also refer to $\hbar\Delta$ as the *qubit gap*. The energy levels are shown in Fig. 3.3**c**. Near the degeneracy point, the two lowest energy levels are well-separated from the higher ones. Right at $\delta\Phi_q = 0$, we can write ground state $|g\rangle$ and first excited state $|e\rangle$ as

$$|g\rangle = \frac{1}{\sqrt{2}}\left(|-I_p\rangle + |+I_p\rangle\right) \text{ and}$$
$$|e\rangle = \frac{1}{\sqrt{2}}\left(|-I_p\rangle - |+I_p\rangle\right) . \tag{3.7}$$

In this situation, there is no net circulating current and, hence, no net magnetic moment. Away from the degeneracy point, where $\varepsilon \gg \Delta$, the ground and excited states correspond in good approximation to the current states $|\pm I_p\rangle$. As long as we are not too far away from the degeneracy point, the energy difference between ground and excited state can be approximated by

$$E_{eg} = \hbar\omega_q = \hbar\sqrt{\Delta^2 + \varepsilon^2} \tag{3.8}$$

with the qubit transition frequency ω_q as depicted in Fig. 3.3**d**. This relation implies that the qubit transition frequency is minimal at the degeneracy point and increases when going away from it. Furthermore, at the degeneracy point, the qubit transition energy does not depend on the magnetic flux to first order, $\partial E_{eg}/\partial\Phi_q = 0$. Consequently, the qubit is much less sensitive to low-frequency external flux noise at this so-called sweet spot. For this reason, the qubit should be operated at a fixed degeneracy point for

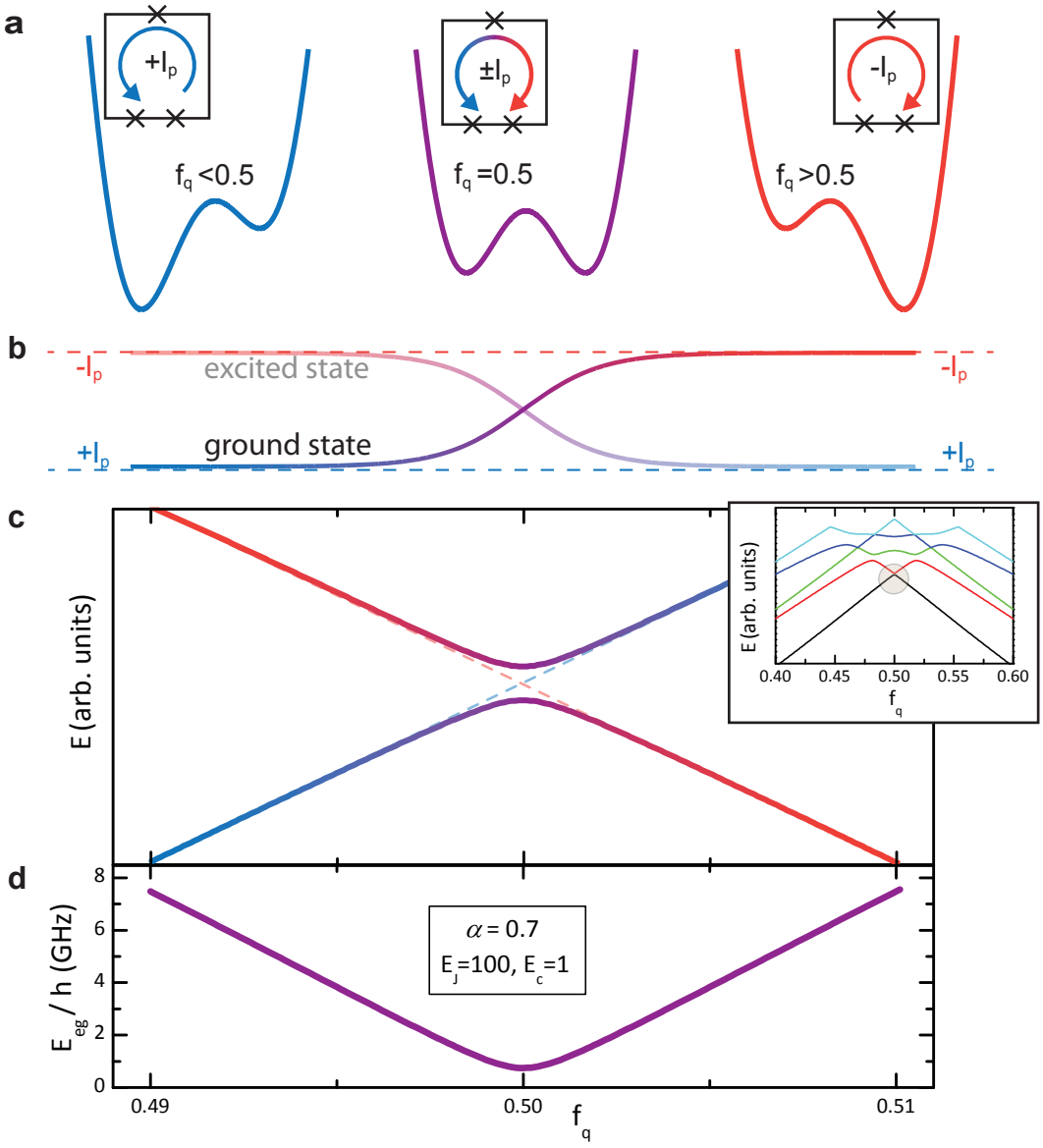

Figure 3.3: Flux dependence of **a** the flux qubit double-well potential, **b** its net circulating current, **c** its two lowest eigenenergies with avoided crossing (inset showing more energies) and **d** the qubit transition frequency E_{eg}/h between ground and excited state.

optimal phase coherence.

3.1.3 Tunability of the qubit gap

For a standard 3-JJ flux qubit, the frequency is tuned by changing the magnetic energy bias ε. Since this can be done by adjusting the frustration of the qubit loop with an external magnetic field, it is very easy to realize. Such frequency tunability is, for example, highly desirable for coupling the qubit to or decoupling it from a microwave resonator. However, tuning the qubit frequency via the magnetic energy bias ε has the drawback of leaving the point of optimal phase coherence. The more promising approach is to tune the qubit frequency while staying at the degeneracy point. In order to do so, one must change the qubit gap Δ via the barrier height of the double well potential.
From a tight-binding calculation of the qubit eigenstates [22], the gap Δ can be approximated to

$$\Delta = \sqrt{\frac{4E_\mathrm{J}E_\mathrm{c}(4\alpha^2-1)}{\hbar^2\alpha(1+2\alpha)}}\ \exp\left(-a(\alpha)\sqrt{4\alpha(1+2\alpha)\frac{E_\mathrm{J}}{E_\mathrm{c}}}\right)\ , \tag{3.9}$$

where $a(\alpha)=\sqrt{1-(1/4\alpha^2)}-[\arccos(1/2\alpha)/2\alpha]$ with $a(\alpha)\simeq 0.15$ for $\alpha=0.7$. We see that the qubit gap Δ is exponentially dependent on the three parameters critical current I_c (via E_J), junction capacitance C (via E_c) and the factor α. The parameters E_J and E_c certainly have to lie within proper margins for a working qubit, but the value of α is the most dominant for the qubit gap Δ. Apart from this, only α is accessible for an in-situ variation (see following section). Typically, the qubit gap Δ should be on the order of a few gigahertz to match the resonance frequency of a microwave resonator. As it is shown in Fig. 3.4, for typical values of charging energy $E_\mathrm{c}/h=1\,\mathrm{GHz}$ and Josephson energies $E_\mathrm{J}/h=20...500\,\mathrm{GHz}$, the qubit gap is far too low for values of $\alpha\simeq 1$. This corresponds to the fact, that for $\alpha=1$ the barrier of the double-well potential reaches a maximum height (cf. Fig. 3.2**c**) and tunnelling becomes very unlikely. Decreasing α from 1 to 0.5 results in a strong increase of the exponential factor in Eq. (3.9) as the barrier height decreases. At the same time, the prefactor (attempt frequency) decreases from the plasma frequency of the JJ to zero, because the double well potential becomes a single well at $\alpha=0.5$. Since the exponential factor dominates within the major part of the interval $0.5<\alpha<1$, a strong increase of Δ is obtained by reducing α. The higher the ratio $E_\mathrm{J}/E_\mathrm{c}$, the steeper is the increase of $\Delta(\alpha)$.

Although the tight-binding approximation allows for an analytical illustration of the basic $\Delta(\alpha)$ dependence, reliable quantitative results can only be derived numerically from the qubit Hamiltonian [cf. Eq. (3.5)]. To this end, the Hamiltonian is diagonalized and its eigenenergies are calculated. The dependence $\Delta(\alpha)$ determined in this manner is also displayed in Fig. 3.4, revealing the limits of the tight-binding approximation. In

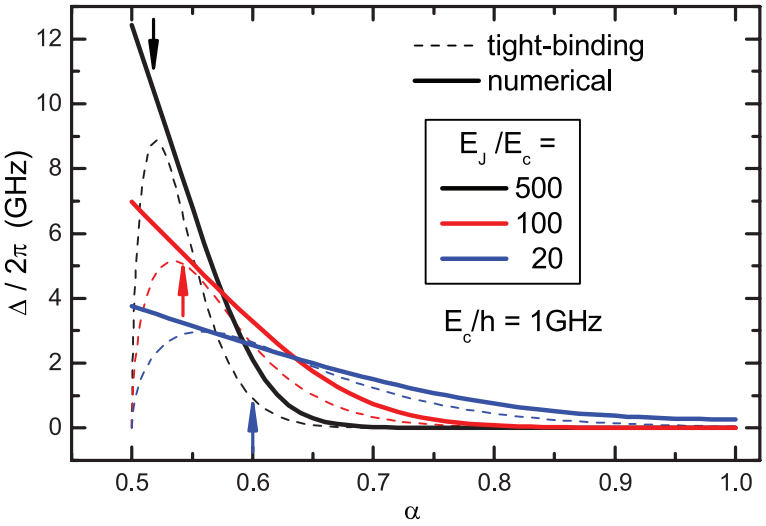

Figure 3.4: **a** Dependence of the qubit gap Δ on the value α. For different values of E_J/E_c, we show the results of, both, the tight-binding approximation of Eq. (3.9) (dashed lines), and the numerical diagonalization of the qubit Hamiltonian (solid lines). The arrows mark the α values, at which the double-well barrier height equals the thermal energy at 30 mK.

contrast to the latter, the numerical solution does not include a decrease of the qubit gap for $\alpha \approx 0.5$. In fact, we also do not observe this behavior in our data (cf. Sec. 5.3). Close to $\alpha = 0.5$, however, the decreasing barrier of the double-well potential lets thermal excitations compete with quantum tunneling. Then, no quantum signature is visible at all. A temperature of 30 mK corresponds to a thermal energy $k_B T/h = 0.63$ GHz. We calculate, at which α values the barrier height of the double-well potential equals this thermal energy. These α values depend, of course, on E_J, which linearly enters the barrier height [cf. Eq. (3.3)]. The calculated values are marked in Fig. 3.4.

In summary, the exponential dependency of the qubit gap on JJ fabrication parameters causes the difficulty to build a fixed-gap flux qubit with a well-defined Δ. The values E_J, E_c and α are determined by the dimensions (some hundreds of nanometers) and by the oxide layer (few nanometer thickness) of the JJs and therefore underlie a large uncertainty. This drawback of the fixed-gap flux qubit can be overcome by a tunable-gap qubit, which is more tolerant to inevitable fabrication variations.

3.2 The tunable-gap flux qubit

According to Eq. (3.8), ω_q cannot only be tuned by varying ε but also by varying Δ. This is advantageous, since the operation point of the qubit stays at the symmetry point, where phase coherence is optimal. Flux qubits with tunable Δ are called *tunable-gap* flux qubits. As pointed out by Mooij *et al.* already in their first proposal of the flux qubit

[20], an *in situ* tunability of Δ is achieved by replacing the α-junction by a small α-loop containing two JJs (cf. Fig. 3.6**b**). In the language of Josephson physics, this means that the α-junction is replaced by a dc-SQUID. Then, the critical current $I_{c,\alpha}$ of the α-loop and, in turn, the qubit gap Δ can be tuned by a control flux $\Phi_\alpha \equiv \Phi_0 f_\alpha$ threading the α-loop [cf. Eq. (2.28)]. If we choose the area of the junctions in the α-loop to $\alpha_0 A_J/2$, we obtain

$$I_{c,\alpha} = \alpha I_c = \alpha_0 I_c |\cos(\pi f_\alpha)| \,. \tag{3.10}$$

In Fig. 3.5, we show the dependence $\alpha(f_\alpha)$ calculated from Eq. (3.10) for $\alpha_0 = 1$ together

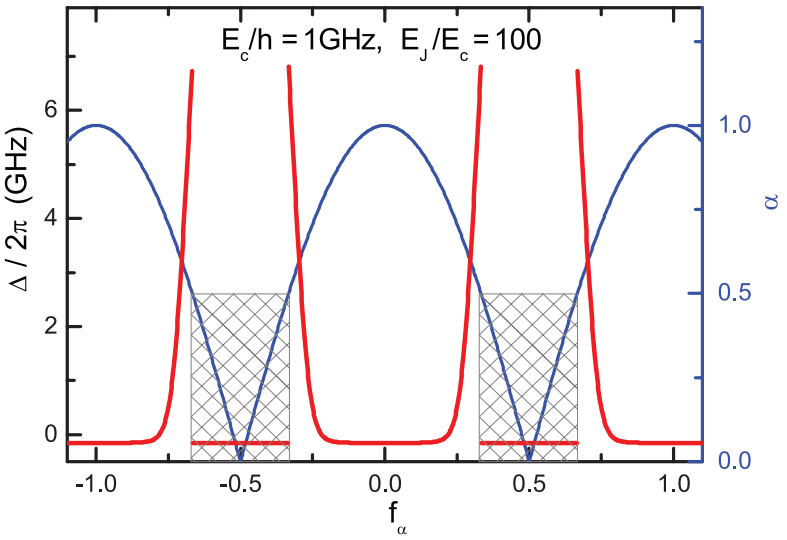

Figure 3.5: Qubit gap Δ (left axis) and value of α (right axis) versus the α-loop frustration f_α. In the shaded regions, $\alpha < 0.5$ and the double-well potential vanishes.

with the dependence $\Delta(f_\alpha)$, which is calculated numerically from the qubit Hamiltonian using the input parameters $E_c/h = 1\,\text{GHz}$ and $E_J/h = 100\,\text{GHz}$. The strong nonlinear dependence $\Delta(f_\alpha)$ allows us to significantly change the gap with only small variations in the flux applied to the α-loop.

Successful implementations of this design have been reported recently [39, 64–66]. While the replacement of the α-junction by an α-loop allows for a tunable qubit gap Δ, applying any flux to the α-loop at the same time changes the flux threading the qubit loop and hence the energy bias ε of the flux qubit. This is unintentional and has to be compensated. To keep the energy bias of the flux qubit constant during variations of Φ_α, a gradiometric design can be used.

3.3 The gradiometric tunable-gap flux qubit

Usually, a gradiometric design is used for magnetometers (also in combination with SQUIDs) in order to increase the sensitivity of the measurement. Gradiometric means that this object is not affected by homogenous magnetic fields, but is only sensitive to gradients of magnetic fields. For a flux qubit, the intention of the gradiometric design is to leave the usually flux-dependent potential energy of the qubit given by Eq. (3.3) unaffected by a homogeneous magnetic field. This is equivalent to a constant net current through the JJs of the flux qubit. The gradiometric versions of a fixed-gap and a tunable-gap flux qubit are shown in Fig. 3.6**c** and Fig. 3.6**d**, respectively. In both cases, the main structure is that of an eight-shaped gradiometric loop, where the screening currents in the two subloops, generated by an applied homogeneous magnetic field, cancel each other on the central line, thus leaving the qubit potential energy unaffected. For the tunable-gap

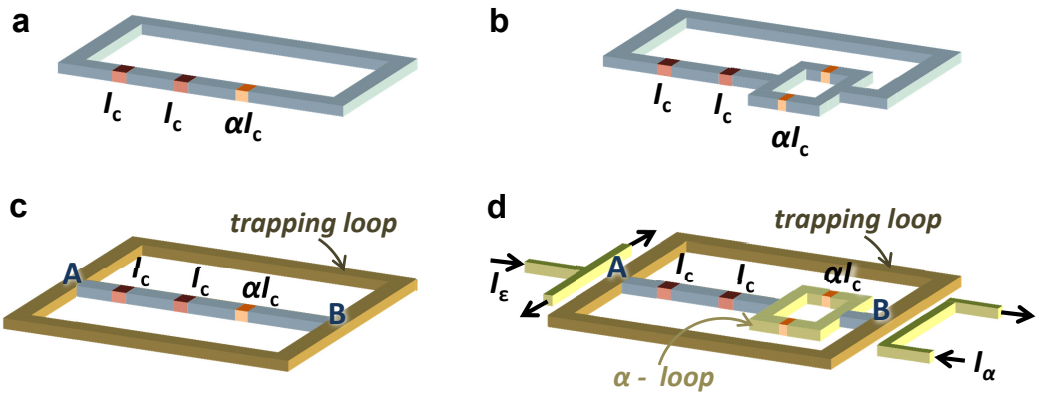

Figure 3.6: Circuit schematics of **a** the three-Josephson-junction (3-JJ) flux qubit with α-junction, **b** the simplest 3-JJ flux qubit with the tunable α-junction realized by a dc-SQUID, **c** the gradiometric 3-JJ flux qubit without tunable α-junction, and **d** the gradiometric 3-JJ flux qubit with tunable α-junction. The α- and ε-lines can be used to change the magnetic frustration of the α- and qubit loop independently.

gradiometric flux qubit of Fig. 3.6**d**, an applied homogeneous magnetic field does not affect the energy bias of the flux qubit but it changes Φ_α and allows for tuning of the qubit gap. The immediate consequence of the gradiometric layout is that an inhomogeneous magnetic field is required to adjust the energy bias ε of the flux qubit when needed. This inhomogeneous field can be generated by feeding a small current through the so-called ε-flux line, which couples asymmetrically to the qubit loop (cf. Fig. 3.6**d**). It generates different flux densities B in the two subloops of area $A_1 \approx A_2$ (see also Fig. 3.7**b**), leading to different amounts of total flux $\Phi_1 = \int_{A_1} B_1 \, \mathrm{d}A$ and $\Phi_2 = \int_{A_2} B_2 \, \mathrm{d}A$. This results in the

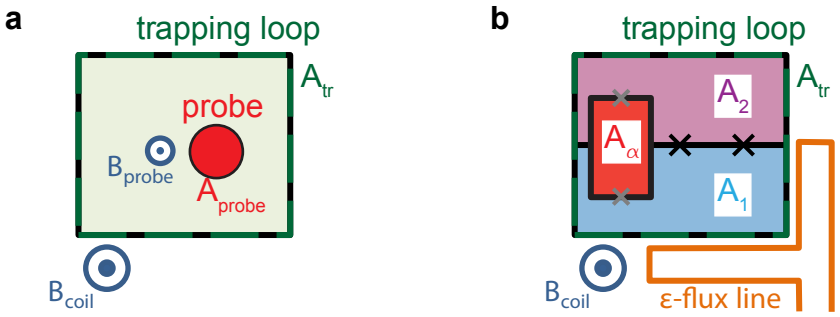

Figure 3.7: Sketch illustrating the penetration or screening of magnetic fields for **a** a probe inside the trapping loop and for **b** the experimental situation of the gradiometric tunable-gap qubit.

magnetic frustration

$$f_\mathrm{q} = f_{12} \quad = \quad \frac{\Phi_1 - \Phi_2}{\Phi_0} \tag{3.11}$$

by the ε-flux line, which is used to change the energy bias ε of the gradiometric flux qubit. Correspondingly, the deviation of f_{12} from the value $(n+\frac{1}{2})$ at the symmetry point is

$$\delta f_\mathrm{q} = \delta f_{12} \quad = \quad f_{12} - \left(n + \frac{1}{2}\right) \ . \tag{3.12}$$

Furthermore, the outer ring of the gradiometric qubit, denoted as the trapping loop, can be used to trap an integer number of magnetic flux quanta, e.g., by cooling below T_c in an applied magnetic field. This allows for a pre-biasing of the qubit near the symmetry point. We note, however, that the exact amount of flux threading the qubit loop and the α-loop, respectively, depends on the ratio of the kinetic and geometric inductances. Since an understanding of this point is important for a controlled design of a gradiometric qubit with tunable gap, it is discussed in more detail in Sec. 3.3.2. Within this work, we investigate both fixed-gap and tunable-gap gradiometric 3-JJ flux qubits. The former is an ideal model system to study the principle of flux biasing.

3.3.1 Flux trapping

Besides its reduced sensitivity to homogenous flux noise, the gradiometric layout comes with another advantage. When trapping magnetic flux in its outer loop, the so-called trapping loop (cf. Fig. 3.6**c** and Fig. 3.6**d**), the qubit can be pre-biased close to the degeneracy point. Flux biasing is based on fluxoid quantization as described in Sec. 2.2. The total magnetic flux (i.e., the fluxoid) in a closed superconducting loop such as the trapping loop is quantized in units of Φ_0 or, equivalently, the phase of the superconducting

order parameter changes by $2\pi n$ around the closed trapping loop. Therefore, in the fully symmetric gradiometric qubit designs of Fig. 3.6**c** and Fig. 3.6**d**, the trapping of an odd number $n=(2n'+1)$ $(n,n'\in\mathbb{N})$ of flux quanta in the trapping loop leads to a phase difference of $(2n'+1)\pi$ between the points A and B. This corresponds to a flux bias of $(n'+\frac{1}{2})\Phi_0$, i.e., a flux bias at the symmetry point. The flux trapping is realized by applying externally a magnetic flux close to the desired value (cf. Fig. 2.1 in Sec. 2.2) while cooling the sample into the superconducting state. In contrast to the flux bias with an external coil, which is connected to an external current source, the bias via flux trapping is, in principle, noise free. On the other hand, once a specific flux state has been frozen in, it can no longer be changed without heating the sample above T_c. Therefore, in practice flux trapping is often used for pre-biasing at an operation point, while an additional magnetic field is used for making fast changes around this operation point. In order to enable such flux control, one has to take care of the right size of kinetic and geometric inductances in the superconducting loop, which is discussed in the following subsection.

3.3.2 Effect of kinetic inductance

The relative magnitudes of kinetic and geometric inductances of the superconducting lines forming the gradiometric (tunable-gap) qubits are of great technical relevance. They determine to which extent magnetic flux actually affects the qubit or how much it is screened by the closed trapping loop. This is crucial for applying an inhomogeneous field to the qubit via the ε-line as well as for frustrating the α-SQUID when tuning the qubit gap.

In Sec. 2.2, the difference between flux and fluxoid quantization has already been explained and the kinetic inductance has been introduced. To illustrate the following considerations we use the simple Gedankenexperiment of Fig. 3.7**a**. There, an external homogenous magnetic field is applied to a superconducting loop (trapping loop), that contains a probe structure for magnetic flux inside the loop. In the special case of flux quantization, the total flux Φ inside the loop consist of the externally applied flux Φ_{ex} and the flux Φ_g generated by the circulating current in the ring due to its geometric inductance. Flux quantization requires that this total flux $\Phi=\Phi_{ex}+\Phi_g=n\Phi_0$ is always quantized in terms of the flux quantum. Therefore the probe can only experience this quantized, yet no continuously varying flux. This situation changes for the case of fluxoid quantization that holds when the width of the superconducting lines is made small enough (on the order of λ_L), which is actually the case for the structures used in this work. Then, the first term on the left hand side of Eq. (2.7) and the kinetic inductance L_k become relevant and allow for a partial penetration of the applied magnetic field. According to

Eq. (2.11), the fluxoid quantization condition reads as

$$\frac{\Phi_{\mathrm{ex}}}{\Phi_0} + \frac{L_{\mathrm{k}} I}{\Phi_0} + \frac{L_{\mathrm{g}} I}{\Phi_0} = f_{\mathrm{ex}} + f_{\mathrm{k}} + f_{\mathrm{g}} = f_{\mathrm{ex}} + f_{\mathrm{k}} + \beta f_{\mathrm{k}} = n \ , \tag{3.13}$$

where we introduce the parameter

$$\beta \equiv L_{\mathrm{g}}/L_{\mathrm{k}} = f_{\mathrm{g}}/f_{\mathrm{k}}. \tag{3.14}$$

Thus, we can solve Eq. 3.13 for

$$f_{\mathrm{k}} = \frac{n - f_{\mathrm{ex}}}{1+\beta} \, . \tag{3.15}$$

The frustration f_{k} is not associated with a magnetic field, but with the kinetic energy of the charge carriers (cf. Sec. 2.2). Thus, it does not contribute to the net frustration that is linked with the magnetic field inside the trapping loop. Nevertheless, we use Eq. 3.15 in order to calculate the net trapping loop frustration

$$f_{\mathrm{tr,net}} = f_{\mathrm{ex}} + f_{\mathrm{g}} = f_{\mathrm{ex}} + \beta f_{\mathrm{k}} = \frac{1}{1+\beta} \, f_{\mathrm{ex}} + \frac{\beta}{1+\beta} \, n \ . \tag{3.16}$$

This is the frustration effectively linked with a magnetic field $B_{\mathrm{probe}} = \Phi_0 f_{\mathrm{tr,net}}/A_{\mathrm{probe}}$ that is experienced by the probe structure inside the trapping loop. From Eq. (3.16) the influence of the kinetic inductance can be understood easily. For negligible kinetic inductance, i.e., dominant geometric inductance ($\beta \gg 1$), the situation becomes formally equivalent to the case of flux quantization. The screening by the circulating current in the trapping loop is so strong that we can no longer change the flux in the loop by varying the applied field. The frustration of the trapping loop is fixed to the value $f_{\mathrm{tr,net}} \approx n$ frozen in during cool-down.

In contrast, if the kinetic inductance is dominant ($\beta \ll 1$), the contribution of the circulating screening current is negligible and $f_{\mathrm{tr,net}} \approx f_{\mathrm{ex}}$. In this case, the superconducting lines cannot screen magnetic fields and we can change the magnetic frustration of the trapping loop and the probe continuously by varying the applied magnetic field. In this sense, β can be interpreted as a screening factor.

These considerations can now be adapted from a theoretical probe structure to the real situation of the α-loop implemented within the trapping loop (cf. Fig. 3.7**b**). The net magnetic frustration of the α-loop is, in first approximation, obtained by multiplying Eq. (3.16) with the area ratio A_α/A_{tr} of the α- and the trapping loop:

$$f_{\alpha,\mathrm{net}} = \frac{A_\alpha}{A_{\mathrm{tr}}} \, f_{\mathrm{tr,net}} \ . \tag{3.17}$$

Here, we neglect effects arising from the fact that the α-loop is not centered in the trap-

ping loop. This means that we consider the field B_{probe} to be homogenous in the area of the α-loop, whereas this assumption is not true very close to the lines of the trapping loop. Furthermore, we neglect any possible effects due to the direct galvanic connection of trapping and α-loop as such influences would be suppressed by the symmetry of the gradiometric layout. Then, the critical current of the α-loop becomes $I_{\mathrm{c},\alpha}(f_{\alpha,\mathrm{net}}) = \alpha(f_{\alpha,\mathrm{net}})I_{\mathrm{c}}$ [cf. Eq. (3.10)] with

$$\begin{aligned} \alpha(f_{\alpha,\mathrm{net}}) &= \alpha_0 \left|\cos\left(\pi f_{\alpha,\mathrm{net}}\right)\right| \\ &= \alpha_0 \left|\cos\left(\pi \frac{A_\alpha}{A_{\mathrm{tr}}} \left[\frac{1}{1+\beta} f_{\mathrm{ex}} + \frac{\beta}{1+\beta} n\right]\right)\right| . \end{aligned} \tag{3.18}$$

Of course, the limiting cases of dominant or negligible screening parameter β apply in the same way to the α-loop as discussed above. However, a value of $\beta \simeq 1$ is more realistic and also desirable for our structures. With a suitable value of β, adjusted via a suitable width of the superconducting lines, α can be varied both by changing f_{ex} via an external magnetic field and by changing the number n of flux quanta frozen into the trapping loop during cool-down. For example, n could be used for pre-biasing at a specific α value and the external magnetic field provided by a current sent through an on-chip control line for small variations around this value. The pre-biasing with trapped flux has the advantage that it is not affected by the noise added by the current source, while the variations with the on-chip control line can be very fast.

For zero applied magnetic field, Eq. (3.18) reduces to

$$\alpha(f_{\alpha,\mathrm{net}})|_{f_{\mathrm{ex}}=0} = \alpha_0 \left|\cos\left(\pi \frac{A_\alpha}{A_{\mathrm{tr}}} \frac{\beta}{1+\beta} n\right)\right| . \tag{3.19}$$

This expression applies to the experimental situation, where an odd number $n = (2n' + 1)$ of flux quanta is frozen into the trapping loop to bias the gradiometric flux qubit at its symmetry point and no additional external magnetic field is applied. Fixing $\alpha_0 \simeq 1$ by the fabrication process, we can change the number of trapped flux quanta to choose α in the desired regime $0.5 < \alpha < 1$. Of course, flux trapping only allows for a step-wise variation of α. For continuous and fast variations of α, magnetic fields generated by an external coil or on-chip control lines have to be used. For a typical value of $\beta \simeq 0.8$, we obtain $f_{\alpha,\mathrm{net}} \simeq 0.08\, n$ for $f_{\mathrm{ex}} = 0$. This calculation shows that we need only a small number of trapped flux quanta to significantly modify α. Furthermore, we obtain $f_{\mathrm{tr,net}} = 0.55 f_{\mathrm{ex}}$ for $n = 0$, meaning that about half of the applied magnetic flux is effectively frustrating the α-loop and thus changing the qubit gap Δ.

Finally we note, that for the frustration of the qubit the situation is qualitatively similar but quantitatively a bit more complex. The qubit frustration $f_{\mathrm{q}} \equiv f_{12} = f_1 - f_2$ depends on the exact spatial distribution of the inhomogeneous field generated by the

ε-line. Nevertheless, the screening or penetration of this field depends analogously on the value of the screening parameter β.

3.3.3 The gradiometer quality

A perfect gradiometer should be completely insensitive to a homogeneous magnetic field. However, in reality there are always imperfections such as slight differences of the areas A_1 and A_2 of the two subloops of the eight-shaped gradiometer and/or of the geometric inductances L_{g1} and L_{g2} and kinetic inductances L_{k1} and L_{k2} of the superconducting lines forming the subloops. Due to these imperfections there is a finite imbalance δf_{imb} of the magnetic frustration of the two subloops. According to Eq. (3.13), δf_{imb} can be expressed as

$$\begin{aligned} \delta f_{\mathrm{imb}} &= \delta f_{\mathrm{ex}} + \delta f_{\mathrm{g}} + \delta f_{\mathrm{k}} = \frac{\delta\Phi_{\mathrm{ex}}}{\Phi_0} + \frac{\delta\Phi_{\mathrm{g}}}{\Phi_0} + \frac{\delta\Phi_{\mathrm{k}}}{\Phi_0} \\ &= \frac{\Phi_{\mathrm{ex}}}{\Phi_0}\frac{\delta A}{A} + \frac{I\delta L_{\mathrm{g}}}{\Phi_0} + \frac{I\delta L_{\mathrm{k}}}{\Phi_0} \,. \end{aligned} \tag{3.20}$$

With $I = (n - f_{\mathrm{ex}})\Phi_0/(L_{\mathrm{g}} + L_{\mathrm{k}})$ we can rewrite this expression to

$$\delta f_{\mathrm{imb}} = f_{\mathrm{ex}} \underbrace{\left(\frac{\delta A}{A} - \frac{\delta L_{\mathrm{g}} + \delta L_{\mathrm{k}}}{L_{\mathrm{g}} + L_{\mathrm{k}}}\right)}_{\equiv 1/Q_{\mathrm{grad,ex}}} + n \underbrace{\left(\frac{\delta L_{\mathrm{g}} + \delta L_{\mathrm{k}}}{L_{\mathrm{g}} + L_{\mathrm{k}}}\right)}_{\equiv 1/Q_{\mathrm{grad,n}}} \,. \tag{3.21}$$

The total gradiometer quality Q is given by $Q^{-1} = Q^{-1}_{\mathrm{grad,ex}} + Q^{-1}_{\mathrm{grad,n}}$. The first term describes imbalances of the frustration when a homogeneous external field is applied, and the second those when an integer number of flux quanta is frozen in. Obviously, the higher the Q the lower is δf_{imb}. As it is shown in Sec. 5.2.3, Q values on the order of 500 are feasible for fixed-gap gradiometric qubits. In Sec. 5.3.3, we explore, to which extent the implementation of an α-loop affects the gradiometer quality.

3.4 Circuit QED

Having introduced both superconducting harmonic resonators (cf. Sec. 2.6) and persistent current flux qubits, they are now combined in structures used in circuit quantum electrodynamics (QED). The fascinating and rapidly growing field of circuit QED is often referred to as *quantum optics on a chip*, which emphasizes its analogy to cavity QED. There, single atoms interact with the quantized electromagnetic field inside a 3D optical or microwave cavity. In our solid-state analog, superconducting qubits as artificial atoms are coupled to superconducting resonators. For a flux qubit, the physical properties of

these combined qubit-resonator system are described by the Hamiltonian

$$\hat{H} = \hbar\omega_\mathrm{r}\left(\hat{a}^\dagger\hat{a} + \frac{1}{2}\right) + \frac{1}{2}\hbar\varepsilon\hat{\sigma}_z - \frac{1}{2}\hbar\Delta\hat{\sigma}_x + \hbar g\hat{\sigma}_z\left(\hat{a}^\dagger + \hat{a}\right) . \tag{3.22}$$

Here, the first term equals the resonator Hamiltonian of Eq. (2.37), second and third term the one of the qubit in Eq. (3.5). The fourth term describes the essential interaction between qubit and resonator field $\hat{a}^\dagger + \hat{a}$ with a coupling rate

$$g = MI_\mathrm{p}I_\mathrm{r}/\hbar . \tag{3.23}$$

The latter stems from the interaction between the qubit persistent current I_p and the resonator vacuum current I_r mediated by the qubit-resonator mutual inductance M. In circuit QED, the important strong coupling limit, where the coupling rate g exceeds the loss rates γ and κ of qubit and resonator, respectively, can be reached straightforwardly. In this limit, the coherent exchange of an excitation between qubit and resonator is experimentally accessible. Furthermore, the general Hamiltonian of Eq. (3.22) can be simplified by a base transformation and a rotating wave approximation (RWA) to the renowned Jaynes-Cummings-Hamiltonian [67]

$$\hat{H}_\mathrm{JC} = \hbar\omega_\mathrm{r}\left(\hat{a}^\dagger\hat{a} + \frac{1}{2}\right) + \frac{1}{2}\hbar\omega_\mathrm{q}\hat{\sigma}_z + \hbar g\sin\theta\left(\hat{a}^\dagger\hat{\sigma}_- + \hat{a}\hat{\sigma}_+\right) . \tag{3.24}$$

Again, the first term describes the resonator and the second one the qubit with its flux dependent transition frequency ω_q given by Eq. (3.8). The third term with $\theta = \arctan(\Delta/\varepsilon)$ and the qubit raising and lowering operators $\hat{\sigma}_+ \equiv |\mathrm{e}\rangle\langle\mathrm{g}|$ and $\hat{\sigma}_- \equiv |\mathrm{g}\rangle\langle\mathrm{e}|$, respectively, corresponds to the Jaynes-Cummings interaction. The RWA is only valid for $\omega_\mathrm{r} + \omega_\mathrm{q} \gg g, |\omega_\mathrm{r} - \omega_\mathrm{q}|$, which is well fulfilled for the measurements presented in this work. Only when the coupling strength g reaches a considerable portion $g/\omega_\mathrm{r} \gtrsim 0.1$ the RWA is no longer sufficient to describe the physics of this so-called ultrastrong coupling regime [34].

Due to the qubit-resonator interaction including off-diagonal terms, the qubit ground and excited states $|\mathrm{g}\rangle$ and $|\mathrm{e}\rangle$ as well as the photon number state $|N\rangle$ of the resonator are no longer eigenstates of the Hamiltonian of Eq. (3.24). The new eigenstates – the so-called dressed states of the joint qubit-resonator system – are the superpositions [68]

$$\begin{aligned} |-,N\rangle &= \cos\Theta\,|\mathrm{g},N\rangle - \sin\Theta\,|\mathrm{e},N-1\rangle \text{ and} \\ |+,N\rangle &= \sin\Theta\,|\mathrm{g},N\rangle + \cos\Theta\,|\mathrm{e},N-1\rangle , \end{aligned} \tag{3.25}$$

where $\Theta = 1/2\arctan(2g\sqrt{N}/\delta)$ is the photon-number dependent mixing angle with the

qubit-resonator detuning $\delta = \omega_\mathrm{q} - \omega_\mathrm{r}$. The latter is used to distinguish two different experimental regimes.

Resonant regime

For vanishing detuning $\delta \simeq 0$, the qubit transition frequency very well matches the resonator frequency and energy is coherently exchanged between qubit and resonator. For the special case of $\delta = 0$, the eigenstates of Eq. (3.25) turn to the symmetric and antisymmetric superpositions

$$|\pm,N\rangle = \frac{1}{\sqrt{2}} \left(|\mathrm{g},N\rangle \pm |\mathrm{e},N-1\rangle \right) , \tag{3.26}$$

which is analogous to the formation of flux qubit eigenstates in Eq. (3.7). Figure 3.8**a** shows the so-called Jaynes-Cummings ladder, which is very instructive to visualize the dressed eigenstates. The uncoupled states $|\mathrm{g},N\rangle$ and $|\mathrm{e},N-1\rangle$ are energetically degenerate. However, due to the interaction, the mixed states $|\pm,N\rangle$ split by an amount of $2\hbar g \sin\theta\sqrt{N}$, forming doublets. For $N = 1$, this leads to the situation where a single photon can be coherently exchanged at a frequency $2g \sin\theta$, the vacuum Rabi frequency. As stated before, this interpretation holds only in the strong coupling regime. As the qubit transition frequency is flux dependent according to Eq. (3.8), the application of magnetic flux tunes the system away from the resonant regime. Moreover, for a large bias energy $\varepsilon \gg \Delta$, the angle θ in Eq. (3.24) approaches zero and thus, the interaction strength becomes vanishingly small. In this flux regime, the uncoupled qubit and resonator states are again the eigenstates of the system. From an experimental point of view, we expect the appearance of an avoided crossing (anticrossing) in the flux dependent spectrum of qubit and resonator due to the formation of the Jaynes-Cummings doublets. This effect is clearly visible in the experimental data in Chapter 6.3.

Dispersive regime

When qubit and resonator are significantly detuned, i.e., $|\delta| \gg g$, there is no longer a coherent exchange of excitations between them. However, qubit and resonator still interact via virtual photons, which leads to a dispersive shift of the energy levels as shown in Fig. 3.8**b**. In this regime, the Jaynes-Cummings Hamiltonian of Eq. (3.24) can be approximated via a unitary transformation [69] to the dispersive Hamiltonian

$$\hat{H}_\mathrm{disp} = \hbar \left(\omega_\mathrm{r} + \frac{g^2 \sin^2\theta}{\delta} \hat{\sigma}_z \right) \left(\hat{a}^\dagger \hat{a} + \frac{1}{2} \right) + \frac{1}{2} \hbar \omega_\mathrm{q} \hat{\sigma}_z \, . \tag{3.27}$$

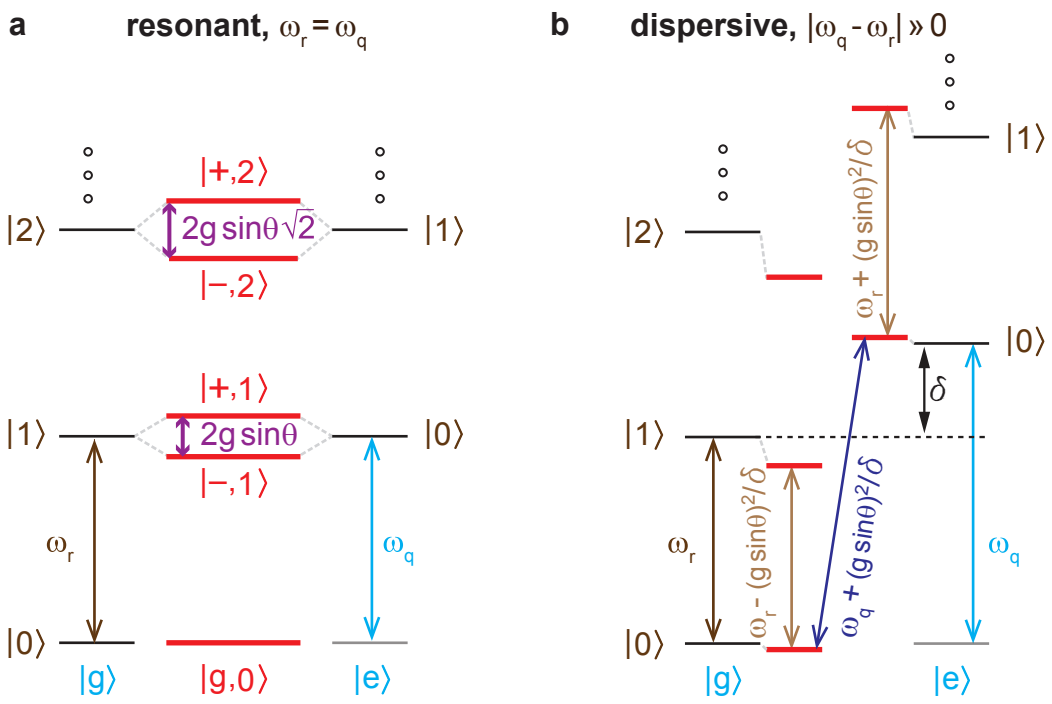

Figure 3.8: Jaynes-Cummings ladder: Energy level diagram illustrating the change from uncoupled qubit and resonator levels (black lines) to the coupled system following the Jaynes-Cummings Hamiltonian (red lines). **a** Resonant case. **b** Dispersive limit.

In this notation, the system can be interpreted as an uncoupled qubit (second term) and a resonator with an effective resonant frequency $\omega_\mathrm{r} \pm \frac{g^2 \sin^2\theta}{\delta}$, that is dependent on the state of the qubit. In this way, the qubit can be measured by observing its influence on the dispersive shift of the resonator, which is the basis for the two-tone-spectroscopy of the qubit (cf. Sec. 4.4.2 and Sec. 6.3). Furthermore, this is the basis for a quantum non-demolition (QND) readout of the qubit with the resonator[70–74]. Alternatively, one can rewrite this Hamiltonian in the form

$$\hat{H}_\mathrm{disp} = \hbar\omega_\mathrm{r}\left(\hat{a}^\dagger\hat{a} + \frac{1}{2}\right) + \frac{1}{2}\hbar\tilde{\omega}_\mathrm{q}\hat{\sigma}_z \tag{3.28}$$

with

$$\tilde{\omega}_\mathrm{q} = \omega_\mathrm{q} + \frac{2g^2\sin^2\theta}{\delta}\hat{a}^\dagger\hat{a} + \frac{g^2\sin^2\theta}{\delta}\,. \tag{3.29}$$

In this form, the system appears as an uncoupled resonator (first term) and a qubit with modified frequency $\tilde{\omega}_\mathrm{q}$. The latter contains two contributions of dispersive shift: The term $g^2\sin^2\theta/\delta$ is a constant shift, which is the analog to the Lamb-shift in atomic physics. The other term $2g^2\sin^2\theta\hat{a}^\dagger\hat{a}/\delta$ is associated with an ac-Zeeman shift of the qubit. Due to its dependence on the photon number $N = \langle\hat{a}^\dagger\hat{a}\rangle$ in the resonator, the ac-Zeeman shift of the qubit can be used to calibrate the power inside the resonator (cf. Sec. 6.2.3).

Finally, we note that both resonant and dispersive limit are important because they allow for an extraction of important qubit parameters from the measurement data in Chapter 6 using analytical formulas. Nevertheless, we also use the full Jaynes-Cummings-Hamiltonian from Eq. (3.24) to fit the qubit-resonator spectrum in both resonant and dispersive regime in Sec. 6.3.

Chapter 4

Experimental techniques

Superconducting quantum circuits require sophisticated fabrication and measurement techniques. In particular, the JJs of the flux qubit with sub-micron lateral dimensions need to be fabricated with electron beam lithography. Furthermore, the comparably high current densities can only be achieved with a well-controlled oxidation process under UHV conditions. All samples characterized in this thesis have been fabricated at WMI facilities. They are based on aluminum thin film structures and Al/AlO_x/Al Josephson junctions fabricated by electron beam lithography and two-angle shadow evaporation on thermally oxidized silicon wafers. Although the author of this thesis has put great effort on a reproducible and continuously improved sample fabrication, we refer to Ref. [75] for an overview of the fabrication process. Further fabrication details of gradiometric tunable-gap qubits can be found in the work of Ref. [76], which was conducted under supervision of the author of this thesis.

In this chapter, we first focus on the pre-characterization of JJs in Sec. 4.1. Next, we investigate the principle of phase-biasing in Sec. 4.2. The measurement setups used in the following chapters for qubit characterization are described in Sec. 4.3 and Sec. 4.4.

4.1 Characterization of Josephson junctions

A thorough pre-characterization of the JJs later forming the flux qubit is of great importance, mainly for two reasons. First, the successful implementation of a flux qubit poses strong requirements on the JJ parameters. The relevant parameters E_c, E_J and α – linked with the more fundamental JJ parameters capacitance C, critical current I_c and areas A and A_α, respectively – have to lie within certain margins for a working flux qubit (cf. Sec. 3.1). However, they are subject to unavoidable uncertainties within the fabrication process. Second, the measurement of flux qubits at millikelvin temperatures takes considerable experimental effort, time and money (e.g., for liquid helium). Therefore, we pre-characterize the JJs to a reasonable extent by means of electrical and imaging measurements.

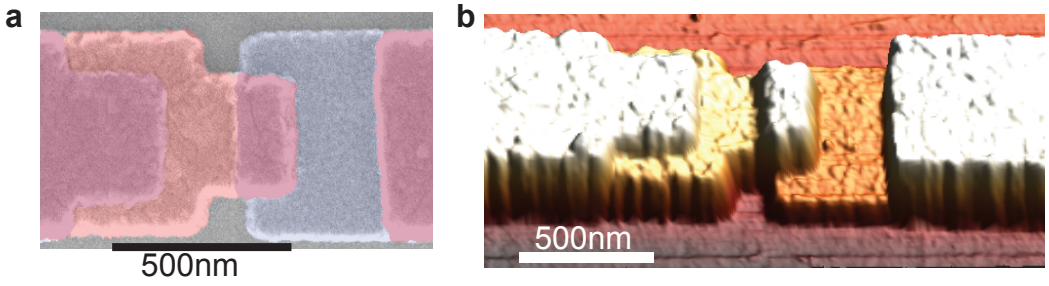

Figure 4.1: **a** SEM image (top view) of one of our Al-AlOx-Al JJs. Bottom Al layer (blue) and top Al layer (red) overlap to form the JJ (purple rectangle in the middle). **b** AFM image of a JJ (displayed at an angle of 45°) visualizing the 3D structure of the 40 nm and 70 nm thick Al layers.

4.1.1 SEM and AFM imaging of JJs

We first shortly describe the methods used for imaging the JJs, which give us access to their cross-sectional areas. Since we assume the critical current density to be the same for all three qubit junctions, the size of the α-JJ by definition determines the value of α. As the qubit gap Δ depends exponentially on α [cf. Eq. (3.9)], the ratio of areas should be known as precisely as possible. A precisely controlled junction size is particularly crucial for fixed-gap flux qubits; it is actually one big advantage of tunable-gap flux qubits that fabrication uncertainties can be overcome. Nevertheless, the maximum value α_0 of a tunable α-loop should be adjusted properly. Furthermore, the absolute size of the JJs determines critical current and capacitance and, thus, the relevant energies E_J and E_c (cf. Sec. 2.3.3). In the complex electron beam fabrication process, the area of a JJ is exposed to inevitable variations in, e.g., electron beam focus or resist development. Therefore, we typically image the JJs after every fabrication run. Our standard technique for this is taking a scanning electron microscope (SEM) image of the JJs as depicted in Fig. 4.1**a**. However, as the exposition of the JJ's oxide barrier to the charging by an electron beam might cause electrical breakthrough, SEM imaging is only applied to additional test JJs located on the sample or only after the full characterization of the JJ. Recently, we have also used atomic force microscopy (AFM) to image JJs as shown in Fig. 4.1**b**. From this technique we can also determine the junction area and furthermore learn about topological properties such as surface roughness [77]. As AFM was proven to be non-destructive for our JJs [78], it can even be used to pre-characterize the junctions before further measurements.

4.1.2 Low temperature IV characteristic

Apart from a rough determination of its area, the most important characterization of a JJ involves an electrical measurement in the superconducting state in order to determine

the main junction properties. To this end, the JJ needs to be connected with electrical feed lines. However, the flux qubits themselves cannot be connected with wires as this would introduce an enormous amount of noise spoiling the quantum mechanical behavior. Before a real qubit characterization, the parameters of the qubit junctions can therefore only be deduced from additional test JJs fabricated on the same chip. This procedure is justified as the oxidation process, which determines the critical current density of the JJs, is the same for all JJs fabricated in the same run. We take care that the lithography process is controlled adequately in order to yield, e.g., comparable junctions areas.

In fact, the JJs we characterize are always implemented in a dc-SQUID wired for a four-point measurement. One main experimental part of this work (cf. Chapter 5) deals with flux qubits with a SQUID readout, which is explained in detail in Sec. 4.3. For these samples it is obvious to pre-characterize the readout SQUID in order to ensure the function of the readout device as well as to check the qubit junction properties. For the experiments on qubits integrated in a circuit QED layout (cf. Chapter 6), such a SQUID is added for testing purposes at the edge of the microwave resonator chip. The cryogenic measurement of these SQUIDs is performed at a temperature of approximately 500 mK inside a well-shielded ^{3}He evaporation cryostat. The details of this setup are described in detail in Ref. [79] and Ref. [80].

Before showing low-temperature data, it must be stated that we have also established the measurement of the JJs' room temperature resistance to identify samples with electrical breakthrough of the oxide layer. This measurement works best when the samples are already connected to the sample holder of the cryostat profiting from a stable electrical connection via bonding wires and from proper filtering of the feed lines (in contrast to irreproducible results obtained when using a wafer prober). As it turns out, we can clearly distinguish damaged JJs with a room temperature resistance below 100 Ω from properly working JJs with resistances of 200 Ω to 300 Ω corresponding to a critical current density $j_c(500\,\mathrm{mK}) \simeq 2\,\mathrm{kA/cm^2}$ for a typical junction size of $A_\mathrm{J} \simeq 0.03\,\mu\mathrm{m}^2$. Thereby it must be noticed that these resistance values not only contain the JJ resistance but also that of additional aluminum on-chip lines, which do not contribute in the superconducting state. More details of our measurements can be found in the appendix of Ref. [76]. Further investigations at the WMI of the room temperature resistance for a whole range of current densities were made in Ref. [78].

IV characteristic of dc-SQUIDs

We now turn to the low-temperature measurements of dc-SQUIDs. As already mentioned, dc-SQUIDs are pre-characterized at a temperature of 500 mK. If the sample passes this test and is cooled down in a dilution refrigerator (cf. Sec. 4.3), the SQUID is, of

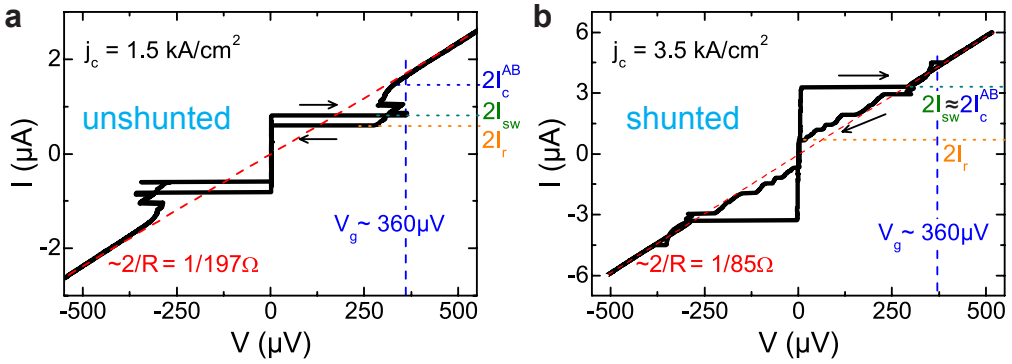

Figure 4.2: IV characteristics measured at $T = 30\,\mathrm{mK}$ and for zero applied magnetic field (i.e., $f_{\mathrm{SQ}} = 0$) for two dc-SQUIDs: **a** An underdamped and unshunted dc-SQUID with only slight hysteresis ($I_{\mathrm{sw}}/I_{\mathrm{r}} = 1.38$). **b** A dc-SQUID with additional shunt capacitors shows a more pronounced hysteresis with $I_{\mathrm{sw}}/I_{\mathrm{r}} = 5.02$.

course, characterized again. Since these measurements at 30 mK yield more meaningful results on JJ properties, they are shown here. Figure 4.2**a** shows a typical current-voltage curve for one of our readout SQUIDs at 30 mK without any applied magnetic field, i.e., $f_{\mathrm{SQ}} = 0$. The curve basically follows the theoretical expectation for an underdamped JJ as discussed in Sec. 2.3.5: With the bias current increasing from zero, no voltage drop across the SQUID is measured (superconducting state) up to a current of $2I_{\mathrm{sw}} = 0.80\,\mu\mathrm{A}$. Then, a sudden voltage drop corresponding to the gap voltage $V_{\mathrm{gap}} = 360\,\mu\mathrm{V}$ of Al appears followed by a linear region determined by the normal resistance $R_{\mathrm{n}}/2 = 197\,\Omega$. When the current is again decreased below $2I_{\mathrm{c}}$, the SQUID remains in the voltage state until the retrapping current $2I_{\mathrm{r}} = 0.58\,\mu\mathrm{A}$ is reached. This hysteretic behavior results from a low damping of the JJs. The intermediate regime between $2I_{\mathrm{c}}$ and $2I_{\mathrm{r}}$ features a complex nonlinear characteristic dominated by quasiparticle tunnelling.

The measured value for the gap voltage is close to the theoretical gap voltage $V_{\mathrm{gap}}^{\mathrm{BCS}} = 1.764 k_{\mathrm{B}} T_{\mathrm{c}} = 365\,\mu\mathrm{V}$ with the bulk value $T_{\mathrm{c}} = 1.2\,\mathrm{K}$, suggesting a good quality of our aluminum thin films. From the gap voltage we determine the upper limit for the critical current from the Ambegaokar-Baratoff relation, Eq. (2.26), to $2I_{\mathrm{c}}^{\mathrm{AB}} = 1.45\,\mu\mathrm{A}$, which coincides well with the onset of the linear regime. Furthermore, we can use a value for the junction area $A_{\mathrm{J}} = 0.028\,\mu\mathrm{m}^2$ – determined by SEM microscopy of several JJs fabricated on the same chip in the vicinity of this sample – in order to calculate the critical current density $j_{\mathrm{c}} = 1.3\,\mathrm{kA/cm}^2$. As the latter is independent of the JJ area, it is more directly related to the properties (mainly the thickness) of the JJ's oxide barrier.

For comparison, Fig. 4.2**b** shows the IV characteristic of another dc-SQUID, that is modified for an optimized readout device for qubits (cf. Sec. 4.3). With the implementation of large capacitors to ground in parallel with the SQUID, the total capacitance of the dc-SQUID as LCR resonator is significantly enlarged. As this corresponds to a

larger mass of the phase particle, the shunted dc-SQUID experiences less damping and its hysteresis is much more pronounced. A strong hysteretic behavior prevents the SQUID – once it has switched to the voltage state – from an unwanted return to the superconducting state due to current fluctuations. In this way, the readout fidelity of a dc-SQUID is improved. Due to a shorter oxidation time, the critical current density $j_c = 3.5\,\mathrm{kA/cm^2}$ is increased. Also larger SQUID junction areas contribute to a higher critical current $2I_{sw} = 3.29\,\mu\mathrm{A}$. Thus, a stronger modulation of the switching current with magnetic flux also contributes to better readout sensitivity. Moreover, the maximum switching current is practically identical to the calculated $2I_c^{AB} = 3.3\,\mu\mathrm{A}$, benefiting from the filtering properties of the shunt capacitors.

With the critical current extracted from the IV characteristic, we can also calculate the Josephson energy $E_J = \Phi_0 I_c/2\pi$ [cf. Eq. (2.19)], which is essential to estimate the behavior of the qubit made in the same fabrication process. For the two samples shown here, we obtain $E_J/h \simeq 200\,\mathrm{GHz}$ and $E_J/h \simeq 800\,\mathrm{GHz}$ for the JJs of the unshunted and the shunted SQUID, respectively. Note, that these two SQUIDs are the ones belonging to the two gradiometric tunable-gap qubits characterized in Sec. 5.3. There, the E_J values from the SQUID characterization are used again in order to consistently analyse the qubit spectroscopy data. However, besides the Josephson energy E_J also the charging energy E_c influences the qubit properties. To determine the latter, an investigation of the junction capacitance is necessary.

Josephson junction capacitance

The capacitance of a JJ determines, together with critical current I_c and normal resistance R, the behavior of a real JJ or SQUID as discussed within the RCSJ model (cf. Sec. 2.3.4). Consequently, the capacitance can also be evaluated from a current-voltage characteristic for certain junction conditions. Either the shape of the hysteresis or special features originating from junction resonances [81–84] can be studied. For the latter, separate dc-SQUIDs with larger geometric inductance would have been needed. Therefore, we investigate the hysteresis of existing SQUIDs to determine the JJ capacitance.

The hysteresis of the IV curve reflects the damping of the JJs and is described by the Stewart-McCumber parameter $\beta_C \propto C$ of Eq. (2.24) [1]. A direct access to the capacitance C is possible by determining β_C. The latter can be extracted from the ratio $a_0 = I_r/I_c$ of retrapping and critical current of underdamped JJs. To this end, the junction must not be shunted with an additional capacitance as this would change the retrapping current. The exact dependence $\beta_C(a_0)$ can only be calculated numerically starting from the equation of motion, Eq. (2.22). However, this numerical solution can be approximated very well

[1] Note that the dimensionless β_C given by Eq. (2.24) is the same for a (symmetric) dc-SQUID consisting of two identical JJs as for each single JJ.

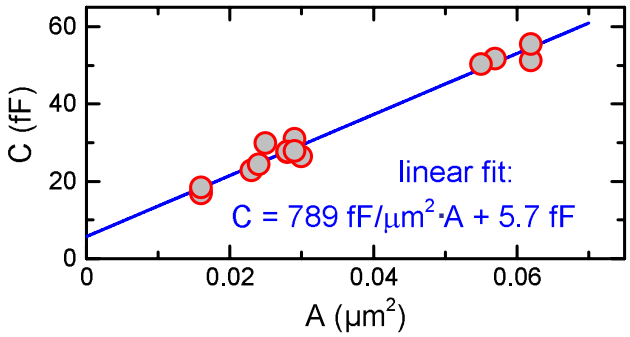

Figure 4.3: Capacitance C of Josephson junctions determined from hysteretic IV characteristics plotted versus the junction area A. From a linear fit (blue line) to the data we determine a specific capacitance $c_s \simeq 790\,\mathrm{fF}/\mu\mathrm{m}^2$.

with the analytical expression [85]

$$\beta_C = \frac{2-(\pi-2)a_0}{a_0^2} \tag{4.1}$$

when $a_0 = 0.3...0.6$, which is fulfilled for the JJs we investigate in this context. Then, the capacitance can be calculated from Eq. (4.1) and Eq. (2.24), with the parameters I_c, I_r and R directly determined from a current-voltage characteristic as the one shown in Fig. 4.2**a**. Figure 4.3 shows the capacitance of several unshunted and underdamped dc-SQUIDs determined in this manner. The capacitance is plotted versus the JJ area so that the slope of a linear fit to the data yields the specific capacitance $c_s \simeq 790\,\mathrm{fF}/\mu\mathrm{m}^2$. This value is in agreement with the simple estimation of $c_s = \epsilon_0\epsilon_r/d$ of a plate capacitor with a relative permittivity $\epsilon_r \simeq 10$ for aluminum oxide [86], and with an oxide thickness $d \simeq 1.2\,\text{Å}$. It must however be stated that this value for the specific capacitance is about eight times higher than a value determined previously on comparable JJs via SQUID resonances [81]. Nevertheless, the correctness of the determined value is confirmed later on. With this specific capacitance, we calculate a charging energy $E_c/h \simeq 1\,\mathrm{GHz}$. As it is shown during the analysis of (tunable-gap) qubits in Chapter 5, this value for E_c is very well suited to describe the measured behavior of the qubit gap [cf. Eq. (3.9)].

4.2 Phase-bias by flux trapping

After the pre-characterization of JJs in the previous section, we now investigate some properties of the superconducting loops. As discussed in Sec. 2.2, a knowledge of the geometric and kinetic inductances L_k and L_g, respectively, is of great practical relevance for the frustration of superconducting loops. In Sec. 4.2.1, we estimate these values with the help of phase-biased SQUIDs. The basic principle of this phase-biasing is closely

connected to the flux trapping for qubit biasing, that is described in Sec. 4.2.2. Before, we want to comment shortly on the technical procedure of flux trapping. The typical sequence is as follows: A certain magnetic field is applied to the sample via an external coil. Then, the sample is heated above the critical temperature of aluminum for a time not longer than a few seconds. When the sample has returned to the superconducting state the magnetic bias field can be removed. The exact details of how the sample is heated – either by heating the whole sample stage or by locally heating at the sample itself – depend on the used cryostat and are described in detail in the appendix of Ref. [76].

4.2.1 Phase-biased SQUIDs

In the work of Ref. [76], which was conducted under supervision of the author of this thesis, we extensively studied phase-biased SQUIDs; here, we shortly recapitulate the basic principle and main results. A phase-biased SQUID [87] denotes a dc-SQUID that contains an additional superconducting loop for flux trapping as depicted in Fig. 4.4**a**. Depending on the length of the shared segment a with respect to the total trapping loop circumference s, the kinetic phase difference $\phi_{\mathrm{k,SQ}}$ of the SQUID contains an additional part $(a/s)\phi_{\mathrm{k,tr}}$. Besides, the trapping loop adds an additional frustration to the SQUID loop via a mutual inductance M_{g} between trapping and SQUID loop. In total, the flux-dependent switching current of the SQUID is modified from Eq. (2.28) to

$$I_{\mathrm{sw}}(f_{\mathrm{SQ}},n) = 2I_{\mathrm{c}}\left|\cos\left(\pi f_{\mathrm{SQ}}\left[1+\kappa\frac{A_{\mathrm{tr}}}{A_{\mathrm{SQ}}}\right]-\kappa\pi n\right)\right|, \tag{4.2}$$

where

$$\kappa = \frac{\frac{a}{s}+\frac{M_{\mathrm{g}}}{L_{\mathrm{k}}}}{1+\beta} \tag{4.3}$$

and $A_{\mathrm{SQ}}/A_{\mathrm{tr}}$ is the ratio of SQUID area to trapping loop area. Equation (4.2) implies that the periodicity in magnetic frustration of I_{sw} is changed by the factor $(1+\kappa A_{\mathrm{tr}}/A_{\mathrm{SQ}})$ and that the I_{sw}-curve is shifted stepwise by $\kappa\pi n$. If A_{tr} is small compared to A_{SQ}, the ratios $M_{\mathrm{g}}/L_{\mathrm{g}}$ and a/s are equal so that $\kappa \approx a/s$, which can be used to bias a SQUID exactly at a phase π using $a/s = 0.5$ [87]. We demonstrated the realization of both SQUIDs with a bias of π $(a/s = 0.5)$ and with a bias of $\pi/2$ $(a/s = 0.25)$ [76].

The value of κ can be determined with Eq. (4.2) in two ways: First, the periodicity of $I_{\mathrm{sw}}(f_{\mathrm{SQ}})$ is compared for one SQUID with trapping loop and one reference SQUID without. Second, the shift of the $I_{\mathrm{sw}}(f_{\mathrm{SQ}},n)$ curve is determined for several numbers n of trapped flux quanta. Measurement data for both methods are shown in Fig. 4.4**b** and Fig. 4.4**c**, respectively. Both measurements consistently yield $\kappa = 0.180 \pm 0.002$. However, we cannot determine β directly from these measurements because of the unknown M_{g}

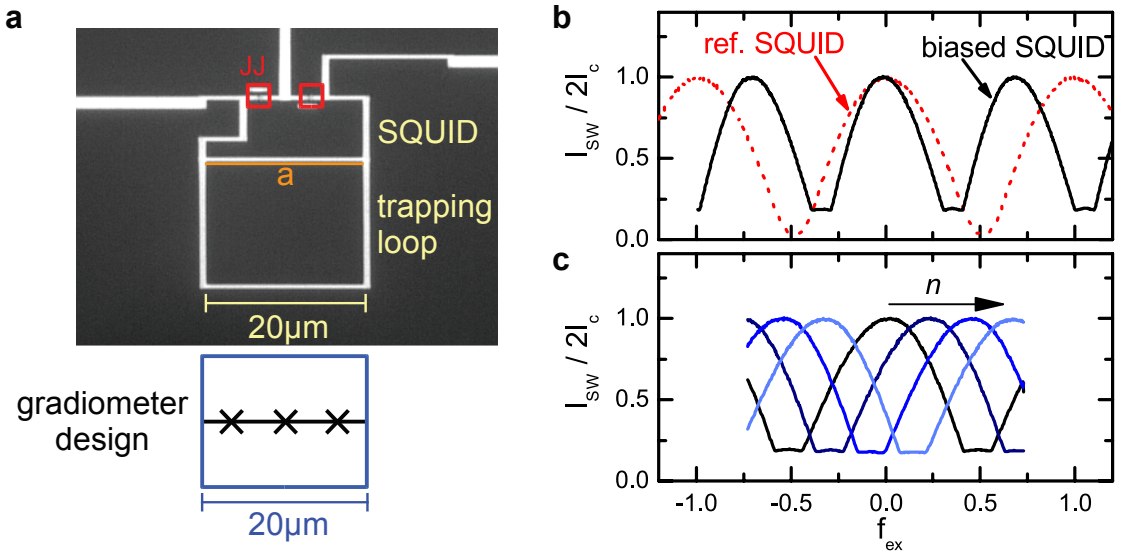

Figure 4.4: Phase-biased SQUID: **a** Optical micrograph of a phase-biased SQUID, where the trapping loop has the same dimensions as the one used for all gradiometric qubits in this work (sketch on the lower part). **b** Change of the periodicity of $I_{\mathrm{sw}}(f_{\mathrm{ex}})$ for a phase-biased SQUID compared to a reference SQUID without trapping loop. **c** Shift of the $I_{\mathrm{sw}}(f_{\mathrm{ex}})$ curve for increasing number n of trapped flux quanta.

and L_{k} in Eq. (4.3).

In order to estimate the kinetic inductance of the superconducting lines we use the dirty limit expression $L_{\mathrm{k}} = \hbar\rho_{\mathrm{n}}\ell/\pi\Delta_0 S$ [88, 89], where $\Delta_0 = 0.18\,\mathrm{meV}$ is the zero temperature energy gap of Al. The use of this expression is justified, since the mean free path in our 90 nm thick Al films is limited by the film thickness and therefore is much smaller than the coherence length $\xi \simeq 1.5\,\mu\mathrm{m}$ of Al. The normal resistivity ρ_{n} is determined by suitable test structures fabricated on the same chip. For the cross-sectional area $S = 500 \times 90\,\mathrm{nm}^2$ of the superconducting line forming the trapping loop, we obtain a kinetic inductance per unit length of $L_{\mathrm{k}}/\ell \simeq 1\,\mathrm{pH}/\mu\mathrm{m}$, resulting in $L_{\mathrm{k}} = 70\,\mathrm{pH}$ for the trapping loop of Fig. 4.4**a**. Furthermore, the geometric inductance L_{g} of the superconducting loop can be calculated according to Ref. [90] to $L_{\mathrm{g}} \simeq 57\,\mathrm{pH}$. This results in $\beta \simeq 0.81$. Then, Eq. (4.3) is used to make a consistency check. The resulting value of $M_{\mathrm{g}} = 3.3\,\mathrm{pH}$ is plausible with respect to the maximum expected value $(a/s)L_{\mathrm{g}} = 16\,\mathrm{pH}$.

Although the above discussion can only give a rough estimate for β, it is very helpful to predict the approximate behavior of the trapping loop of the qubit as discussed in Chapter 5, especially the net frustration of the α-loop [cf. Eq. (3.16) and (3.17)]. A more accurate determination of β is performed in Sec. 5.3.2 from spectroscopy data on a gradiometric tunable-gap qubit. The investigation of phase-biased SQUIDs also demonstrates the successful trapping of flux quanta, which we transfer to the biasing of gradiometric qubits in the following subsection.

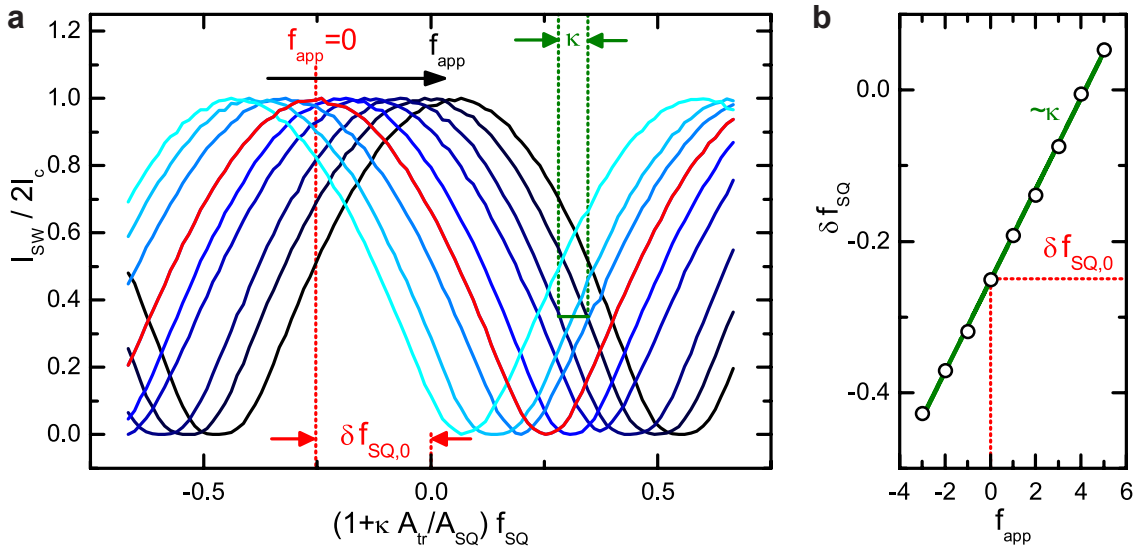

Figure 4.5: Flux trapping in a gradiometric qubit loop: **a** The $I_{\mathrm{sw}}(f_{\mathrm{ex}})$ curve of the readout SQUID measured at 35 mK is shifted for different numbers of trapped flux quanta. **b** The shift δf_{SQ} of the $I_{\mathrm{sw}}(f_{\mathrm{ex}})$ curve plotted versus the applied frustration f_{app} shows the discrete steps characteristic for fluxoid quantization.

4.2.2 Flux trapping in the qubit loop

We now turn to the trapping of flux quanta in the outer loop of a gradiometric flux qubit as introduced theoretically in Sec. 3.3.1. A real layout of such a sample is shown in Fig. 5.3. Essentially, the difference concerning flux trapping to the previous subsection on phase-biased SQUIDs is the fact, that SQUID and trap loop do not share a common line segment. Consequently, Eq. (4.2) and Eq. (4.3) are also valid here after setting $a = 0$. Thus, the trapping of different numbers n of flux quanta also results in shifted $I_{\mathrm{sw}}(f_{\mathrm{SQ}},n)$ curves of the readout SQUID. Effectively, this shift can be attributed to the additional flux in the SQUID loop generated via the mutual inductance by the circulating current

$$I = \Phi_0 \frac{n - f_{\mathrm{tr}}}{L_{\mathrm{k}} + L_{\mathrm{g}}} \tag{4.4}$$

[cf. Eq. (2.11)] in the trapping loop. From Eq. (4.4) one can determine a maximum number n_{max} of flux quanta that result in a circulating current on the order of the critical current of the loop (order of mA). With the values for the inductances calculated in the previous subsection, we estimate $n_{\mathrm{max}} \gtrsim 50$. Here and for the qubit measurements in Chapter 5, we trap at most 10 flux quanta and, hence, the trapping loop is always well in the superconducting state.

Figure 4.5**a** shows a set of $I_{\mathrm{sw}}(f_{\mathrm{SQ}})$ curves, that are shifted according to the amount of frustration f_{app} applied to the trapping loop during the flux trapping process [2]. From the

[2]Note that the notation f_{app} is used here for the trapping loop frustration f_{tr} in order to clearly denote

flux periodicity of the SQUID and the known areas of SQUID and trapping loop, we can quite accurately predict the necessary amount of f_{app} equivalent to a certain number n of flux quanta [except for the small uncertainty of the factor κ, cf. Eq. (4.2)]. Nevertheless, we also perform flux trapping with intermediate values between the expected ones to check the stepwise flux trapping, that is illustrated in Fig. 4.5**b**. There, the shift δf_{SQ} of the switching current curve is plotted versus f_{app}. For clarity, for a certain number of trapped flux only one data point is shown. The data follows a linear behavior with a slope $\kappa = M_{\mathrm{g}}/L_{\mathrm{k}}/(1+\beta)$. The fact that $\delta f_{\mathrm{SQ}}(f_{\mathrm{app}} = 0) \neq 0$ suggests a constant background field in the cryostat. Thus, we typically do not exactly know the absolute number of trapped flux. Nevertheless, for the biasing of a gradiometric qubit a distinction between odd and even numbers of trapped flux quanta can easily be made by checking the existence of a qubit signal (cf. Sec. 5.2.1). Summing up, our measurements show that we can selectively and reproducibly trap different amounts of flux quanta, which is the basis for the biasing of the gradiometric qubit near its degeneracy point.

4.3 SQUID readout of flux qubits

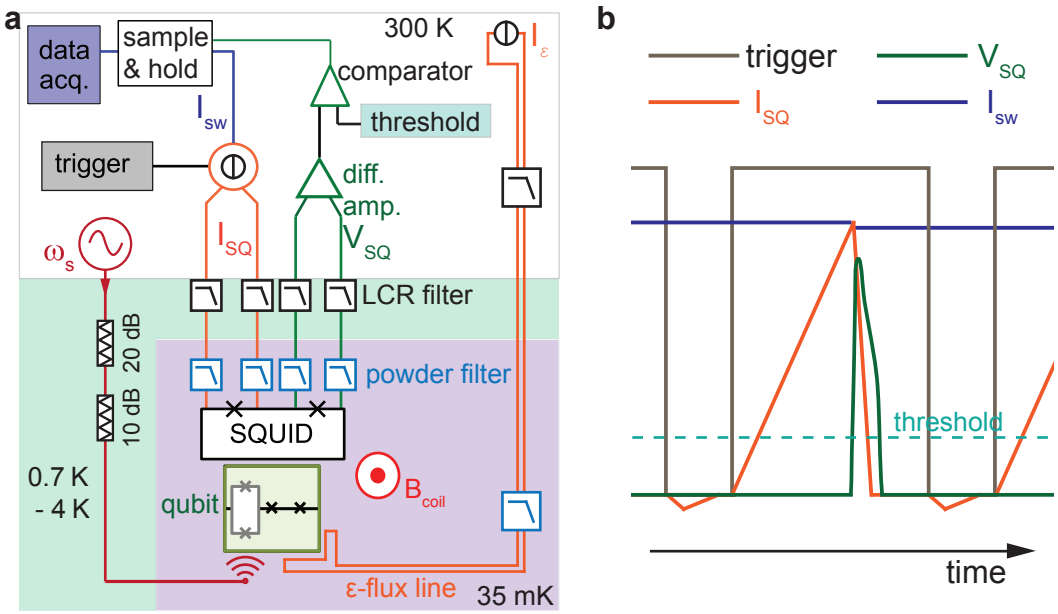

Figure 4.6: **a** Schematic measurement setup with dc-SQUID readout: The qubit is inductively coupled to the readout SQUID. A superconducting coil and/or an on-chip ε-line are used to frustrate SQUID and qubit. The qubit can be excited with a CW microwave signal. **b** Illustration of the SQUID readout protocol: The bias current of the SQUID I_{SQ} is linearly increased until a voltage drop larger than an adjustable threshold is detected.

it as the frustration during the trapping process

In this and the following section, we describe the measurement setups used to characterize flux qubits in this work. The first setup is based on the detection of the magnetic moment generated by the qubit persistent current with a dc-SQUID magnetometer. The second measurement scheme is based on a circuit QED architecture of the qubit coupled to a transmission line resonator (cf. Sec. 4.4). In both cases, the intended sensitivity for quantum mechanical properties still enforces the requirements on experimental conditions as compared to the pre-characterizations in the previous sections. To avoid thermal excitations, e.g., from ground to first excited state of the qubit, the sample temperature T must be low enough to fulfill $k_\mathrm{B}T \ll \hbar\omega_\mathrm{q}$. For typical qubit transition frequencies $\omega_\mathrm{q}/2\pi \simeq 5\,\mathrm{GHz}$ (corresponding to about 240 mK) this is sufficiently achieved by the use of ^{3}He/^{4}He dilution refrigerators with a base temperature of $T \simeq 35\,\mathrm{mK}$ ($T \simeq 15\,\mathrm{mK}$ for the circuit QED setup). It must be noted that the above condition cannot be achieved by increasing the qubit transition frequency as it is bound by a second condition. Only when $\hbar\omega_\mathrm{q} \ll 2\Delta_0$, quasiparticle excitations in the superconducting aluminum are strongly suppressed. With $2\Delta_0 = 360\,\mu\mathrm{eV}$ determined in Sec. 4.1, which equals a frequency of 87 GHz, this condition is well fulfilled for our qubits. Of course, the stable operation of the dilution refrigerator at these temperatures requires a deliberate thermal shielding and anchoring of wires connecting to the sample. Furthermore, the tiny magnetic field ($B \simeq 10^{-8}\,\mathrm{T}$) linked with the qubit persistent current needs to be well protected from magnetic stray fields by the use of mu-metal shields.

The details of the home-made cryostat used for the SQUID-based qubit measurements are explained in Ref. [75] and Ref. [80]. We focus here on the schematic measurement setup as depicted in Fig. 4.6**a**. The SQUID as the readout device for the qubit is located on the sample chip and connected in a four-point geometry. Its feed lines are strongly filtered from high-frequency noise by the use of homemade stainless steel powder filters (cut-off frequency $\simeq 2\,\mathrm{GHz}$) at 35 mK, homemade LCR filters (cut-off 100 kHz) at 4 K and commercial Mini-Circuit BLP (cut-off 1.9 MHz) at room temperature. The flux-dependent switching current of the dc-SQUID is detected as follows: An analog current source provides a current linearly increasing from zero with approximately 0.1 µA/ms (cf. Fig. 4.6**b**). Once this current reaches $I_\mathrm{sw}(\Phi)$ of the SQUID, the corresponding gap voltage is amplified by a differential voltage amplifier (*Stanford Research SR560*) and fed into a voltage comparator. Only when the measured voltage exceeds a well-defined threshold – higher than possible false premature voltage drops – a sample-and-hold circuit is activated that allows to record the current at the moment of the detected switching event. After that, the bias current is decreased again to zero or slightly below in order to ensure the return of the SQUID to the zero-voltage state. The start of the next current ramp is triggered by a square pulse signal of right length to envelope such a measurement cycle. Since the switching of the SQUID into the voltage state is a statistical process, the

cycle is repeated very often (typically 750 times) for each flux value to obtain a Gaussian distribution of the switching events around a mean value $\langle I_{\mathrm{sw}} \rangle$ visible in the histogram of Fig. 4.7**b**. The magnetic flux penetrating the SQUID and qubit loops is applied with a superconducting coil located underneath the sample. In Fig. 4.7**a**, the flux-dependent switching current distribution of a readout SQUID is shown.

The detection of the qubit relies on the change of magnetic flux in the SQUID caused by the flux dependent magnetic moment or persistent current of the qubit (cf. Fig. 3.3**b**). Formally, the total magnetic flux of the SQUID Φ_{SQ} is composed of the applied external flux Φ_{ex} and the flux $\Phi_{\mathrm{q-SQ}}$ induced by the qubit to yield

$$\begin{aligned} \Phi_{\mathrm{SQ}} &= \Phi_{\mathrm{ex}} + \Phi_{\mathrm{q-SQ}} = \\ &= \Phi_{\mathrm{ext}} + k\sqrt{L_{\mathrm{g,SQ}} \cdot L_{\mathrm{g,q}}} \cdot I_{\mathrm{p}} \ . \end{aligned} \tag{4.5}$$

Here, $L_{\mathrm{g,SQ}}$ and $L_{\mathrm{g,q}}$ denote the geometric inductances of SQUID and qubit, respectively, and $0 \leq k \leq 1$ is a parameter for the (inductive) coupling strength between qubit and SQUID. While $k = 0$ means no coupling, the limit $k = 1$ applies to a galvanic coupling over infinite length. It is evident from Eq. (4.5), that the flux in the readout SQUID is affected by changes in the amount and sign of the qubit persistent current I_{p}, which appear near the degeneracy point. Technically, the detection of the qubit via the SQUID's switching current differs for gradiometric and for regular flux qubits. For regular flux qubits, a sweep of the superconducting coil current frustrates both SQUID and qubit simultaneously. Consequently, the qubit signature appears periodically in the $I_{\mathrm{sw}}(\Phi)$ curve of the SQUID, where the exact positions depend on the ratio of the areas of SQUID and qubit. These have to be adjusted (e.g., $A_{\mathrm{SQ}}/A_{\mathrm{q}} = 1.76$) so that the qubit degeneracy points coincide with a large (linear) slope and thus high flux sensitivity in the SQUID's $I_{\mathrm{sw}}(\Phi)$ curve (cf. Sec. 5.1). For gradiometric qubits, that are insensitive to the homogenous field of the coil, an asymmetric on-chip ε-line is used to frustrate the gradiometric qubit. This ε-line (as well as the α-line frustrating the tunable α-loop) is connected in the same way as the SQUID with strongly filtered wires to a current source. Then, the coil is only used to bias the SQUID at a position of high sensitivity and the SQUID is read out while sweeping the ε-line current I_{ε}. In both cases the qubit manifests itself in a continuous steplike feature, that is depicted in Fig. 4.7**c** after subtracting the approximately linear portion of the SQUID. It should be noted that this gradual continuous change of the magnetic signal of the qubit is already a clear signature of the quantum mechanical superposition states. In contrast, the switching of a classical bit would result in an abrupt discrete step. Typically, the qubit step extends over a range of several mΦ_0 of qubit flux.

Although it is in principle possible to extract the qubit gap Δ from the shape of a qubit step measured at different temperatures [91], a more direct and more precise technique

for the qubit characterization is microwave spectroscopy [92, 93]. The spectroscopy tone

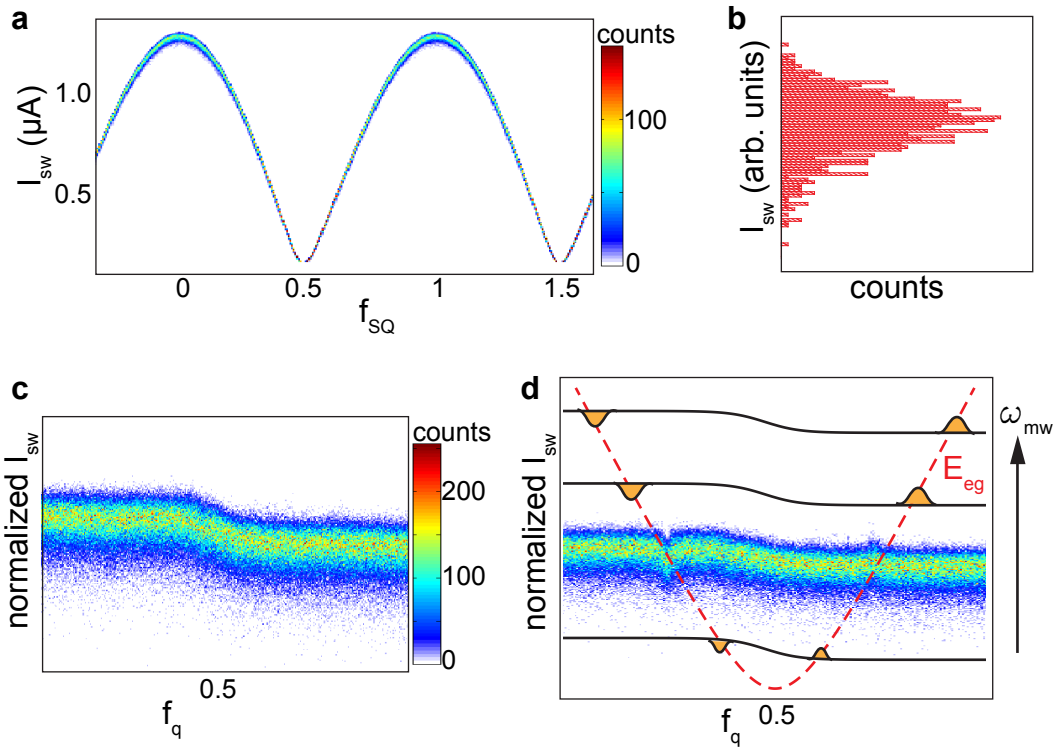

Figure 4.7: **a** Color-coded switching current (I_{sw}) histograms of the readout SQUID as a function of magnetic frustration f_{SQ} applied with the superconducting coil. **b** A single switching current histogram follows a Gaussian distribution with slightly more weight to lower I_{sw} due to thermally or noise-induced premature switching. **c** Normalized switching current (SQUID signal subtracted) revealing the change in magnetic flux due to the continuous switching of the persistent current qubit when changing its frustration f_{q}. **d** Qubit microwave spectroscopy: A CW microwave signal of fixed frequency excites qubit transitions causing a characteristic pair of a dip and a peak around the degeneracy point (see data in color-coded plot). Measuring at various fixed frequencies (schematic black lines) the qubit hyperbola of Eq. (3.8) can be determined.

is a continuous wave microwave signal. It is supplied by a microwave source and fed into the cryostat with an coaxial cable that passes two thermally anchored attenuators for noise reduction. At its end near the qubit sample, the cable is dismantled from its outer conductor in order to act as an antenna. The antenna then irradiates the qubit with a microwave signal of constant frequency ω_{s} and power, while a qubit step is recorded with the SQUID. At those flux values, where the flux dependent qubit transition frequency of Eq. (3.8) matches the spectroscopy frequency, i.e., $\omega_{\mathrm{s}} = \omega_{\mathrm{q}}(\delta\Phi_{\mathrm{q}})$, the qubit is excited from its ground to the excited state, changing the sign of the persistent current. In the qubit step signature detected by the SQUID, this results in characteristic peaks and dips that are located symmetrically with respect to the center of the step, the qubit degeneracy point (cf. Fig. 4.7**d**). Repeating this measurement for several spectroscopy frequencies,

the qubit hyperbola can be mapped out and with a fit of Eq. (3.8) to the measured data the qubit parameters I_p and Δ can be determined.

In summary, this technique is very well suited to investigate the basic properties of fixed-gap as well as of tunable-gap flux qubits as it is shown in Chapter 5. The comparably small dilution unit allows for quick cool-down cycles and two to four samples can be mounted at once. However, it must be stated, that this kind of SQUID readout fails exactly at the interesting degeneracy point of the qubit. Since the circulating currents of opposite direction just cancel each other, in the time average no magnetic signal is measured by the SQUID. Furthermore, any advanced experiments including microwave resonators or time-domain measurements are not possible within this cryostat due to limited space. Therefore, we also use another qubit measurement setup in a larger dilution refrigerator, that is described in the following section.

4.4 Circuit QED readout of flux qubits

Compared to the previous setup, a circuit QED experiment such as in Chapter 6, where extremely low power signals of $\simeq 10^{-17}\,\mathrm{W}$ need to be detected, requires a lot more complexity in terms of shielding and additional bulky components such as circulators and cold amplifiers. In the following, this alternative cryostat and the measurement schemes for the circuit QED experiment are described.

4.4.1 Measurement setup

The homemade ^{3}He/^{4}He-dilution refrigerator used for theses experiments reaches a base temperature of $\simeq 10\,\mathrm{mK}$. It is surrounded by a cryoperm and a mu-metal shielding inside and around the $^4\mathrm{He}/\mathrm{lN}_2$ dewar, and is located inside a shielded room for a strong suppression of electromagnetic noise. Concerning noise the most attention needs to be paid to the input and output lines of the transmission line resonator sample. To avoid a thermal population of the resonator, its input line is interspersed with several attenuators. By thermally anchoring these attenuators to different temperature stages of the cryostat, also the inner conductor of the microwave line is subsequently cooled. This principle is illustrated in Fig. 4.8**a**. The configuration of attenuations is calculated to guarantee a negligible number of thermal photons at the sample temperature. Details of this calculation using Planck distribution can be found in Ref. [94] and Ref. [95]. Like the resonator input line, the line connecting the antenna for qubit excitation is attenuated and thermalized. In contrast, the very weak output signal of the qubit-resonator system must not be attenuated but amplified. Therefore, a cryogenic HEMT amplifier (*LNF*, noise temperature $T_\mathrm{N} \simeq 2\,\mathrm{K}$, gain $\simeq 40\,\mathrm{dB}$ in the frequency range $4 \ldots 8\,\mathrm{GHz}$) is used at

a temperature of 4 K followed by another amplifier at room temperature (*MITEQ JS2*, gain $\simeq 25$ dB). To prevent noise – stemming, e.g., from the amplifiers – from entering via the output line to the sample, cryogenic microwave circulators (*Quinstar*) are used, where the third port is connected with 50 Ω for an absorption of incoming noise. The rf coaxial cables at temperatures below 4 K are also chosen to minimize cables losses and thermal conductivity. The cables have an inner conductor of superconducting niobium (Nb) and an outer conductor of cupronickel (CN). For the input the thinner and more flexible cable type UT47 is used. For the output line the cable UT85 with larger cross-sectional area causes still less loss. Typically, the cables (including SMA connectors) at the sample stage need to be tailored to every new experiment. Consequently, these cables are tested before the experiment in a TDR (time domain reflectometry) measurement to ensure impedance mismatches of less than 5 Ω. Also the complete input and output lines are tested for transmission losses. The sample itself is located inside a gold-plated copper box, that can be seen either closed or open in Fig. 4.8**b** and Fig. 4.8**c**. The 10x6 mm^2 large sample chip is fixed inside the box with silver glue, that also provides good electrical and thermal contact between the resonator ground plane and the sample box as well as between the resonator inner line and the pin of the SMA connector (cf. Fig. 4.8**c**).

In order to connect the on-chip ε-flux bias line of a gradiometric qubit or any other on-chip structure (SQUIDs) with dc lines, bond wires can be set between the chip and a PCB with copper pads next to the chip inside the sample box. Copper wires soldered onto these copper pads exit the sample box via small holes. The lines are then connected to stainless-steel-powder filters, that are excellent low-pass filters for frequencies below the GHz-regime [10, 96–101]. The dc lines continue up to 1K in form of superconducting niobium-titanium (NbTi) wires in bronze or cupro-nickel matrix, that largely suppress thermal conductivity. Manganin wires build up the dc lines from 1K to room temperature, where they are passing additional low-pass filters (Mini-Circuits BLP-1.9 and home-made RC low-pass filters) and connect to an analog current source. The latter is controlled by the measurement program via a National Instruments PCI-6052E 16-bit acquisition card. The same card and current source is used to generate a homogenous magnetic field at the sample with a superconducting magnet coil. The coil consists of approximately 4400 windings of a NbTi wire in copper matrix [102] and is located just next to the sample box (cf. Fig. 4.8**b**). The magnet is equipped with a persistent current switch allowing to trap flux in the magnet coil for a stable constant magnetic field bias. However, for the measurements presented here the coil is used in the non-persistent mode only.

To ensure the stable operation of the refrigerator and the success of the careful thermalization several thermometers are placed at different temperature stages of the cryostat, which are read out with an AVS-47 resistance bridge. Especially, one thermometer is placed right on top of the sample box (gray block in Fig. 4.8**b**).

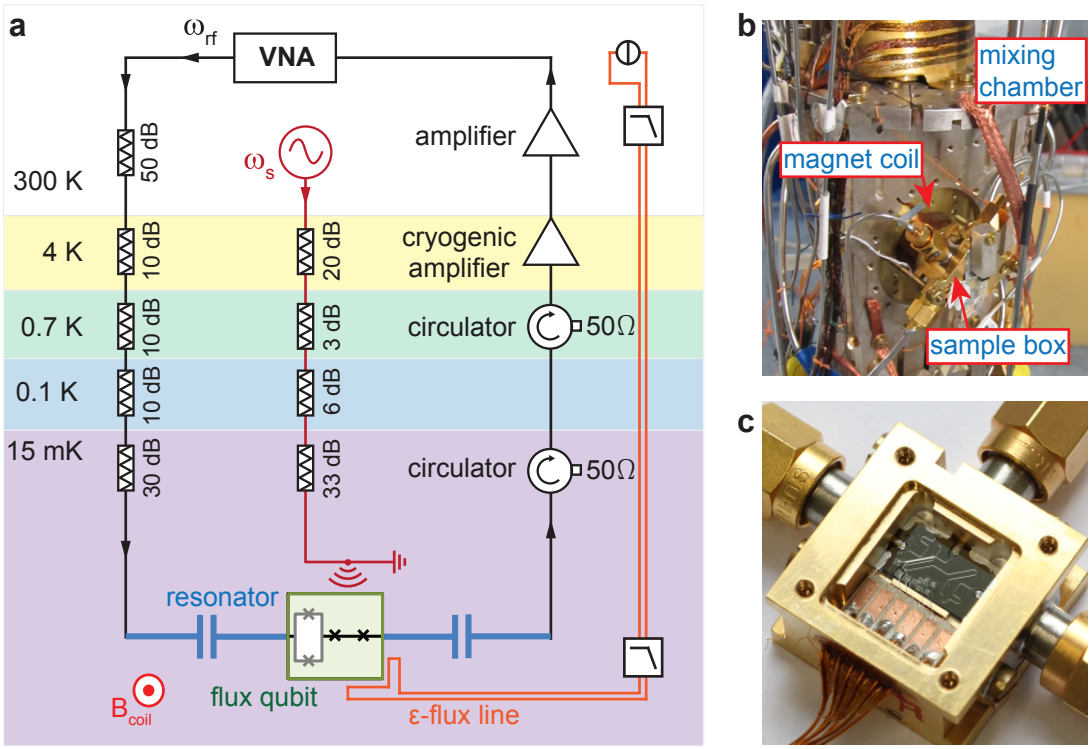

Figure 4.8: **a** Schematic setup for circuit QED measurements of coupled qubit-resonator systems. The input signal ω_{rf} generated by a VNA is heavily attenuated at different temperature stages (background colors) in order to suppress thermal noise and to reach the single-photon level inside the resonator. This applies similarly to the qubit excitation signal ω_{s} that stems from a microwave source and is fed to an antenna near the qubit. The resonator output line contains two circulators for noise reduction and two amplifiers. Twisted pair dc wires for the ε-line are filtered several times. Not shown are the feed lines of the superconducting coil generating the homogenous magnetic field B_{coil}. **b, c** Photographs of the mounted and open sample box.

4.4.2 Measurement protocols

In order to spectroscopically analyse the coupled cavity-qubit system as a function of an applied magnetic flux, basically two measurement protocols are used: a cavity power transmission measurement and a so-called two-tone spectroscopy.

Cavity transmission spectroscopy

In this measurement scheme the transmitted power through the resonator is probed for each flux value. This is realized by the use of a *Rohde & Schwarz (R&S) ZVA24* vector network analyzer (VNA), that measures the transmitted power (and also phase) of a frequency sweep of fixed power sent to the sample (cf. Fig. 4.8). As described above, the input line from the VNA to the sample is heavily attenuated by approximately $-150\,\mathrm{dB}$ (including additional $-10\,\mathrm{dB}$ of estimated cable losses). Together with typical VNA output powers of $-10\,\mathrm{dBm}$ in the experiments of Chapter 6, this result in a power of only $10^{-19}\,\mathrm{W}$. We verify in Sec. 6.2.3, that this corresponds to the regime of less than one photon on average in the resonator sample. Consequently, one can assume that no photon is transferred from resonator to qubit during this measurement. And even if the qubit is excited, its expected lifetime is short compared to the timescale of the transmission measurement. Therefore, the qubit resides in its ground state and the transmission measurement probes the lowest energy eigenstate of the coupled qubit-resonator system with the resonant and dispersive interactions described in Sec. 3.4. Especially, with this measurement the coupling strengths between qubit and resonator modes are determined in Sec. 6.3.

Two-tone spectroscopy

Two-tone spectroscopy is based on the dispersive interaction between qubit and resonator and the dependence of the dispersive shift on the qubit state as described in Sec. 3.4. In contrast to the cavity transmission measurement, the qubit is to be excited in two-tone spectroscopy while the resonator is still probed as before. This is achieved by sending another continuous wave signal, stemming from an *R&S SMF* microwave source, to the qubit via the antenna line (cf. Fig. 4.8). Similar to the resonator input line, the antenna line experiences a strong attenuation of approximately $-72\,\mathrm{dB}$ (including cable losses). With a typical output power of $-20\,\mathrm{dBm}$ at the SMF, a power of around $10^{-12}\,\mathrm{W}$ reaches the antenna of the sample. This power is significantly larger than the one of the resonator probe signal because of two reasons. First, this signal tone is in general not resonant with the transmission line resonator and thus, does not experience a resonant enhancement of field strength. In fact, only an unknown part of the microwave power is transferred from the antenna to the qubit. Second, the qubit excitation needs to be

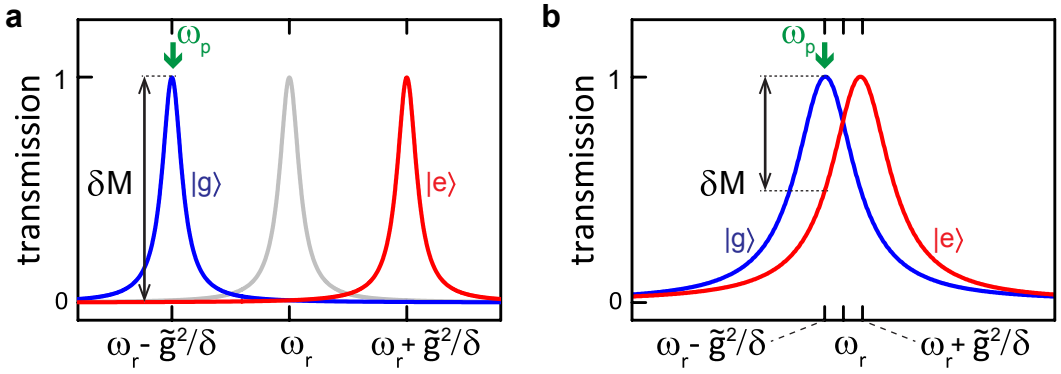

Figure 4.9: **a** Schematic illustration of the two-tone measurement. Shown are the Lorentzian transmission curves of an uncoupled resonator (gray), a resonator with dispersive shift due to the interaction with a qubit in its ground state (blue) and the same for the qubit in the excited state (red). When the qubit is excited, the change in magnitude δM at the probe frequency ω_p determines the measurement contrast. **b** For reduced dispersive shift the measurement contrast decreases significantly.

strong enough to continuously excite the qubit despite its decay. As a consequence, the qubit is in saturation with equal probabilities to be in its ground or excited state. The measurement principle is further illustrated in Fig. 4.9: For a fixed magnetic flux bias, at first a cavity transmission spectrum is recorded in order to determine the effective resonant frequency $\omega_\mathrm{r} - \frac{g^2 \sin^2\theta}{\delta}$ of the resonator with dispersive shift of a qubit in its ground state (again in low photon number approximation, cf. Sec. 3.4). Then, the resonator probe frequency ω_p is fixed at this value and transmission is continuously probed by the ZVA. Simultaneously, the signal frequency ω_s is varied step by step. When ω_s matches the flux dependent qubit transition frequency, the qubit is excited. In the probe signal of the ZVA, this manifests in a decrease of the transmitted power. Due to the 50% population of ground and excited state, the decrease in transmission equals $\frac{1}{2}\delta M$ with δM as defined by Fig. 4.9. By repeating this procedure for a range of magnetic frustration around the degeneracy point, the flux dependent qubit transition frequency can be mapped out and the essential qubit parameters persistent current I_p and, most importantly, the qubit gap Δ can be evaluated. However, the quality of the two-tone measurement varies with magnetic flux bias. As can be seen from Fig. 4.9**b**, the detected change in magnitude $\frac{1}{2}\delta M$ decreases significantly when the dispersive shift is only of the size of the transmission linewidth. Away from the degeneracy point the effective coupling rate $\tilde{g} = g \sin\theta$ with $\theta = \arctan(\Delta/\varepsilon)$ decreases. Also, for very large detuning $\delta = \omega_\mathrm{q} - \omega_\mathrm{r}$ the signal is reduced. Furthermore, by increasing the resonator probe power, the dispersive shift also contains a photon number dependent contribution. This allows us to calibrate the photon number inside the resonator from a two-tone experiment in Sec. 6.2.3.

Chapter 5

Making the flux qubit tunable: A spectroscopic study

One main goal of this thesis is to successfully operate a gradiometric tunable-gap flux qubit at the WMI. Due to the much more complex design of this qubit as compared to a standard 3-JJ qubit, considerable effort is spent on a systematic implementation. This includes the careful pre-characterization described in the previous chapter, especially the determination of JJ parameters by SQUID measurements in Sec. 4.1.2 and the study of phase biasing and flux trapping in Sec. 4.2. Moreover, we perform a stepwise transition from the standard 3-JJ qubit to the gradiometric tunable-gap qubit, which is reflected in the arrangement of this chapter.

We first start with the characterization of two standard fixed-gap qubits in Sec. 5.1. With these results we can confirm a successful qubit fabrication process and the functionality of our measurement technique. The determined qubit parameters form a reference for the following samples. In Sec. 5.2, a gradiometric – but still 3-JJ fixed-gap – qubit is investigated. Here, the trapping of magnetic flux for phase-biasing and the use of the on-chip ε-line can be explored without too much increase of complexity coming along with a tunable α-SQUID. The latter is finally realized in a gradiometric tunable-gap qubit in Sec. 5.3. In particular, we test the tunability range of the qubit gap. The second of the two samples we show is optimized by fabrication for a larger tunability of the qubit gap.

All the measurements in this chapter are performed inside a small homemade dilution refrigerator with the dc-SQUID readout as introduced in Sec. 4.3. We use continuous wave spectroscopy to determine the qubit parameters Δ and I_p. This chapter closely follows the author's work from Ref. [63].

5.1 Regular fixed-gap flux qubits

We first discuss the properties of fixed-gap, non-gradiometric flux qubits serving as reference samples. The qubit gap Δ and the persistent current I_p are determined by qubit

spectroscopy as discussed in Sec. 4.3. The main sample layout is depicted in the SEM micrograph of Fig. 5.1**a**. The qubit is tightly surrounded by the readout SQUID, guaranteeing large mutual inductance between the two elements. For this non-gradiometric layout, qubit and SQUID are frustrated simultaneously by the homogeneous magnetic field of the external coil. The flux periodicity of qubit and SQUID is, however, different and depends on the area ratio $A_{\mathrm{SQ}}/A_{\mathrm{q}} = 1.76$, which is illustrated in Fig. 5.1**b**. It shows the maximum switching current I_{sw} of the readout SQUID with its flux dependence according to Eq. (2.28). Possible qubit steps appear at the qubit degeneracy points marked with the rectangles. The following measurements are performed at $f_{\mathrm{q}} = -1.5$ (red rectangle), where a large linear slope of $I_{\mathrm{sw}}(f_{\mathrm{SQ}})$ provides good readout contrast. Figure 5.1**c** shows one typical qubit spectrum, where the qubit frustration $\delta f_{\mathrm{q}} = f_{\mathrm{q}} - (n + \frac{1}{2}) = \delta\Phi_{\mathrm{q}}/\Phi_0$ is swept at fixed microwave frequency $\omega_{\mathrm{s}}/2\pi = 24.93\,\mathrm{GHz}$. The clearly visible qubit step is obtained after subtracting the flux dependence of the readout SQUID from the mean value of the switching current histograms. Only at those δf_{q} values where the microwave driving is resonant with the qubit transition frequency ω_{q}, a 50% population of the excited state occurs. This manifests itself in characteristic peak and dip structures in the switching current I_{sw} of the readout SQUID at frequency dependent δf_{q} values. At $\delta f_{\mathrm{q}} \simeq \pm\, 0.013$ a dip and a peak, respectively, are visible due to the microwave excitation. By Lorentzian fits (see the red curve at the dip) to these dips and peaks, we determine their position in δf_{q}.

For a full qubit spectroscopy these resonance positions are recorded for various excitation frequencies ω_{s} and we thus obtain $\omega_{\mathrm{q}}(\delta f_{\mathrm{q}})$. Figure 5.2 shows typical spectra obtained for two 3-JJ flux qubits with fixed α-junction. Assuming that j_{c} has the same value for all three junctions, the value of $\alpha = \alpha_0 = A_\alpha/A_{\mathrm{J}}$ can be determined from the measured area ratio. Then a two-parameter fit of Eq. (3.8) to the spectroscopy data yields Δ and $I_{\mathrm{p}} = \hbar\varepsilon/2\delta\Phi_{\mathrm{q}}$. The spectra in Fig. 5.2 are obtained for two flux qubits differing only in their α_0 values. For $\alpha_0 = 0.75$ and 0.55, we obtain $\Delta/2\pi = 1.39\,\mathrm{GHz}$ and $10.76\,\mathrm{GHz}$ and $I_{\mathrm{p}} = 583\,\mathrm{nA}$ and $283\,\mathrm{nA}$, respectively. Obviously, for α_0 values closer to 0.5 (1.0) large (small) Δ and small (large) I_{p} values are obtained in agreement with Eq. (3.9) and (3.4). A consistency check can be made by calculating the I_{p} values from Eq. (3.4). Here, the unknown critical current $I_{\mathrm{c}} = j_{\mathrm{c}}A$ is estimated from the measured junction area and using the j_{c} value of the junctions of the readout SQUID. We obtain $I_{\mathrm{p}} = 619\,\mathrm{nA}$ and $270\,\mathrm{nA}$ in good agreement with the values derived from the spectroscopy data.

We also perform numerical simulations based on the diagonalization of the full qubit Hamiltonian using E_{J}, E_{c} and $\alpha = A_\alpha/A_{\mathrm{J}}$ as input parameters. They are based on the values for j_{c} and c_{s} derived from the IV characteristic of the readout SQUID (cf. Sec. 4.1.2) and the measured junction areas. As shown in Fig. 5.2, there is very good agreement between the simulation result and the two-parameter fit for $\alpha = 0.55$. However, signifi-

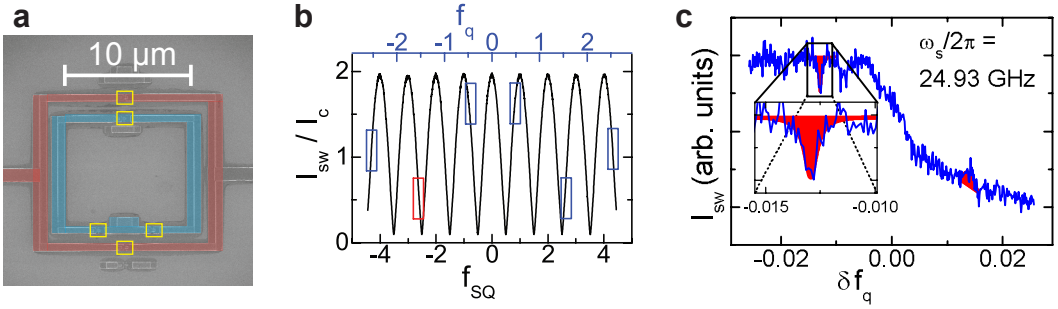

Figure 5.1: **a** SEM micrograph of a standard fixed-gap qubit (highlighted with blue color) enclosed by the readout SQUID (red). Positions of the JJs are marked by yellow rectangles. **b** Flux periodicity of readout SQUID (bottom axis) and qubit (top axis). Shown is the SQUID switching current. The rectangles mark the possible positions of qubit steps (degeneracy points) consistent with the area ratio $A_{\mathrm{SQ}}/A_{\mathrm{q}} = 1.76$. Qubit spectroscopy is performed at $f_{\mathrm{q}} = -1.5$ (red rectangle). **c** Exemplary qubit spectrum at a driving frequency $\omega_{\mathrm{s}}/2\pi = 24.93\,\mathrm{GHz}$. The mean value of the SQUID switching current clearly shows a qubit step and the characteristic peak and dip. By Lorentzian fits (red curves) the dip and peak positions in δf_{q} are extracted.

cant deviations appear for $\alpha = 0.75$. The reason is that there are not enough data points around $\delta\Phi_{\mathrm{q}} = 0$, where the readout of the qubit state by the dc-SQUID fails. This leads to large uncertainties in Δ for the two-parameter fit. Therefore, small Δ values tend to have larger error bars. Nevertheless, Fig. 5.2 clearly demonstrates that the numerical simulation describes the experimental data very well.

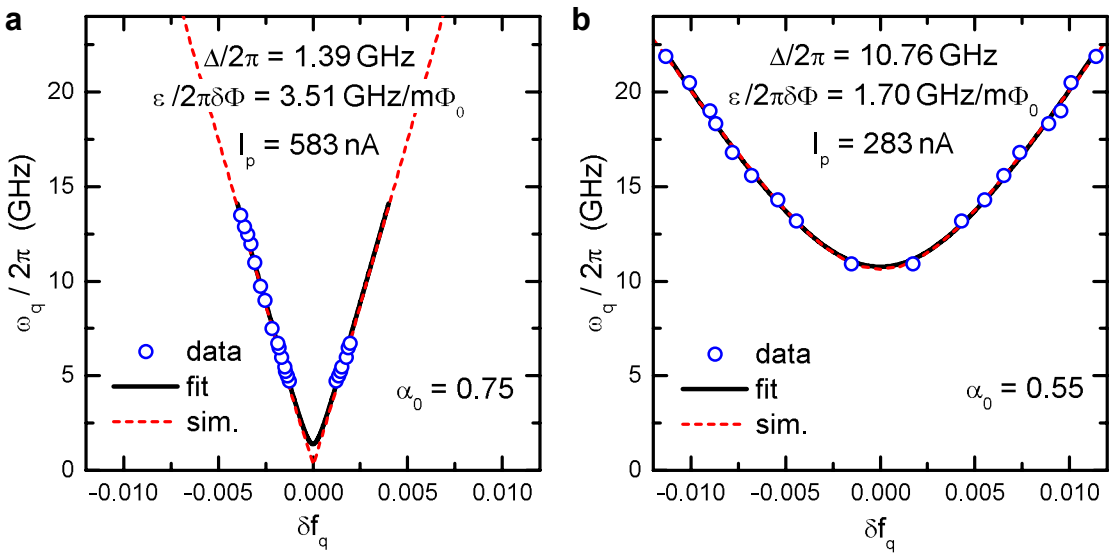

Figure 5.2: Transition frequency $\omega_{\mathrm{q}}/2\pi$ plotted versus $\delta f_{\mathrm{q}} = f_{\mathrm{q}} - (n + \frac{1}{2}) = \delta\Phi_{\mathrm{q}}/\Phi_0$ for two fixed-gap flux qubits with **a** $\alpha_0 = 0.75$ and **b** $\alpha_0 = 0.55$. Also shown is a two-parameter fit of the data (black lines) yielding $\Delta/2\pi$ and I_{p} and the result of a numerical simulation based on the diagonalization of the full qubit Hamiltonian. In **b**, the result of the two-parameter fit and the simulation are almost indistinguishable.

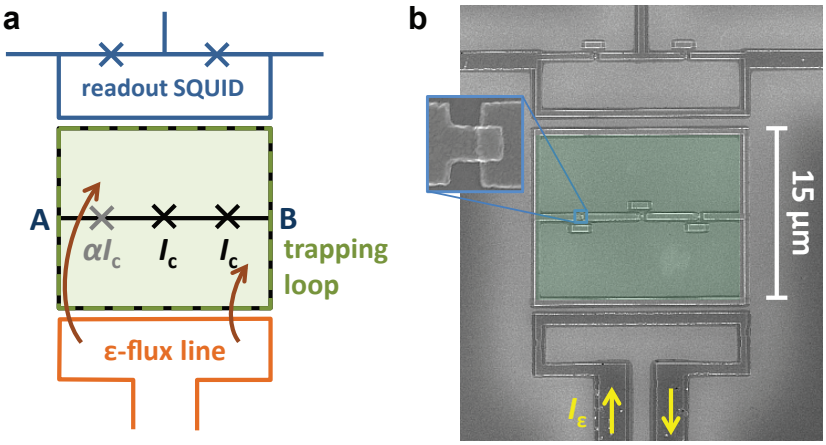

Figure 5.3: **a** Circuit schematics of the fixed-gap gradiometric flux qubit with readout dc-SQUID and ε-flux line. The outer loop of the flux qubit (broken olive line) forms the trapping loop. **b** SEM image of the implemented circuit. The inset shows an enlarged view of the α-junction.

In summary, the characterization of these two standard fixed-gap flux qubits demonstrates the successful operation of the fabrication process ensuring a good starting point for the fabrication of new qubit layouts. Furthermore, the above analysis proves that our evaluation routine and the use of input parameters for E_J and E_c is suitable. Besides, these data also emphasise one main motivation for a tunable-gap flux qubit: Although the large difference in qubit gap for the two samples is in agreement with different values for α_0, limitations in the fabrication process hardly allow us to realize a qubit gap with an accuracy of less than some hundred megahertz.

5.2 The fixed-gap gradiometric flux qubit

We next discuss the properties of fixed-gap gradiometric flux qubits to demonstrate the operation of the gradiometric qubit design shown in Fig. 5.3**a** and Fig. 5.3**b**. Besides the qubit's eight-shaped gradiometric design, there are two differences to the standard qubits studied in the previous section. First, the qubit frustration is now changed by sending a current I_ε through the on-chip ε-flux bias line. The external coil is still used to frustrate the SQUID but should not affect the gradiometric qubit (cf. Sec. 5.2.3). Second, the presence of the ε-line requires us to place the qubit next to instead of inside the readout SQUID. From geometric considerations, we expect the mutual coupling between qubit and SQUID to decrease by a factor of approximately two, which forces us to increase the number of switching events per flux point by a factor four to achieve a similar readout quality. Typically, we use a number of 750 switching events for each flux value for the measurements on gradiometric qubits in this chapter.

5.2.1 Qubit bias by flux trapping

We start the characterization of the gradiometric qubit with a demonstration of the qubit-biasing by flux trapping. In Sec. 4.2, we explore the technique of flux trapping and the phase-biasing of SQUIDs. Here, we show the effect of flux trapping on the gradiometric fixed-gap qubit. Therefore, we trap different numbers of flux quanta in the qubit trapping loop (cf. Fig. 5.3**a**) and then sweep the current through the ε-line to change the qubit frustration while reading out the dc-SQUID continuously.

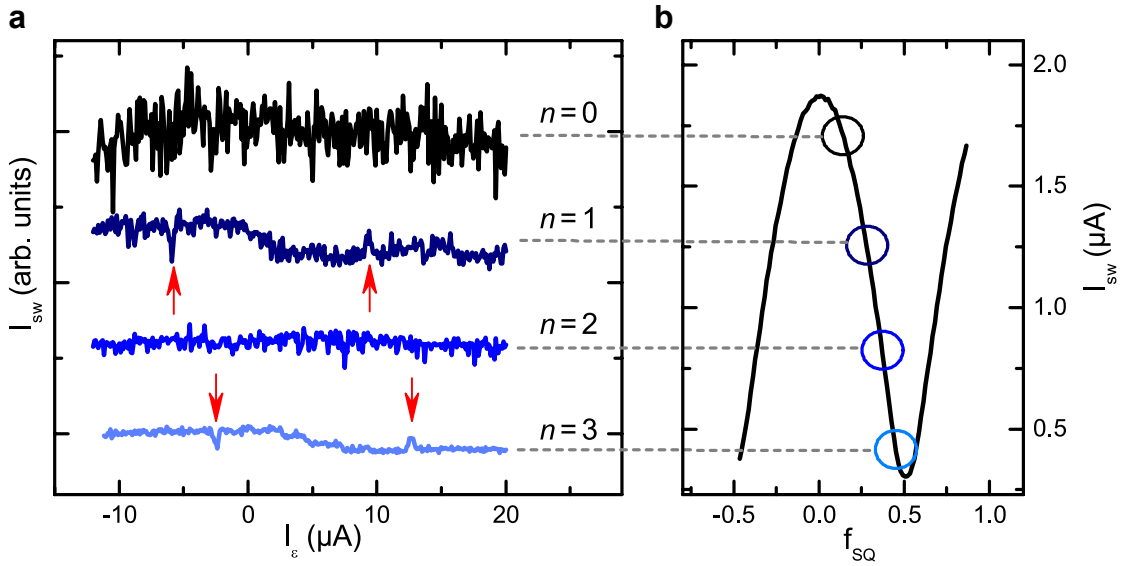

Figure 5.4: **a** Mean switching current versus ε-line current I_ε for an increasing number n of trapped flux quanta in the outer qubit loop. Only for an odd number of trapped flux ($n=1,3$), a qubit step and dips and peaks (marked with red arrows) due to qubit excitation with $\omega_s/2\pi = 8.13\,\mathrm{GHz}$ are visible. **b** Illustration of the working points of the readout SQUID corresponding to the spectra in **a**, explaining the different signal amplitudes and quality.

In Fig. 5.4**a**, the mean switching current is plotted versus the current I_ε for $n=0\ldots3$ trapped flux quanta. For $n=1$ and $n=3$, these curves clearly show a qubit step near $I_\varepsilon=0$ and the characteristic dips and peaks (marked with red arrows) due to the excitation with a continuous microwave signal of frequency $\omega_s/2\pi = 8.13\,\mathrm{GHz}$. In contrast, the data for $n=0$ and $n=2$ do not reveal any indication of the qubit. These experimental results are in full agreement with the expected behavior of flux biasing as described theoretically in Sec. 3.3.1. The flux qubit is biased close to its symmetry point by freezing in an odd number $n=(2n'+1)$ ($n'\in\mathbb{N}$) of flux quanta in the trapping loop during cool-down. This results in a phase difference of $(2n'+1)\pi$ between points A and B, equivalent to a flux bias of $(n'+\frac{1}{2})\Phi_0$ of the gradiometric flux qubit at its symmetry point. Freezing in an even number $n=2n'$ of flux quanta, however, results in a phase difference between points A and B of $2\pi n'$. This corresponds to a flux bias of the gradiometric qubit by

$2n'\Phi_0/2 = n'\Phi_0$. That is, the qubit is biased far away from its symmetry point and no qubit transitions should be observable near $I_\varepsilon = 0$. A large current I_ε would be necessary to reach the degeneracy point in this situation. Technically, we could not provide such a large current as heating in contact resistances in the feed lines would suppress superconductivity in the sample first (see the discussion on heating effects in Ref. [76]).

It should also be mentioned that the four spectra in Fig. 5.4**a** differ in signal amplitude and signal-to-noise ratio (SNR) as a consequence of different readout working points of the dc-SQUID. This is illustrated in Fig. 5.4**b**, showing that, with increasing number n of trapped fluxoids, the SQUID working point is shifted from the maximum to the minimum of the $I_{\rm sw}(f_{\rm SQ})$ curve. This is consistent with an increasing circulating current in the trapping loop and, following Eq. (4.5), an additional flux induced in the SQUID. Consequently, the absolute value of the switching current decreases, but the detected qubit signal, i.e., the SNR, increases with n for the data shown here. For example, the SNR increases from a value of approximately 2 for $n = 1$ to a value of 8 for $n = 3$. However, the dependence of the SQUID working point on the number of trapped flux quanta is shown here rather to demonstrate this principle. In fact, the gradiometric qubit design is advantageous in a sense that the external coil can be used to properly adjust the readout point of the SQUID without affecting the qubit flux bias. This statement is, however, only true for a perfectly working gradiometer. The fact that the position of the qubit step changes from $n = 1$ to $n = 3$ is an indication for a finite imbalance of the gradiometer, which is analyzed in Sec. 5.2.3 after characterizing the qubit properties.

5.2.2 Spectroscopy of gradiometric fixed-gap qubits

Having biased the qubit close to the degeneracy point and the SQUID to an adequate readout position as just described above, we perform continuous microwave spectroscopy on two gradiometric fixed-gap qubits. The measurement technique is the one described in Sec. 4.3 and the same as in the previous section on standard flux qubits with one main difference. Now, the frustration of the gradiometric qubit is swept by the spatially inhomogeneous magnetic field, which is generated by the current I_ε sent through the ε-flux line. Two examples of single spectra with qubit excitation of frequency $\omega_{\rm s}/2\pi = 8.13\,{\rm GHz}$ are already shown in Fig. 5.4**a**.

Figure 5.5**a** and Fig. 5.5**b** show the whole set of spectroscopy data of two gradiometric fixed-gap flux qubits, that differ by fabrication in the value of $\alpha_0 = 0.77$ and $\alpha_0 = 0.65$, respectively. The qubit transition frequency $\omega_{\rm q}/2\pi$ is plotted versus the gradiometric qubit frustration $\delta f_{\rm q} \equiv \delta f_{12} = f_{12} - (n + \frac{1}{2}) = \delta\Phi_{\rm q}/\Phi_0$.

Since we are measuring $\omega_{\rm q}(\delta I_\varepsilon)$ and not $\omega_{\rm q}(\delta f_{\rm q})$ in the first place, the evaluation of

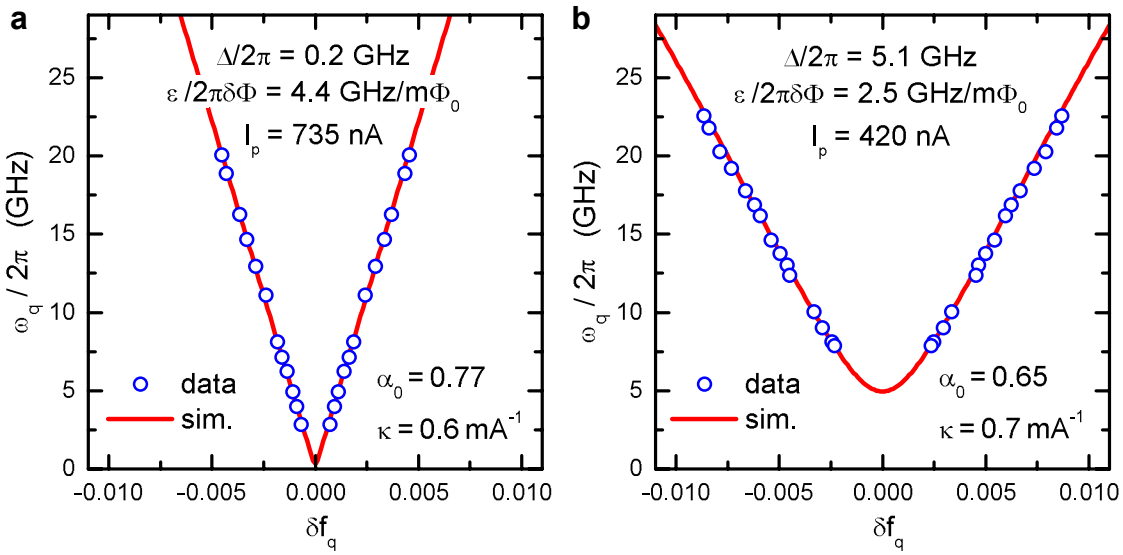

Figure 5.5: Spectroscopy data for two gradiometric fixed-gap qubits with **a** $\alpha_0 = 0.77$ and **b** $\alpha_0 = 0.65$, respectively. The transition frequency $\omega_q/2\pi$ is plotted versus $\delta f_q = f_q - (n + \frac{1}{2}) = \delta\Phi_q/\Phi_0$. Also shown is the result of a numerical simulation (red line) based on the diagonalization of the full qubit Hamiltonian with the listed parameters.

this data contains a calibration factor

$$\kappa \equiv \frac{\partial \delta f_q}{\partial \delta I_\varepsilon} , \tag{5.1}$$

where $\delta I_\varepsilon = I_\varepsilon - I_\varepsilon^{sym}$ is the deviation of the current I_ε sent through the ε-flux line from the value I_ε^{sym} needed for biasing the qubit at the symmetry point. This is done by calculating $\omega_q(\delta f_q)$ by numerical simulations using the pre-characterized values E_J, E_c and $\alpha = A_\alpha/A_J$ as input parameters – a procedure that is proven to yield trustworthy results in the previous section on standard fixed-gap qubits. The scaling factor κ is then obtained by re-scaling the measured $\omega_q(\delta I_\varepsilon)$ dependence to obtain optimum agreement with the simulation result. For the samples in Fig. 5.5, we obtain $\kappa = 0.6\,\mathrm{mA}^{-1}$ and $\kappa = 0.7\,\mathrm{mA}^{-1}$, respectively, saying that a current of about 1 mA results in $\delta f_q = 1$. In general, the agreement between the experimental data and the simulation is found to be very good. The simulated values for the samples in Fig. 5.5 are $\Delta/2\pi = 0.2\,\mathrm{GHz}$ and $I_p = 735\,\mathrm{nA}$ for $\alpha_0 = 0.77$ in Fig. 5.5**a** and $\Delta/2\pi = 5.1\,\mathrm{GHz}$ and $I_p = 420\,\mathrm{nA}$ for $\alpha_0 = 0.65$ in Fig. 5.5**b**. Again, we can make a consistency check by calculating the I_p value according to Eq. (3.4) as discussed above. We obtain $I_p = 768\,\mathrm{nA}$ (**a**) and $I_p = 485\,\mathrm{nA}$ (**b**) in good agreement with the values derived from the simulation.

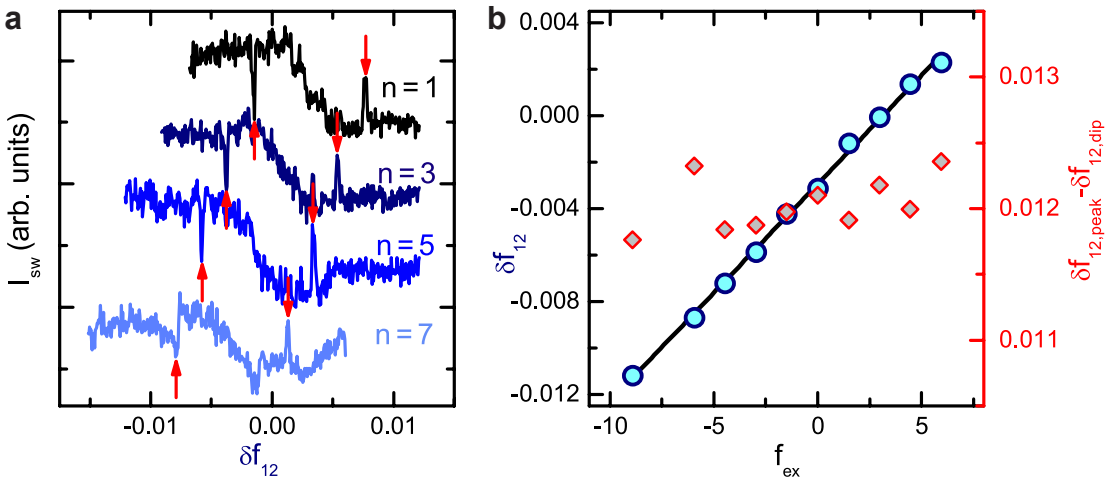

Figure 5.6: **a** Switching current I_{sw} of the readout SQUID of a fixed-gap gradiometric flux qubit as a function of $\delta f_{12} = f_{12} - \left(n + \frac{1}{2}\right)$ recorded for a fixed microwave frequency of 19.33 GHz. The peak and dip positions mark those δf_{12} values where $\omega_{\mathrm{q}}/2\pi = 19.33\,\mathrm{GHz}$. **b** Frustration imbalance δf_{12} as a function of the frustration f_{ex} generated by a homogeneous applied magnetic field. Also shown is the distance between the peak and dip positions in the $I_{\mathrm{sw}}(\delta f_{12})$ curves.

5.2.3 Gradiometer quality

We also use the simple fixed-gap gradiometric qubit to check the quality of the gradiometer discussed in Sec. 3.3.3. Figure 5.6**a** shows the switching current of the readout SQUID as a function of $\delta f_{12} = f_{12} - \left(n + \frac{1}{2}\right)$ recorded for a fixed microwave frequency of 19.33 GHz. The peaks and dips in the $I_{\mathrm{sw}}(\delta f_{12})$ curves mark the δf_{12} positions where the qubit transition frequency $\omega_{\mathrm{q}}/2\pi = 19.33\,\mathrm{GHz}$. On varying the number n of trapped flux quanta, these positions shift due to the imperfect balance of the gradiometer. From the measured shift we derive $Q_{\mathrm{grad,n}} = 943 \pm 19$. In Fig. 5.6**b**, δf_{12} is plotted versus f_{ex} generated by a homogeneous applied magnetic field. From the measured slope the quality factor $Q_{\mathrm{grad,ex}} = 1076 \pm 16$ is determined. The total quality of the gradiometer is then $Q \simeq 500$, corresponding to a gradiometer imbalance of only 0.2%. This means, that the qubit operation point is shifted by about $2\,\mathrm{m}\Phi_0$ when we apply a homogeneous field generating one Φ_0 in the trapping loop. The measured quality factors are plausible. For example, the limited precision of the electron beam lithography process causes a finite precision $\delta A/A_{\mathrm{tr}}$ of the trapping loop area as well as $\delta S/S$ of the cross-sectional area and $\delta\ell/\ell$ of the length of the superconducting lines. The measured quality factor corresponds to $\delta A \simeq 0.2\,\mu\mathrm{m}^2$, $\delta S \simeq 50\,\mathrm{nm}^2$ or $\delta\ell \simeq 60\,\mathrm{nm}$. These values agree well with the values expected for the precision of the fabrication process.

In Fig. 5.6**b**, we also plot the distance between the peak and dip positions in the $I_{\mathrm{sw}}(\delta f_{12})$ curves. This distance is nearly independent of f_{ex}, demonstrating that the qubit potential is not affected by the homogeneous background field.

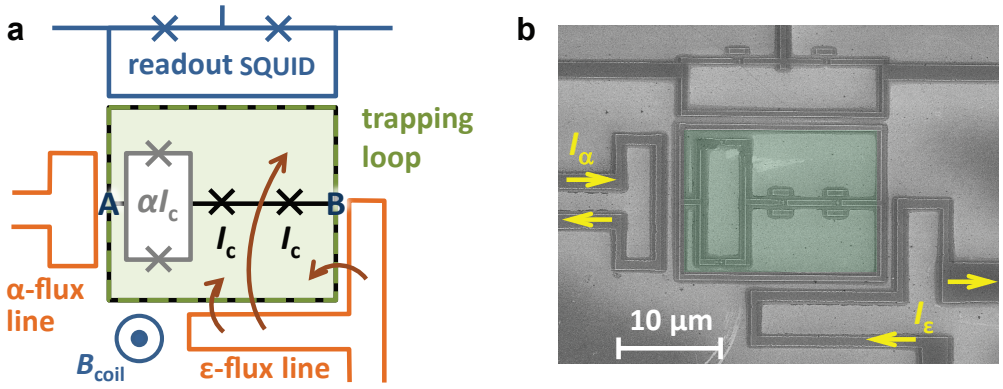

Figure 5.7: **a** Circuit schematics of the tunable-gap gradiometric flux qubit with readout dc-SQUID, ε- and α-flux line. The outer loop of the flux qubit (broken olive line) forms the trapping loop, the inner (gray line) the α-loop. **b** SEM image of the implemented circuit.

In total, our results show that the gradiometric flux qubits can be fabricated in a controlled way and work as expected. The fact that the qubit operation point is not affected by a homogeneous background field allows us to integrate these qubits into large scale circuits where several qubits have to be operated and read out simultaneously without affecting each other.

5.3 The tunable-gap gradiometric flux qubit

In this subsection, we discuss the results obtained with tunable-gap gradiometric flux qubits as sketched in Fig. 5.7. This layout now combines the gradiometer principle investigated in the previous section with a tunable α-SQUID. In addition to the ε-line for frustrating the qubit, we integrate the additional on-chip α-line that is arranged symmetrically with respect to the gradiometer. Consequently, a dc current I_α through this α-line does not affect the qubit frustration f_q but only changes the frustration of the α-loop and thus the qubit gap Δ. Possible crosstalk between α-line and the qubit loop as well as between ε-line and α-loop is found to be negligible in the current ranges used for the following experiments. Tuning the qubit gap Δ via the on-chip α-line is demonstrated in Sec. 5.3.4. Before, we change the value of α with the homogenous magnetic field generated by the current I_coil fed through an external superconducting coil in Sec. 5.3.1. Besides this continuous variation of α by an applied magnetic field (external or on-chip), α can be changed step-wise by freezing different numbers of (odd) flux quanta in the trapping loop. The analysis of this dependence can be used to directly determine the inductance ratio β of Eq. (3.14) in Sec. 5.3.2. Moreover, we test the quality of the gradiometer in Sec. 5.3.3. For the following, the spectroscopy measurement technique is

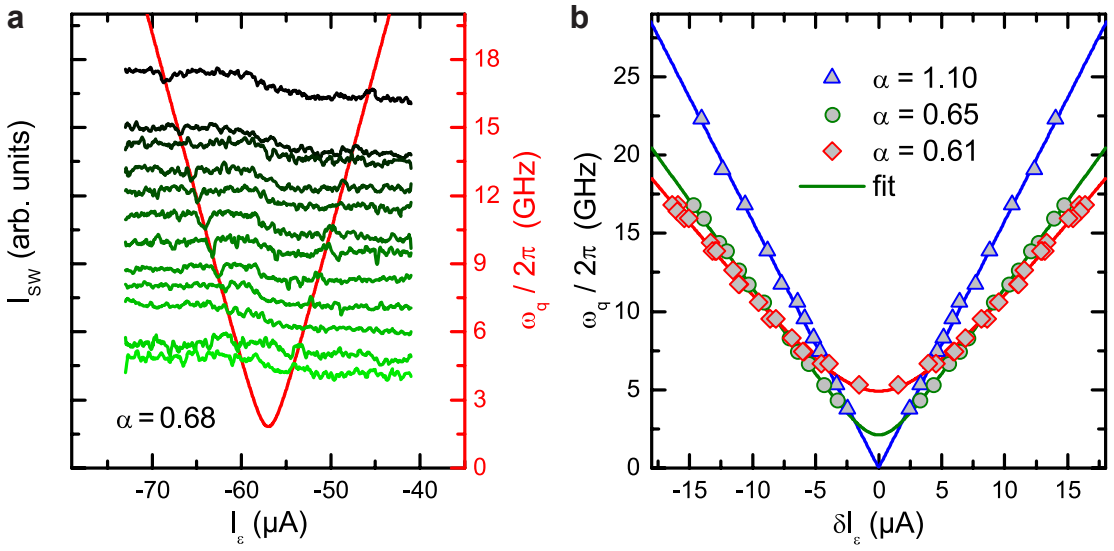

Figure 5.8: **a** Exemplary set of recorded qubit spectra obtained by sweeping the ε-current I_ε for a constant value of $\alpha = 0.68$. The spectra for different excitation frequencies are shifted according to the right axis scale of the qubit transition frequency $\omega_q/2\pi$. Also shown is a two-parameter fit (red curve) to the extracted peak and dip positions. **b** Transition frequency $\omega_q/2\pi$ plotted versus $\delta I_\varepsilon = I_\varepsilon - I_\varepsilon^{sym}$ for three different α values for a tunable-gap gradiometric flux qubit with $\alpha_0 = 1.10$. Also shown is the result of a two-parameter fit.

the one described in Sec. 4.3 and the same as in the previous section on gradiometric fixed-gap qubits.

5.3.1 Tuning the gap with an external coil

We first discuss the experiments using a homogeneous magnetic field of a superconducting coil placed underneath the sample. The homogeneous magnetic field generates the frustrations $f_{tr,net}$ and $f_{\alpha,net}$ of the trapping and α-loop, respectively, which are given by Eq. (3.16) and (3.17).

Spectroscopy data of a tunable-gap gradiometric flux qubit is shown in Fig. 5.8. A typical set of recorded qubit spectra for a constant $\alpha = 0.68$ is depicted in Fig. 5.8**a**. The mean value of the switching current of the readout SQUID in dependence of the ε-line current I_ε reveals the qubit step and peaks and dips due to qubit excitation. The spectra belonging to different excitation frequencies $\omega_s/2\pi$ are shifted along the vertical axis according to the right axis showing the qubit transition frequency $\omega_q/2\pi$. A two-parameter fit to the extracted dip and peak positions illustrates the qubit hyperbola.

In Fig. 5.8**b**, spectroscopy data of the tunable-gap qubit are shown for three different values of α. The different α values are generated by the homogeneous magnetic field of the external coil, whereas the flux trapped during cool-down was constant at a single flux

quantum, i.e., $n=1$. It must however be noted, that the α values are not known at the beginning, but are calculated within the following analysis. We can fit the data of peak and dip positions (symbols in Fig. 5.8**b**) by a two-parameter fit yielding Δ and the slope $\partial\omega_\mathrm{q}/\partial\delta I_\varepsilon$ at large ω_q values. Here, $\delta I_\varepsilon = I_\varepsilon - I_\varepsilon^\mathrm{sym}$ is the deviation of the current I_ε sent through the ε-flux line from the value $I_\varepsilon^\mathrm{sym}$ needed for biasing the qubit at the symmetry point. To derive the persistent current $I_\mathrm{p} = (\hbar/2\Phi_0)(\partial\omega_\mathrm{q}/\partial\delta f_\mathrm{q})$ from this slope, we have to calibrate the horizontal axis. For this we need the calibration factor $\kappa \equiv \partial\delta f_\mathrm{q}/\partial\delta I_\varepsilon$ [cf. Eq. (5.1)], which is already discussed in the previous section on fixed-gap gradiometric qubits. We find $\kappa = 0.4\,\mathrm{mA}^{-1}$ similar to the values for the gradiometric fixed-gap qubits.

For the analysis of the $\Delta(\alpha)$ dependence, we need a second transfer function, relating the coil current I_coil sent through the external coil to the frustration $f_{\alpha,\mathrm{net}}$ of the α-loop. With Eq. (3.16) and Eq. (3.17), we obtain

$$\zeta \equiv \frac{\partial f_{\alpha,\mathrm{net}}}{\partial I_\mathrm{coil}} = \frac{A_\alpha}{A_\mathrm{tr}} \frac{1}{1+\beta} \frac{\partial f_\mathrm{ex}}{\partial I_\mathrm{coil}} \,. \tag{5.2}$$

With this transfer function and the expressions of Eq. (3.4) and Eq. (3.18) for I_p and α, respectively, we obtain

$$\frac{\partial\omega_\mathrm{q}}{\partial\delta f_\mathrm{q}} = \frac{2\Phi_0 I_\mathrm{p}}{\hbar} = \frac{2\Phi_0 I_\mathrm{c}}{\hbar} \sqrt{1 - \left[2\alpha_0 \left|\cos\left(\pi\zeta I_\mathrm{coil} + \pi\frac{A_\alpha}{A_\mathrm{tr}}\frac{\beta}{1+\beta}n\right)\right|\right]^{-2}} \,. \tag{5.3}$$

Using the abbreviations $\eta = 2\Phi_0 I_\mathrm{c}\kappa/\hbar$ and $I_n = (A_\alpha/A_\mathrm{tr})(\beta/1+\beta)(n/\zeta)$ this simplifies to

$$\frac{\partial\omega_\mathrm{q}}{\partial\delta I_\varepsilon} = \eta\sqrt{1 - \left[2\alpha_0 \left|\cos\left(\pi\zeta[I_\mathrm{coil} + I_n]\right)\right|\right]^{-2}} \,. \tag{5.4}$$

We can use this expression to fit the measured $\partial\omega_\mathrm{q}(I_\mathrm{coil})/\partial\delta I_\varepsilon$ dependence using η, I_n and ζ as fitting parameters.

In Fig. 5.9**a**, the measured $\partial\omega_\mathrm{q}/\partial\delta I_\varepsilon$ values are plotted versus I_coil together with a fit using Eq. (5.4). Evidently, the data points are clustered near specific I_coil values. The reason is that the homogeneous magnetic field produced by I_coil also changes the frustration of the readout SQUID and that the sensitivity of this SQUID is sufficient only in a limited range of frustration. Figure 5.9**a** shows that the expression of Eq. (5.4) fits the experimental data well, yielding values for ζ and I_n. With these fitting parameters, we can calculate $\alpha = \alpha_0\,|\cos(\pi\zeta[I_\mathrm{coil} + I_n])|$. The resulting curve is also shown in Fig. 5.9**a**. We note, however, that in this case the fit parameters I_n and ζ cannot be used to directly determine β from the expression $I_n = (A_\alpha/A_\mathrm{tr})(\beta/1+\beta)(n/\zeta)$, because the value of I_n can be distorted by an additional background magnetic field. Therefore, we use only differences ΔI_n to determine β in the following subsection. Knowing the $\alpha(I_\mathrm{coil})$ dependence, we can adjust α to any desired value by adjusting I_coil and then perform

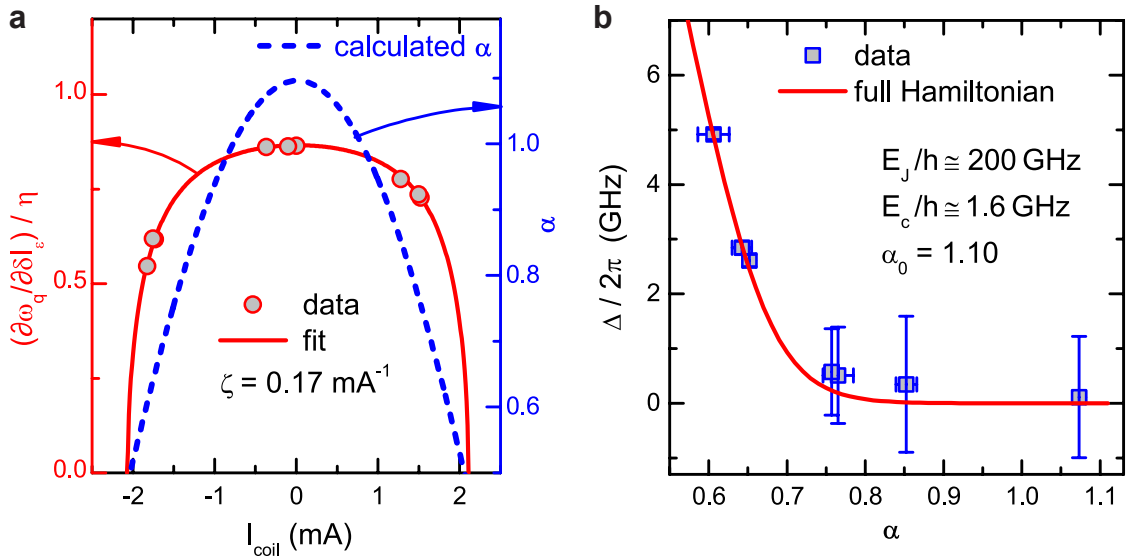

Figure 5.9: **a** Measured $\partial\omega_q/\partial\delta I_\varepsilon$ values plotted versus the coil current I_{coil} producing the homogeneous magnetic field for a tunable-gap gradiometric flux qubit. The solid line is a fit to the data using Eq. (5.4) yielding ζ and I_n. The broken line shows the calculated $\alpha(I_{coil})$ dependence for these fitting parameters. **b** Minimal qubit transition frequency $\Delta/2\pi$ plotted versus α. The solid line is obtained by numerical simulations based on the full qubit Hamiltonian using the parameters $E_J/h = 200\,\mathrm{GHz}$ and $E_c/h = 1.6\,\mathrm{GHz}$.

spectroscopy at these values. Fitting the spectroscopy data (cf. Fig. 5.8**b**), we can derive the qubit gap Δ and plot it versus α. The result is shown in Fig. 5.9**b** together with the dependence obtained from numerical simulations based on the qubit Hamiltonian. The agreement between the experimental data and the numerical simulation is best for $E_J/h = 200\,\mathrm{GHz}$ and $E_c/h = 1.6\,\mathrm{GHz}$, i.e., $E_J/E_c = 125$. We note that the E_J value agrees well with the one estimated independently from the measured junction areas and the j_c value measured for the junctions of the readout SQUID (cf. Sec. 4.1.2). This clearly shows the consistency of the data analysis and demonstrates the good control on the junction parameters fabricated on the same chip. Knowing the $\Delta(\alpha)$ and $\alpha(I_{coil})$ dependencies, we can adjust the qubit gap *in situ* by I_{coil}, while operating the qubit at the symmetry point with optimal coherence properties. This is a key prerequisite for many applications of flux qubits.

For the sample of Fig. 5.9, the qubit gap can be varied between values close to zero and approximately 5 GHz. For a second sample, our aim is to increase the tunability of the gap. According to Fig. 3.4, this can be achieved by increasing the ratio E_J/E_c of the qubit junctions. To this end, we reduce the oxidation time for the junction barrier. From the pre-characterization of the corresponding readout SQUID (cf. Fig. 4.2**b**), we confirm a higher current density and an increased Josephson energy $E_J/h = 800\,\mathrm{GHz}$. Besides, the maximum value of α is designed to $\alpha_0 = 0.7$, which makes it easier to tune

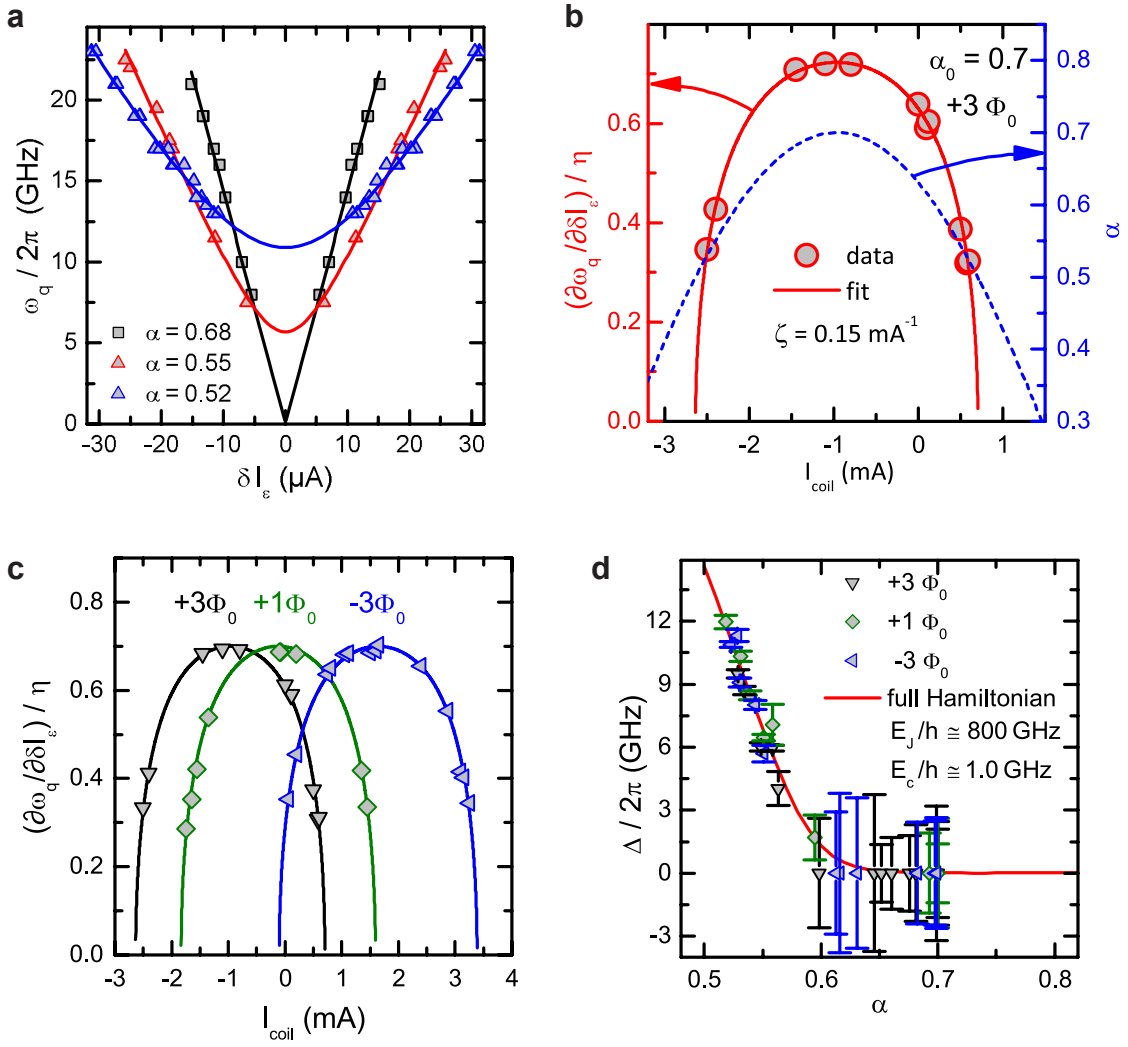

Figure 5.10: **a** Transition frequency $\omega_q/2\pi$ plotted versus $\delta I_\varepsilon = I_\varepsilon - I_\varepsilon^{\rm sym}$ for a tunable-gap gradiometric flux qubit with $\alpha_0 = 0.7$. Also shown is the result of a two-parameter fit. **b** Measured $\partial\omega_q/\partial\delta I_\varepsilon$ values plotted versus the current $I_{\rm coil}$ through the external coil producing the homogeneous magnetic field for $n = +3$ trapped flux quanta. The solid line is a fit to the data by Eq. (5.4) yielding ζ and I_n. The broken line shows the calculated $\alpha(I_{\rm coil})$ dependence for these fitting parameters. **c** Measured values as in **b** for three different values of the number of trapped flux quanta, $n = -3, +1, +3$, fitted with consistent parameters. From the horizontal displacement of the different curves we obtain $\Delta I_n/\Delta n = 0.43\,\mathrm{mA}$. **d** Minimal qubit transition frequency $\Delta/2\pi$ plotted versus α for three different values of trapped flux quanta. The solid line is a fit of the data based on the full qubit Hamiltonian with the fitting parameters $E_{\rm J}/h = 800\,\mathrm{GHz}$ and $E_{\rm c}/h = 1.0\,\mathrm{GHz}$.

α into the regime of high qubit gap. Moreover, this sample is characterized for three different values of trapped flux quanta to yield, in total, a larger consistent set of data. The overall behavior of this sample as shown in Fig. 5.10 is very similar to the previous one, but the qubit gap can now be tuned to values above 10 GHz as shown in Fig. 5.10**d**. This data can be very well described by the full qubit Hamiltonian with input parameters

$E_J/h = 800\,\mathrm{GHz}$ and $E_c/h = 1\,\mathrm{GHz}$. The latter is in very good agreement with the specific junction capacitance c_s determined in Sec. 4.1.2.

5.3.2 Determination of inductance ratio

Next, we investigate the tunability of this sample for different amounts of trapped flux quanta n. In Fig. 5.10**c**, we plot $\partial\omega_q/\partial\delta I_\varepsilon$ versus the current I_{coil} through the external coil for three different values of the trapped flux ranging from $n = -3$ to $n = +3$. Evidently, the general shape of the three curves is very similar as well as the obtained fitting parameters ζ and η. The shift along the horizontal axis is expected from Eq. (5.4) and can now be used to calculate β. Starting with the expression $I_n = (A_\alpha/A_{tr})(\beta/1+\beta)(n/\zeta)$, we only use differences $\Delta I_n = I_{n,i} - I_{n,j}$. They correspond to differences $\Delta n = n_i - n_j$ and result in $\Delta I_n = (A_\alpha/A_{tr})(\beta/1+\beta)(\Delta n/\zeta)$. For our sample, we find a mean value of $\Delta I_n/\Delta n = 0.43\,\mathrm{mA}$, finally yielding

$$\beta = \left(\frac{\Delta n}{\Delta I_n \zeta}\frac{A_\alpha}{A_{tr}} - 1\right)^{-1} = 0.52\,. \tag{5.5}$$

This value is in reasonable agreement with the one derived from the L_g and L_k values which can be estimated from the qubit geometry, the cross-sectional area of the superconducting lines and the dirty limit expression of L_k (cf. Sec. 4.2.1). We note that the result from Eq. (5.5) can be considered as more precise because it is computed directly from the sample.

5.3.3 Gradiometer quality

Similar to the fixed-gap gradiometric qubit in Sec. 5.2.3, we investigate the gradiometer quality also for the tunable-gap qubit. It must be expected that the implementation of the α-SQUID loop perturbs the symmetry of the gradiometric layout and thus reduces its gradiometer quality. A finite imbalance of the gradiometric qubit becomes evident during the spectroscopy measurements. When the qubit gap is varied by applying different magnetic fields to the α-loop, then the position of the qubit step I_ε^{sym} in the ε-current is shifted as well as the positions of peak and dip for the same excitation frequency. After a calibration with the factor κ ($\kappa = 0.5\,\mathrm{mA}^{-1}$ for the qubit with $\alpha_0 = 0.7$ of Fig. 5.10, for which we now determine the gradiometer quality), the varying qubit step position is expressed by the gradiometer imbalance δf_{imb}. It is plotted in Fig. 5.11**a** for three different amounts of trapped flux as a function of the external frustration f_{ex}, which refers to the whole qubit area (trapping loop area). Obviously, the qubit imbalance changes linearly with the applied frustration analogously to the case of the fixed-gap gradiometric qubit (cf. Fig. 5.6**b**). The inverse slope of linear fits – one for each trapped flux quanta – to

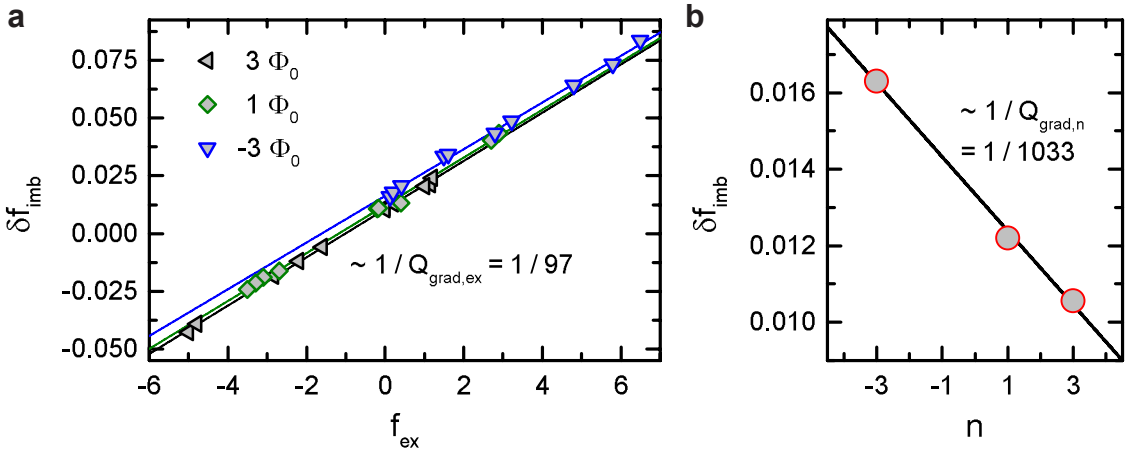

Figure 5.11: Gradiometer imbalance of the tunable-gap qubit with $\alpha_0 = 0.7$ characterized in Fig. 5.10. **a** The change of the qubit working point δf_{imb} is plotted versus the external frustration f_{ex} for different numbers of trapped flux quanta. The slopes of linear fits to these data yield the quality factor $Q_{\mathrm{grad,ex}} = 97$. **b** The shift of the linear fits in **a** for different number n of trapped flux quanta is plotted together with a linear fit, which results in a quality factor $Q_{\mathrm{grad,n}} = 1033$.

these data give us the quality factor $Q_{\mathrm{grad,ex}} = 97$ according to Eq. (3.21). The three linear fits to the different flux quanta data yield approximately the same slope, yet they are shifted vertically with respect to each other. This imbalance as a function of n trapped flux quanta can be seen more clearly in Fig. 5.11**b**. Although the set of data is not very large, we can also apply a linear fit to determine the quality factor $Q_{\mathrm{grad,n}} = 1033$.

Compared to the values for the fixed-gap gradiometer, $Q_{\mathrm{grad,n}}$ is very similar, whereas $Q_{\mathrm{grad,ex}}$ is reduced by a factor $\simeq 10$. Consequently, the total quality factor $Q \simeq 90$ is decreased by a factor $\simeq 5.5$. Thus, we conclude that the quality $Q_{\mathrm{grad,ex}} = \left(\frac{\delta A}{A} - \frac{\delta L_{\mathrm{g}} + \delta L_{\mathrm{k}}}{L_{\mathrm{g}} + L_{\mathrm{k}}}\right)^{-1}$ is reduced due to the deviations of the subloop areas, whereas imperfections in kinetic and geometric inductance, that solely enter $Q_{\mathrm{grad,n}}$, do not seem to change for the tunable-gap qubit.

In summary, the increased imbalance of 1.1% of the tunable-gap gradiometric qubit needs to be considered. The change of the qubit step position is in the range of $20\,\mathrm{m}\Phi_0$ for a complete tuning of the qubit gap from zero to its maximum value. However, this small imbalance can be easily compensated with the ε-current to ensure the stable operation of the qubit at its degeneracy point for future experiments.

5.3.4 Tuning the gap with the on-chip α-line

We finally address the tuning of Δ by the on-chip α-flux line. Since the maximum current is limited by the critical current of the α-line and by heating effects in contacts, only small variations of the frustration of the α-loop are possible. Therefore, a constant

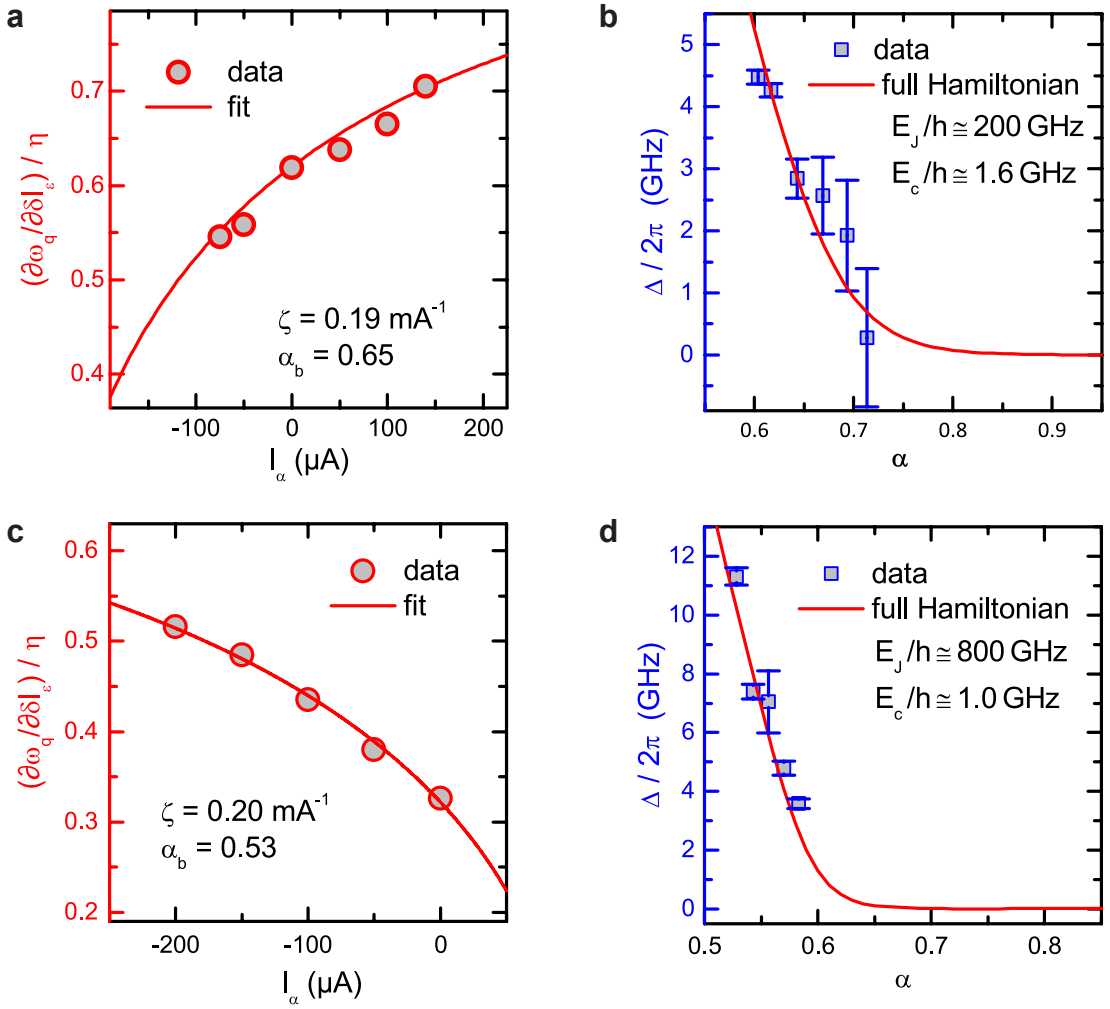

Figure 5.12: **a** and **c** Measured $\partial\omega_{\rm q}/\partial\delta I_\varepsilon$ values plotted versus the current I_α through the α-flux line for two tunable-gap gradiometric flux qubits. The solid lines are fits to the data by Eq. (5.7) yielding the fitting parameter $\widetilde{\zeta}$. **b** and **d** Minimal qubit transition frequency $\Delta/2\pi$ plotted versus α of the qubits of **a** and **c**. The solid lines are obtained from numerical simulations based on the full qubit Hamiltonian using the parameters $E_{\rm J}/h$ and $E_{\rm c}/h$ as listed in the subfigures. The data in (**a**,**b**) and (**c**,**d**) are obtained for the two samples of Fig. 5.9 and Fig. 5.10, respectively, however with on-chip control of Δ via the α-flux line.

applied magnetic field or a proper number of trapped flux quanta are used to pre-bias the qubit at a value $\alpha_{\rm b}$, where the slope of the $\Delta(\alpha)$ dependence is steep. Then, I_α is used to vary α around this value. In our experiments, a constant applied field is used to set $\alpha_{\rm b}$. Since the variation of the frustration of the α-loop is generated by I_α instead of $I_{\rm coil}$, we have to use the modified calibration factor

$$\widetilde{\zeta} \equiv \frac{\partial f_{\alpha,\rm net}}{\partial I_\alpha} \,. \tag{5.6}$$

With this factor, we obtain

$$\frac{\partial\omega_{\mathrm{q}}}{\partial\delta I_{\varepsilon}} = \eta\sqrt{1-\left[2\alpha_0\left|\cos\left(\arccos(\alpha_{\mathrm{b}})+\pi\widetilde{\zeta}I_{\alpha}\right)\right|\right]^{-2}}\,. \tag{5.7}$$

We can use this expression to fit the measured $\partial\omega_{\mathrm{q}}/\partial\delta I_{\varepsilon}$ versus I_{α} dependence using $\widetilde{\zeta}$ as fitting parameter. Based on these results, we can calculate $\alpha = \alpha_0\left|\cos\left(\arccos(\alpha_{\mathrm{b}})+\pi\widetilde{\zeta}I_{\alpha}\right)\right|$. Knowing α, we can use the Δ values obtained from two-parameter fits of the spectroscopy data to get the $\Delta(\alpha)$ dependence. Experimental data for the two samples of Fig. 5.9 and Fig. 5.10 are shown in Fig. 5.12. In Fig. 5.12**b** and Fig. 5.12**d**, we compare the experimental $\Delta(\alpha)$ curves to numerical simulations based on the full qubit Hamiltonian with the same E_{J} and E_{c} values as obtained by tuning α with the coil current (cf. Fig. 5.9**b** and Fig. 5.10**d**). The very good agreement between measurement data and calculation demonstrates again the consistency of our data analysis. All in all, our data clearly show that the qubit gap can be varied in a controlled way over a wide range by varying the frustration of the α-loop of the gradiometric flux qubits either by an external coil or an on-chip control line.

5.4 Summary

Summing up, we demonstrate a systematic evolution from the standard 3-JJ flux qubit via a fixed-gap gradiometric version to the tunable-gap gradiometric qubit at the end. The working principle of gradiometer and trapping loop are successfully demonstrated and the gradiometer quality is determined to be sufficiently high. The gap of tunable-gap gradiometric flux qubits can be reliably tuned over a wide range up to more than 10 GHz, making them attractive for a large number of applications. All in all, our results show that the measured data agree well with the behavior expected from theory.

However, in contrast to pulsed SQUID readout techniques or circuit QED experiments, the qubit gap cannot be measured directly. Also, the spectroscopy measurement used here is relatively time consuming for the characterization of a flux qubit. Although these measurements constitute a good compromise considering their benefits (easy sample mounting, well manageable measurement technique and, especially, availability of the cryostat) the consequent next step is to integrate the tunable-gap qubit into a circuit QED architecture, paving the way to interesting future experiments.

Chapter 6

The tunable-gap flux qubit in a circuit QED architecture

The following chapter deals with the integration of a tunable-gap flux qubit into a circuit QED architecture. Circuit QED is the solid-state analog of cavity QED in quantum optics, where single atoms interact with the electromagnetic field inside a cavity resonator. Analogously, the flux qubit as an artificial atom interacts via its magnetic moment with the magnetic field of a superconducting coplanar waveguide resonator. The much higher coupling strengths in circuit QED, the large design flexibility and, in our setup, the in-situ tunability of the flux qubit at optimal coherence allow us to study light-matter on a fundamental level. To our knowledge, we report on the first implementation of a tunable-gap flux qubit inside a CPW resonator.

This chapter is arranged as follows: In Sec. 6.1, we discuss the basic coupling between the gradiometric tunable-gap qubit and a CPW resonator and present the sample layout. Next, Sec. 6.2 describes the pre-characterization of the resonator and flux calibration measurements of the qubit. Afterwards, we spectroscopically analyse the coupled qubit-resonator system in Sec. 6.3. There, we also demonstrate the tuning of the qubit gap, but rather focus on the determination of basic properties such as coupling strengths. A study on the tunability of the qubit gap is presented in Sec. 6.4. We determine the gradiometer quality of this qubit in Sec. 6.5 and summarize our results in Sec. 6.6.

6.1 Sample layout

In order to couple a persistent current flux qubit to a CPW resonator, the qubit is usually placed at a position of high magnetic field strength of the standing wave profile inside the CPW resonator. Then, the large magnetic moment of the flux qubit, linked with its persistent current I_p, interacts with the oscillating magnetic field of the resonator. The

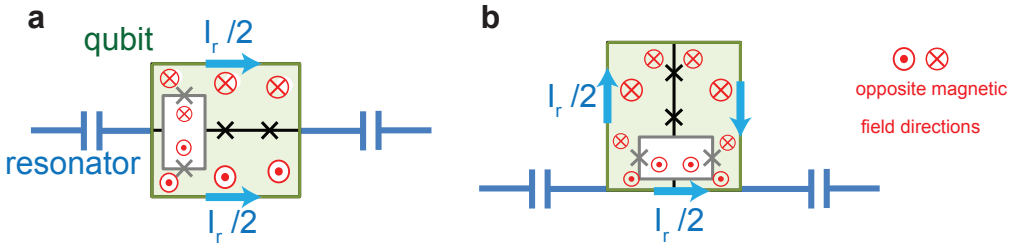

Figure 6.1: Alternative coupling schemes for the gradiometric tunable-gap flux qubit. **a** The resonator current generates an effective coupling to the gradiometric qubit persistent current and no net magnetic field in the α-loop. **b** The gradiometer prevents a coupling of the resonator to the qubit persistent current. However, the resonator current couples to the α-loop.

interaction strength g can be described by

$$\hbar g_n = M I_\mathrm{p} I_{\mathrm{r},n} \ , \tag{6.1}$$

where M is the mutual inductance between qubit and resonator and $I_{\mathrm{r},n}$ is the (high-frequency) current of the n^{th} resonator mode. By a galvanic contact between qubit and the inner conductor of the resonator, the mutual inductance M is strongly increased due to the contribution of the kinetic inductance L_kin of the shared superconducting line. Consequently, the coupling strength is enhanced compared to the case of pure inductive coupling and the strong coupling regime can be reached straightforwardly [75]. For the case of the gradiometric tunable-gap qubit with its more complex design, one has to take care of how to properly connect qubit and resonator. In Fig. 6.1, two possible schemes for galvanic coupling are displayed. To get an intuitive understanding of the coupling in each case, we consider the magnetic field generated by the resonator current in the different loops of the qubit. A resonator current (with gigahertz frequency) along the line containing the qubit JJs is neglected in this consideration due to the large inductance of the JJs. In the scheme of Fig. 6.1**a**, the resonator current I_r splits equally to the upper and lower branch of the gradiometric loop. These currents generate magnetic fields of opposite sign in the two gradiometer subloops. Therefore, the resonator current effectively couples to the qubit magnetic energy bias or persistent current, respectively (σ_z coupling). Furthermore, the fields in the α-loop cancel each other.

The situation is, however, quite different for the coupling scheme of Fig. 6.1**b**. The same magnetic field (amount and direction) in the gradiometric subloops prevents a coupling to the qubit persistent current. In contrast, there is a net field contribution to the α-loop. In this way, the resonator is not coupled to the qubit via its magnetic energy bias but via the qubit gap Δ (σ_x coupling [103]). However, the α-loop does not directly share a line with the resonator in the qubit layout of Fig. 6.1**b**. Only with a considerable

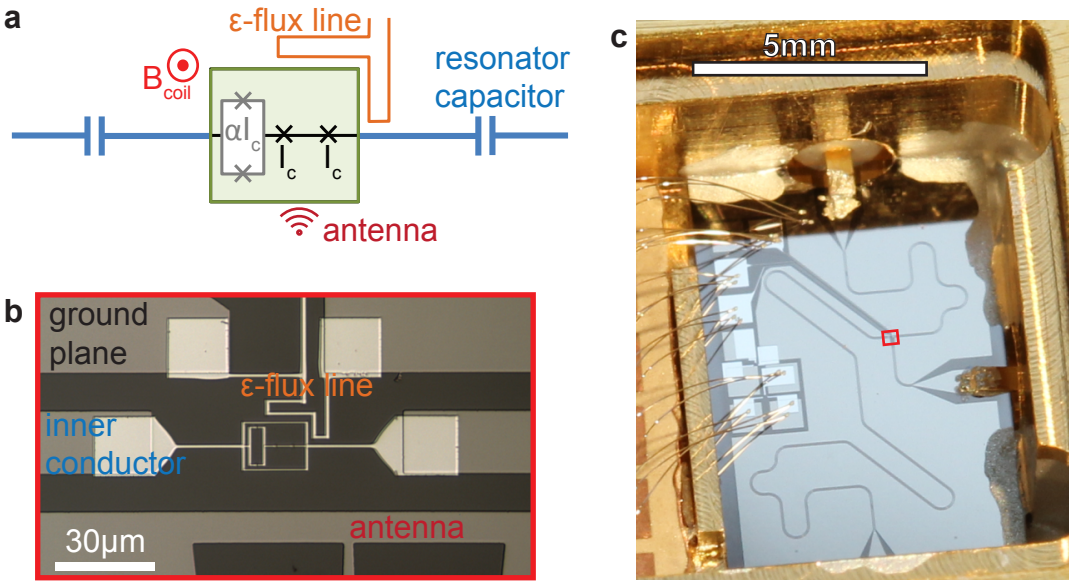

Figure 6.2: **a** Circuit schematics of a microwave resonator galvanically coupled to a gradiometric tunable-gap flux qubit with ε-flux line and microwave antenna. **b** Optical micrograph of the qubit inside the CPW resonator. One can clearly distinguish aluminum structures (white), niobium (gray) and the dark (oxidized) silicon substrate. **c** Photograph of the sample chip mounted inside a gold-plated copper box. The red rectangle marks the position of the enlarged view in **b**.

change of the qubit layout, a galvanic coupling between resonator and α-loop can be reached. Therefore, we restrict ourselves to the case of coupling to the qubit persistent current with the qubit layout extensively studied in the Chapter 5. Nevertheless, it would be very interesting to study and compare both types of coupling mechanism in future experiments.

The schematic layout of our sample is shown in Fig. 6.2**a**. For this first implementation of the gradiometric tunable-gap flux qubit inside a CPW resonator, we adopt the principle to change as little of the relevant qubit layout as possible compared to the layouts studied in the previous chapter. The dimensions of the qubit and its subloops are unchanged as well as the shape of the ε-flux bias line close to the qubit. Yet, we omit the α-flux bias line (cf. Fig. 5.7), as it can obviously not be placed in the same location next to the qubit when inside a CPW resonator. Also, the on-chip α-line is not essential to demonstrate the tunability of the qubit gap as long as we can use an external coil to change f_α. There exists, however, a sample layout for a gradiometric tunable-gap qubit inside a CPW with both an ε- and an α-line, which can be realized in future work [104].

The ε-flux bias line is designed in a way that the ground plane is not cut into two pieces (see Fig. 6.2**b**). We accept that only part (approximately half) of the ε-current will flow nearby the qubit in order to avoid possible negative effects of a split ground plane on the resonator quality. The ε-feed line ends in a square pad ($0.4\,\mathrm{mm}^2$) in one

corner of the $(10\,\mathrm{x}\,6)\,\mathrm{mm}^2$ large chip (cf. Fig. 6.2**c**). From this pad and from the resonator ground plane, bond wires connect the ε-line to PCB copper pads next to the chip inside the sample box. Copper wires soldered onto these copper pads exit the sample box via small holes as illustrated in Fig. 4.8**c** of Sec. 4.4. The additional bond pads on the chip connect to SQUIDs for pre-characterization and testing. In addition to the ε-line, an on-chip microwave antenna allows qubit excitation. This antenna is connected to one of the SMA ports of the sample box. The other two SMA connectors are used for input and output ports of the CPW resonator.

6.2 Sample pre-characterization

6.2.1 Resonator characterization

We first analyze the CPW resonator with respect to its resonant frequencies and quality factors. We therefore perform a transmission measurement with a VNA as described in Sec. 4.4.2. Meanwhile, the qubit is far detuned (with magnetic flux), such that it has no influence on the resonator. Figure 6.3**a** shows a transmission power spectrum over a wide range of input frequency $\omega_{\mathrm{rf}}/2\pi = 2 - 10\,\mathrm{GHz}$. We choose this range to accommodate for the experimental requirements of our flux qubits and technical limitations due to the operating frequencies of cryogenic amplifiers and circulators. The transmission power magnitude is plotted in a logarithmic scale, $10\log(P_{\mathrm{in}}/P_{\mathrm{out}})\mathrm{dB}$, where P_{in} and P_{out} are the input and output port power of the VNA, respectively. There are four narrow maxima in the transmission spectrum, which constitute resonant harmonic modes of the $\lambda/2$-resonator. Accordingly, we refer to the fundamental mode at $\omega_1/2\pi = 2.504\,\mathrm{GHz}$ as $\lambda/2$-mode, whose resonant frequency is determined by design of the length of 25 mm of the CPW resonator. The higher harmonic modes are λ-mode ($\omega_2/2\pi = 4.814\,\mathrm{GHz}$), $3\lambda/2$-mode ($\omega_3/2\pi = 6.959\,\mathrm{GHz}$) and 2λ-mode ($\omega_4/2\pi = 9.201\,\mathrm{GHz}$).

The different standing wave profiles of the resonator current linked with these modes are illustrated in Fig. 6.3**b**. The qubit is located at 1/4 of the length of the resonator. As this position coincides with a node of the 2λ-mode, the latter does not couple to the qubit, as $I_{\mathrm{r}} = 0$ in Eq. (6.1). In contrast, the λ-mode reaches maximum current at the qubit position and thus couples strongest to it. The two remaining modes are expected to show similar, significant coupling to the qubit. However, the fundamental frequency of the $\lambda/2$-mode actually lies out of the specified frequency range of the cryogenic amplifier. Here, the amplification is strongly reduced. Consequently, this mode shows a smaller signal-to-noise ratio. In the following measurements, it is therefore not used as a readout mode for two-tone spectroscopy, but it is, nevertheless, used for the transmission spectroscopy of the qubit.

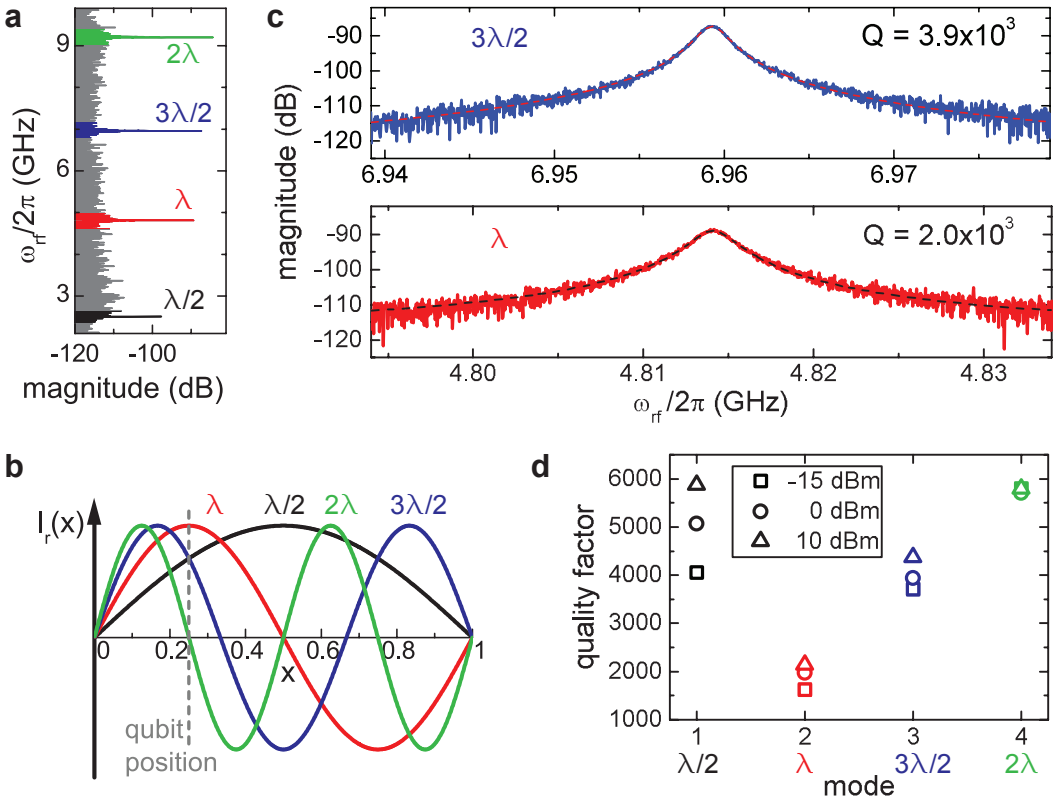

Figure 6.3: Characterization of the CPW resonator (qubit far detuned): **a** Transmitted power spectrum (dB-scale) as a function of the probe frequency ω_{rf}. Away from the four narrow resonances (modes) the resonator strongly filters the transmitted signal by $20-40\,\mathrm{dB}$. **b** Sketch of the standing wave profile of the resonator current I_{r} along the resonator length coordinate x for the four lowest modes. **c** Enlarged view of the power transmission at the resonances of the λ-mode ($\omega_2 = 4.814\,\mathrm{GHz}$, top panel) and the $3\lambda/2$-mode ($\omega_3 = 6.959\,\mathrm{GHz}$, bottom panel). Also shown are Lorentzian fits (dashed lines), which yield the depicted quality factors. These spectra are recorded with a low probe power corresponding to only 1.4 poa (photons on average) in the cavity. **d** Quality factors for four modes and three different power values are dominated by internal losses.

The two most important modes are, however, the λ- and $3\lambda/2$-modes, which are shown in detail in Fig. 6.3**c**. Note that the absolute number of the transmission magnitude ($\simeq -90\,\mathrm{dB}$ at the resonances) is not quantitatively relevant, since this value includes the total input line attenuation and cable losses (cf. Sec. 4.4; in total $\simeq -150\,\mathrm{dB}$) and the total (cryogenic and room temperature) amplification ($\simeq 65\,\mathrm{dB}$). Since these value are only known with an uncertainty of a few dB, and the exact resonator transmission amplitude is not relevant for the following measurements, a calibration of the transmission scale is omitted here. More importantly, however, the output power of the VNA for these measurements is set to a value $P_{\mathrm{out}} = 0\,\mathrm{dB}$, corresponding to only 1–2 photons on average (poa) in the resonant mode (cf. Sec. 6.2.3). Such a small power in the resonator is necessary for the qubit measurements in the following sections. Since the quality of the

resonator modes is power dependent, it has to be determined in this low-power regime.

The quality factor $Q_n = \omega_n/\kappa_n$ of the n^{th} resonator mode is extracted by fitting the Lorentzian resonance curve of the transmitted power with a function

$$P(\omega) = A\frac{\kappa_n/2}{(\omega-\omega_n)^2 + (\kappa_n/2)^2} \tag{6.2}$$

where $A = P_{n,0} \cdot \kappa_n/2$ is linked with the maximum transmitted power in resonance, $P_{n,0}$. The Lorentzian fits in Fig. 6.3**c** show very good agreement with the measured data. The quality factors extracted from these fits are on the order of several thousand and we find loss rates $\kappa_1/2\pi = 0.49\,\text{MHz}$, $\kappa_2/2\pi = 2.4\,\text{MHz}$ and $\kappa_3/2\pi = 1.7\,\text{MHz}$. An overview of the quality factors of the different modes is given in Fig. 6.3**d**. Here, the quality factors for the four first resonator modes are determined for three different values of output power of the VNA ($-15\,\text{dBm}$, $0\,\text{dBm}$, $+10\,\text{dBm}$) corresponding to a resonator population of approximately $0.03\,\text{poa}$, $1.4\,\text{poa}$ or $14\,\text{poa}$, respectively.

For each mode, the quality increases with increasing power. This effect is strongest for the $\lambda/2$-mode. However, the fact that a certain increase in power has more effect on the quality for this mode, might also be influenced by the lower amplification and lower signal-to-noise ratio for this mode. In contrast, the 2λ-mode shows less influence of the power on its quality. We find that the quality factors shown here are determined by the interplay of the resonator modes with the qubit and the additional structures (antenna, ε-line) surrounding the qubit. Recent studies on the quality of the resonator at the WMI showed [105], that the resonator is mainly limited by internal losses arising from the oxide interface layer between niobium and aluminum in the center strip of the CPW resonator. Both pure niobium resonators with uninterrupted center strip as well as resonators with aluminum constriction (without qubit) and ion gun treatment of the niobium resonator before deposition of aluminum, reach quality factors that are one order of magnitude higher than the ones reported here. Hence, it can be concluded that the loaded quality Q_L we determine is approximately equal to the internal quality $Q_\text{L} \approx Q_\text{int}$, as the losses caused by the introduction of the qubit structure with JJs and Nb-Al interface are predominant. This is also supported by the finding that especially niobium suffers from losses due to TLS at its surface [106, 107]. Also, the improvement of quality factors with increasing power as displayed in Fig. 2.6**d** is in agreement with TLS behavior [108, 109]. Moreover, the comparison to a similar resonator-qubit sample with antenna but without ε-line [95] shows that the addition of the ε-line has no further strong impact on the quality factor. Furthermore, this consideration allows us to qualitatively understand the different quality factors for the different modes.

As the quality is dominated by the internal losses caused by the sum of modifications to the resonator at the position of the qubit, this detrimental effect is the stronger the

larger the coupling of the mode is to the qubit – that means the larger the current of the mode at the qubit position. Accordingly, the λ-mode with strongest coupling to the qubit (cf. Fig. 6.3**b**) suffers from the lowest quality factor. Moreover, the $\lambda/2$- and $3\lambda/2$-modes with equal coupling to the qubit show similar quality. Highest quality is reached for the 2λ-mode with no coupling to the qubit. However, a more quantitative discussion would have to take into account the interplay between internal and external quality and their dependencies on the mode number n ($Q_{\mathrm{int}}(n) \sim n$, $Q_{\mathrm{ext}}(n) \sim 1/n$) [62].

Although there may be room for improvement of the internal resonator quality, it can be summarized that the resonator is working well. Especially the opening of one side of the ground plane and insertion of the ε-line brought no dramatic deterioration of the resonator quality. The λ- and $3\lambda/2$-mode are well-suited for the readout of the gradiometric tunable-gap quibt, as can be seen in the following sections.

6.2.2 Flux calibration

After this pre-characterization of the CPW resonator, we continue with the investigation of the qubit. Here, we first need to calibrate the magnetic flux in the qubit loop generated by, both, the external coil and the on-chip ε-line. We use resonator transmission spectroscopy to monitor the qubit via its effect on the transmitted signal caused by the resonant and dispersive interactions of circuit QED (cf. Sec. 3.4).

External magnet coil calibration

A calibration of the magnetic flux generated by the external coil is helpful, as this coil is used later on to frustrate the α-loop and, thus, tune the qubit gap. Furthermore, we need this calibration in order to calibrate also the ε-line current in the next subsection. The sample investigated here does not have a direct measure for magnetic flux [1] as the samples of Chapter 5, where the readout SQUID is used to calibrate the field applied with the external coil – considering also screening effects. Nevertheless, a calibration of magnetic flux is also possible here by exploiting the finite imbalance of the gradiometer.

An ideal gradiometric qubit would be completely insensitive to an externally applied homogenous magnetic field. However, the implementation of an α-loop into the qubit brings a perturbation to the gradiometric behavior (cf. Sec.5.3.3) and one has to trade off minimal imbalance (small α-loop) against maximum tunability of α also with on-chip lines (large α-loop). As it turns out (cf. Sec. 6.5), the gradiometer imbalance for this sample is unexpectedly large. However, a certain imbalance is indeed very useful, as it allows us to calibrate the magnetic flux generated by the external coil.

Figure 6.4**a** shows the measurements for the flux calibration of the external coil. For

[1] Test SQUID for flux measurement on the sample chip was broken.

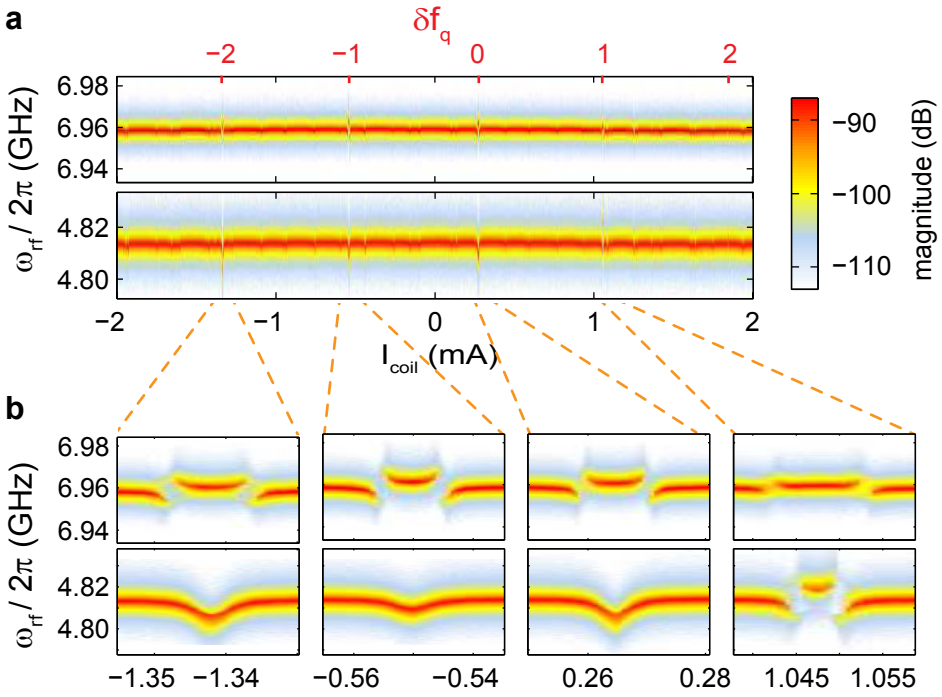

Figure 6.4: Magnet coil calibration: **a** The power transmission spectra of the λ- and $3\lambda/2$-modes of the resonator (with input power corresponding to 15 poa) versus the coil current I_{coil} reveal periodic signatures of the qubit, that are shown on an enlarged scale in **b**. Closeup on four qubit signatures, revealing anticrossings or dispersive shifts.

each value of the coil current I_{coil}, transmission spectra of the resonator at its λ- and $3\lambda/2$-modes are shown. The color-coded power transmission magnitude reveals four regions, where the frequency with maximum transmission deviates considerably from the bare resonant frequency. These regions are shown on an enlarged scale in Fig. 6.4**b**. Obviously, there appear anticrossings of the $3\lambda/2$-mode at each position. The λ-mode experiences either a dispersive shift or an anticrossing, as well. The details of this manifestation of the qubit coupled to the resonator are discussed in detail in the following section. Here it is sufficient to state, that these are clear signatures of the qubit, that appear at periodic distances in I_{coil}. This means, that the homogenous magnetic field of the external coil frustrates the qubit loop because of a finite gradiometer imbalance. From the mean distance between two next qubit signatures the coil current can be calibrated to a magnetic flux quantum, which defines the periodicity of the qubit magnetic energy bias [cf. Eq. (3.6)]. From seven of these neighboring qubit signatures (not all shown in Fig. 6.4), we determine a calibration factor

$$\gamma \equiv \frac{\partial \delta f_{\mathrm{q}}}{\partial I_{\mathrm{coil}}} = 1.2605\,\mathrm{mA}^{-1}\,. \tag{6.3}$$

The calibrated qubit frustration δf_q is also shown in Fig. 6.4 (top axis). There, the origin is set arbitrarily because of an unknown background magnetic field.

It must also be mentioned, that the ability to address the qubit with the external coil provides another experimental convenience. It is, in this case, not necessary to bias the qubit near the degeneracy point by flux trapping, as it is demonstrated in Sec. 5.2.1. Flux trapping requires a rough knowledge on the magnetic field necessary to trap a certain number of flux quanta. Since this is not the case here due to the lack of a SQUID magnetometer, the gradiometer imbalance makes locating and characterization of the qubit much easier. Nevertheless, for future samples of a gradiometric tunable-gap qubit in a CPW resonator, the experience of this work will allow for the reduction of the gradiometer imbalance.

Apart from the periodic appearance of the qubit in the coil current sweep, one should notice the different shape of the qubit signatures in Fig. 6.4**b**. This change in the transmission spectra already reflects a tunability of the qubit gap Δ, which is expected to happen when the homogenous magnetic field frustrates the α-loop. A systematic investigation of this tunability is presented in Sec. 6.4.

ε-flux bias line calibration

The measurements presented in the previous subsection show that the external coil can be used to sweep the qubit through its degeneracy point by exploiting the finite gradiometer imbalance. However, the homogenous coil field simultaneously changes the α-loop frustration. Hence, for the proper characterization of the qubit parameters, we tune the qubit bias with the on-chip ε-line. The latter is also tested to have negligible influence on f_α. A qubit measurement via the ε-line is performed after biasing the qubit close to the degeneracy point with the external coil.

A direct calibration of the ε-line current by sweeping the qubit magnetic energy bias over a whole period is impossible due to the high necessary currents (similar to the samples in Chapter 5). With the preceding calibration of the qubit frustration versus the current I_{coil} of the external coil, it is now straightforward to calibrate also the ε-flux bias line with respect to its frustration of the qubit. To this end, we compare a qubit spectrum generated by a sweep of the calibrated coil current with a spectrum generated by an ε-sweep. Of course it must be guaranteed that the qubit parameters are the same for these two sweeps. In particular, the qubit gap Δ must be equal, as this implies the same persistent current I_p and thus the same dependence on magnetic flux as expressed by Eq. (3.6). Experimentally, this situation is established by the following procedure: First, a qubit spectrum is monitored by sweeping the coil current. Then, the coil current is set to the constant bias of the degeneracy point of the qubit (symmetry

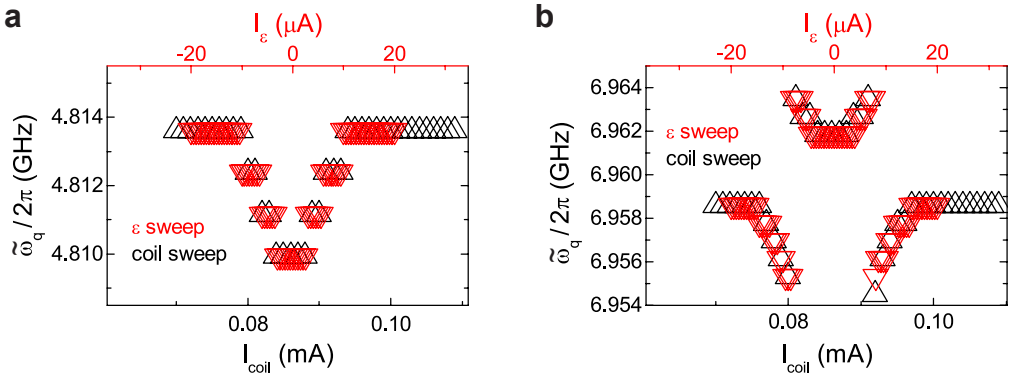

Figure 6.5: Calibration of the ε-line is achieved by comparing the dressed qubit frequency $\tilde{\omega}_\mathrm{q}$ between a sweep with the coil (black, bottom axis) and a sweep with the ε-flux line (red, top axis). **a** λ-mode **b** $3\lambda/2$-mode.

point of the recorded spectrum). Now, the qubit spectrum is reproduced by a sweep of the ε-current. For checking purposes, the qubit gap is also determined in both cases by a two-tone experiment at the degeneracy position in coil and ε-current, respectively. In Fig. 6.5, one example of this calibration measurement is shown. For clarity, only the frequency $\tilde{\omega}_\mathrm{q}$ of maximum transmission is plotted. For each of the λ- (**a**) and the $3\lambda/2$-mode (**b**), the spectrum of a coil sweep is depicted in black colour (bottom horizontal axis). The spectrum of the ε-sweep (red colour) coincides very well with the coil sweep spectrum, after the ε-current axis is scaled accordingly. Completing this process for three different qubit signals (with different qubit gap), we determine a mean calibration factor [cf. Eq. (5.1)]

$$\kappa \equiv \frac{\partial \delta f_\mathrm{q}}{\partial \delta I_\varepsilon} = 0.83\,\mathrm{mA}^{-1}\,. \tag{6.4}$$

It must finally be stated that this calibration of the ε-current is much more direct than the procedure used in Chapter 5, where the JJ parameters E_J and E_c enter into the comparison between simulation and measured data. A flux calibration is a necessary prerequisite to determine all relevant qubit parameters quantitatively, e.g., the coupling strengths to the resonator modes that are extracted from transmission spectroscopy in the following.

6.2.3 Power calibration

In this subsection, the photon number dependent ac-Zeeman shift is used to calibrate the photon number inside the resonator. To this end, we perform a two-tone measurement of the qubit at its degeneracy point. The dressed qubit frequency $\tilde{\omega}_\mathrm{q}$ of Eq. (3.29) then contains the ac-Zeeman contribution $2g_n^2 N/\delta$. When coupling strength g_n and detuning δ are known, the photon number N can be calibrated from the shift of $\tilde{\omega}_\mathrm{q}$ for varying

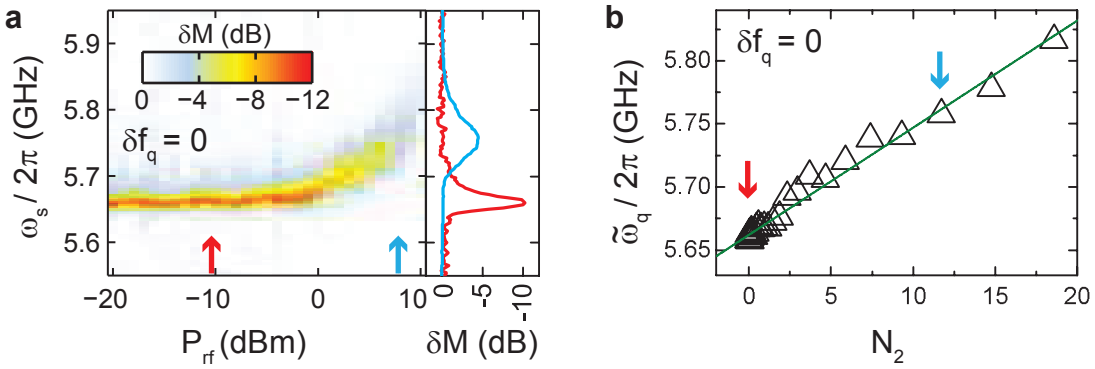

Figure 6.6: Resonator power calibration by a two-tone spectroscopy of the ac-Zeeman shift at the qubit degeneracy point. **a** For increasing ZVA power P_{rf}, the onset and increase of the shift can be detected. The right panel shows two cuts of the color-coded plot marked with the blue (considerable shift) and red (no shift) arrows. **b** Dressed qubit frequency $\tilde{\omega}_{\mathrm{q}}$ extracted from **a** plotted versus the calibrated photon number N_2 in the λ-mode. The arrows mark the same power values as in **a**.

input power to the resonator mode. Here, we want to point out the interdependencies of the qubit characterization. For the accurate determination of the coupling strengths in Sec. 6.3, we have to realize an experimental situation with low resonator population. However, the coupling strengths have to be known for a quantitative power calibration. In practice, this requires some iterative measurements.

Figure 6.6 shows the power calibration measurements. The color-coded plot of Fig. 6.6**a** displays the change of the transmission at the dressed qubit-resonator frequency $\tilde{\omega}_{\mathrm{q}}$ due to the excitation with the signal tone ω_{s} (with fixed power $P_{\mathrm{s}} = -20\,\mathrm{dBm}$). For low resonator input power corresponding to low ZVA output power P_{rf} up to approximately 0 dBm, $\tilde{\omega}_{\mathrm{q}}$ stays constant. For higher power, the photon number dependent ac-Zeeman contribution leads to a measurable shift of $\tilde{\omega}_{\mathrm{q}}$. Also, the shape of the two-tone signal changes from a narrow Lorentzian to a broader Gaussian curve, as expected theoretically [110]. Here we use the λ-mode of the resonator as readout mode. With the coupling strength g_2 of this mode to the qubit as determined in the following section, we calculate the ac-Zeeman shift per photon $2g_2^2/\delta = 9.1\,\mathrm{MHz}$. Comparing this value to the measured shift of $\tilde{\omega}_{\mathrm{q}}$, we can calibrate the number N_2 of photons in the resonator. In Fig. 6.6**b**, $\tilde{\omega}_{\mathrm{q}}$ is plotted versus N_2 to illustrate this linear dependence. Most of the following measurements – especially for the determination of coupling strengths and the qubit gap – are carried out at a ZVA power $P_{\mathrm{rf}} = -10\,\mathrm{dBm}$, which corresponds to $N_2 \simeq 0.18$ poa in the resonator.

6.3 Circuit QED with a gradiometric tunable-gap flux qubit

After this pre-characterization of CPW resonator and flux qubit, we continue with the investigation of the coupled qubit-resonator system. With resonator transmission spectroscopy and two-tone spectroscopy, we determine gap and persistent current of the qubit as well as the coupling strengths between qubit and the resonator modes.

Determination of the qubit gap

In circuit QED experiments, the qubit gap Δ can be determined directly by a two-tone spectroscopy measurement at the qubit degeneracy point (as long as the gap does not lie too close to a resonator mode). This is a big advantage compared to the SQUID-based qubit readout in Chapter 5, where Δ is determined as a fit parameter.

With two-tone spectroscopy as described in Sec. 4.4.2, we get direct access to the dressed qubit frequency $\tilde{\omega}_\mathrm{q}$ of Eq. (3.29) in the dispersive limit. As can be seen from Eq. (3.29), the measured dressed frequency equals the bare qubit frequency, $\tilde{\omega}_\mathrm{q} \approx \omega_\mathrm{q}$, when two conditions are fulfilled: First, the photon number dependent ac-Zeeman term becomes negligible. To this end, all two-tone spectra are recorded with a low resonator input power corresponding to only $N \simeq 0.18\,\mathrm{poa}$ (cf. Sec. 6.2.3). Second, the Lamb-shift (g^2/δ at the degeneracy point) is negligible for large enough detuning. As we use the $3\lambda/2$-mode for two-tone readout, we calculate the Lamb-shift to be at most 3 MHz.

In Fig. 6.7**a** and Fig. 6.7**b**, we show a two-tone spectrum at the qubit degeneracy point, $\delta f_\mathrm{q} = 0$, for a constant bias with the external coil of $I_\mathrm{coil} = 0.10\,\mathrm{mA}$ and $I_\mathrm{coil} = 0.02\,\mathrm{mA}$, respectively. Besides the signature of the resonator modes at $\omega_2/2\pi = 4.814\,\mathrm{GHz}$ and $\omega_3/2\pi = 6.959\,\mathrm{GHz}$, we can clearly identify the qubit signal. Via Lorentzian fits to the spectra, we determine the qubit gaps $\Delta/2\pi = 5.69\,\mathrm{GHz}$ and $\Delta/2\pi = 3.68\,\mathrm{GHz}$, respectively. Another (broader) dip in the spectra at $\omega_\mathrm{s}/2\pi \simeq 6.35\,\mathrm{GHz}$ is found to be flux independent, so that we exclude a connection to the qubit.

Obviously, the qubit gap is tuned by the bias with the external coil. A systematic study of the tunable gap is presented in Sec. 6.4. Here, we exemplarily determine the qubit gap for two bias values, where we also determine the coupling strengths from transmission spectroscopy.

Determination of coupling strengths

Now, we use the recorded power transmission spectra in order to determine the coupling strengths between the qubit and different resonator modes. This is established by fitting

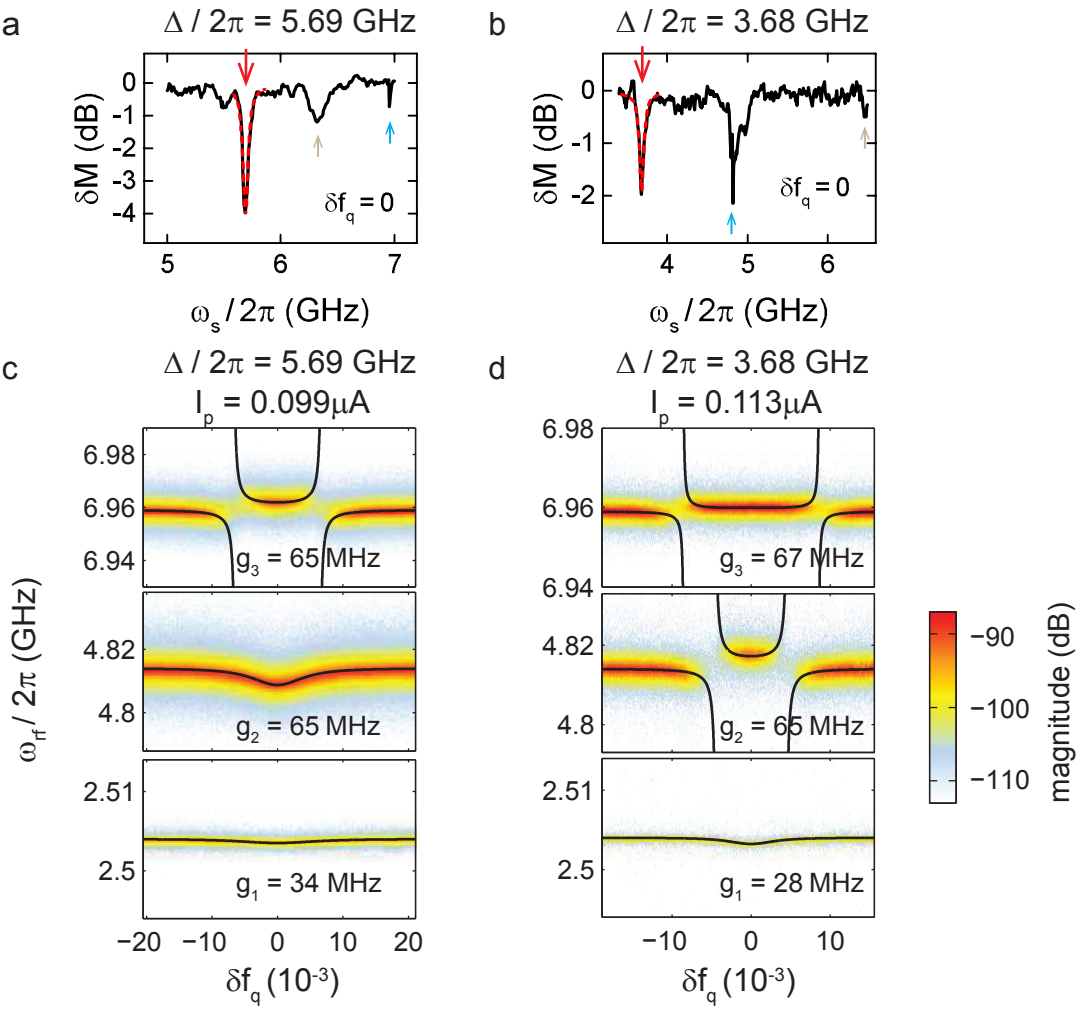

Figure 6.7: **a, b** Two-tone spectra of the qubit-resonator system at the degeneracy point (adjusted via the ε-line) for different bias $I_{\mathrm{coil}} = 0.10\,\mathrm{mA}$ (**a**) and $I_{\mathrm{coil}} = 0.02\,\mathrm{mA}$ (**b**), tuning the qubit gap. The signal of the qubit (red arrows) is fitted with a Lorentzian curve (dashed red line). Other signals in the spectra can be attributed to resonator modes (blue arrows) and to a flux-independent feature (gray arrow). **c, d** Transmission spectra of the qubit-resonator system at the same bias positions in I_{coil} as in **a, b**. The three panels show the resonator modes 1 to 3. The depicted coupling strengths g_i of each mode to the qubit and the qubit persistent current are determined by fitting the full Hamiltonian (black line).

the energy eigenvalues of the full Hamiltonian, Eq. (3.22), to the measured data in a low-power limit ($N \simeq 0.18$ poa, cf. Sec. 6.2.3).

Figure 6.7**c** shows the power transmission for the three lowest resonator modes in dependence on magnetic flux. The latter is swept by the ε-line current, while the external coil provides a constant bias $I_{\mathrm{coil}} = 0.10\,\mathrm{mA}$. The transmitted power is shown in a color-coded plot versus the resonator probe frequency ω_{rf} (vertical axis) and the magnetic frustration of the qubit. The latter is visible in each of the three resonator modes. In the spectrum of the $3\lambda/2$-mode, two anticrossings appear. These can be associated with the resonant interaction between this resonator mode and the qubit according to the theory presented in Sec. 3.4. At those positions in the $\omega_{\mathrm{q}}(f_{\mathrm{q}})$ dependency, where the qubit transition frequency matches the resonator frequency, i.e., $\omega_{\mathrm{q}}(f_{\mathrm{q}}) \approx \omega_3$, the interaction induces the formation of superposition states of qubit and resonator mode. The two other resonator modes exhibit a dip in the resonant frequency. This dip corresponds to the dispersive shift of the resonator mode due to the interaction with the (far) detuned qubit according to Eq. (3.27). The fact that the dispersive shift is much smaller for the ground mode than for the λ-mode reflects – predominantly – the larger detuning $\delta_1 = \omega_{\mathrm{q}} - \omega_1$ inversely entering the dispersive shift. As we see in the following, also the coupling g_1 of the ground mode to the qubit is much smaller than g_2, further reducing the dispersive shift. In total, it can be concluded from this first qualitative look at the transmission spectra, that they show a coupled qubit-resonator system, where the qubit gap Δ lies in between the resonator modes ω_2 and ω_3.

For a quantitative analysis we use the full qubit-resonator Hamiltonian of Eq. (3.22), which is extended for the three resonator modes to

$$\hat{H} = \frac{1}{2}\hbar\varepsilon\hat{\sigma}_z - \frac{1}{2}\hbar\Delta\hat{\sigma}_x + \sum_{n=1,2,3}\left(\hbar\omega_n\left(\hat{a}_n^\dagger\hat{a}_n + \frac{1}{2}\right) + \hbar g_n\hat{\sigma}_z\left(\hat{a}_n^\dagger + \hat{a}_n\right)\right). \tag{6.5}$$

In this context, it must be stated, that it is sufficient to treat the first three resonator modes. As can be seen in Fig. 6.3**b**, the fourth resonator mode has a current node at the qubit position and, thus, does not couple to the qubit. This is confirmed by no visible anticrossing of this mode with the qubit in its transmission spectrum (data not shown here). Any higher resonator mode is not accessible in our experiment due to the limited bandwidth of cryogenic circulators and amplifiers. Their possible interaction with the qubit is expected to be negligible due to the large detuning.

Then, the fitting routine is as follows: The resonant frequencies ω_1, ω_2 and ω_3 as well as the qubit gap Δ, which is determined independently from two-tone spectroscopy, enter as fixed input parameters. The coupling strengths g_1, g_2 and g_3 and the qubit persistent current I_{p} are the fit parameters. With these values, the Hamiltonian of Eq. (6.5) is diagonalized to calculate its eigenenergies. These are compared to the frequencies of maxi-

mum transmission in the measured spectra. The result of such a fit is shown in Fig. 6.7**c**. Obviously, the fit agrees very well with the recorded spectra. The extracted coupling strengths are $g_1/2\pi = 34\,\mathrm{MHz}$, $g_2/2\pi = 65\,\mathrm{MHz}$ and $g_3/2\pi = 65\,\mathrm{MHz}$. Furthermore, the qubit parameters are determined to $\Delta/2\pi = 5.69\,\mathrm{GHz}$ (two-tone-data) and $I_\mathrm{p} = 0.099\,\mu\mathrm{A}$ (fit).

In addition to this rather nonintuitive determination, the coupling strengths can – partly – also be extracted directly from the measurement data. For the spectrum of the λ-mode, the dispersive shift is maximal at the degeneracy point. There, the mixing angle $\theta = \arctan(\Delta/\varepsilon) = \pi/2$ and, thus, the dispersive shift $g_2^2 \sin^2\theta/\delta_2 = g_2^2/\delta_2$, neglecting the photon number dependent part. Inserting the measured shift of $\simeq 4.8\,\mathrm{MHz}$ yields $g_2 \simeq 64\,\mathrm{MHz}$ in good agreement with the fitted value.

In Fig. 6.7**d**, we show a second set of transmission spectroscopy data at $I_\mathrm{coil} = 0.02\,\mathrm{mA}$. The smaller gap (cf. Fig. 6.7**b**) leads to obvious differences in the transmission spectra. Now, also the λ-mode exhibits an anticrossing with the qubit hyperbola. A fit with the qubit Hamiltonian also matches the data and yields coupling rates $g_1/2\pi = 28\,\mathrm{MHz}$, $g_2/2\pi = 65\,\mathrm{MHz}$, $g_3/2\pi = 67\,\mathrm{MHz}$ and a persistent current $I_\mathrm{p} = 0.113\,\mu\mathrm{A}$.

Comparing the parameters for the two bias positions in Fig. 6.7**(a,c)** and Fig. 6.7**(b,d)**, the persistent current increases with decreasing gap as expected qualitatively from the dependencies $I_\mathrm{p}(\alpha)$ and $\Delta(\alpha)$ and as observed, e.g., in Fig. 5.9. However, the coupling strengths do not scale with I_p as expected from Eq. (6.1). Instead, the coupling rates g_{1-3} stay approximately constant for the different bias values, which is confirmed by further data sets (not shown here) with $I_\mathrm{p} = 0.101\,\mu\mathrm{A}$ and $I_\mathrm{p} = 0.140\,\mu\mathrm{A}$, respectively. As an in situ tunable qubit gap is a prerequisite for studying this relation between coupling rate and persistent current, we cannot find similar results in the literature. It would be interesting to study the validity of Eq. (6.1) with a tunable-gap qubit, that is optimized for a larger tunability of its persistent current (cf. Eq. (3.4) and Fig. 6.11**b**).

Strong coupling regime

The fitted coupling rates g_n are larger than the resonator loss rates κ_n determined in Sec. 6.2.1 by at least a factor of 27. The qubit decay rate γ can only be roughly estimated from the two-tone spectra in Fig. 6.7**a** and Fig. 6.7**b**. There, the FWHM of the qubit signal yields an upper bound $\gamma/2\pi \lesssim 55\,\mathrm{MHz}$, so that the conditions for strong coherent coupling are not fulfilled unambiguously. Another indication for the strong coupling regime is the observation of the vacuum Rabi splitting in the resonator transmission at an anticrossing position [111]. In Fig. 6.8, we plot two selected spectra. In the low-power limit, there is a weakly visible splitting, which becomes more prominent for higher input power, which also increases the splitting by the photon number dependent

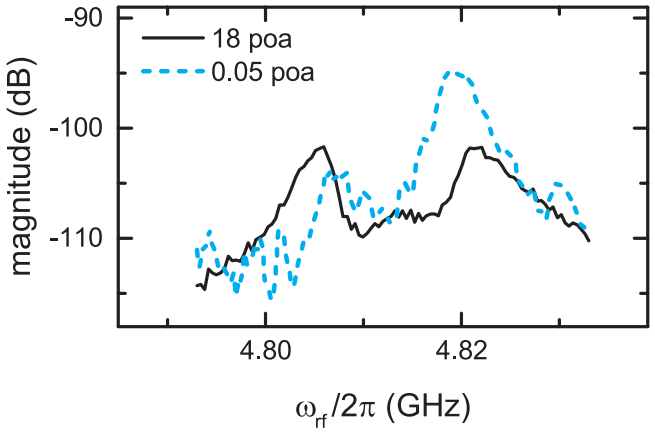

Figure 6.8: Resonator transmission magnitude plotted versus the probe frequency ω_{rf} at an anticrossing position. For higher input power (black line) two clearly separated states appear. In the low-power spectrum (blue dashed line), the vacuum Rabi splitting is still visible, indicating strong coherent coupling.

contribution. Yet, reliable results on the qubit decay rate can only be gained by a time-domain characterization. Realizing the latter was no longer content of this thesis, but is ongoing work at the WMI. First results show significantly smaller loss rates (cf. Chapter 7) compared to our estimation above, so that we can in fact conclude to reach the strong coherent coupling limit with this sample.

6.4 Tuning the qubit gap

In the previous section, it is already observed that the qubit gap changes for different bias currents in the external coil. In this subsection, we study the tunability of the qubit gap in more detail.

To this end, the experimental procedure is as follows: At a fixed value of I_{coil} we first perform a transmission measurement of the qubit-resonator system by sweeping the qubit frustration via the ε-current I_ε. In contrast to the data shown in Fig. 6.7**c** and Fig. 6.7**d**, this measurement is recorded with higher input power (14 poa) and less resolution, as we only need to determine the position of the qubit degeneracy point in the ε-current. This value $I_\varepsilon^{\mathrm{sym}}$ changes linearly with the coil current I_{coil} due to the significant gradiometer imbalance of this qubit. Next, we record a two-tone spectrum – now with low resonator power corresponding to 0.18 poa – at the qubit degeneracy point. The qubit gap is extracted from this spectrum by a Lorentzian fit.

In Fig. 6.9, we plot the determined gap values versus I_{coil} and show one example of a two-tone spectrum in the inset. The measured gap values range from $\Delta/2\pi = 2.69\,\mathrm{GHz} \ldots 5.69\,\mathrm{GHz}$. The data points appear in two groups of similar shape,

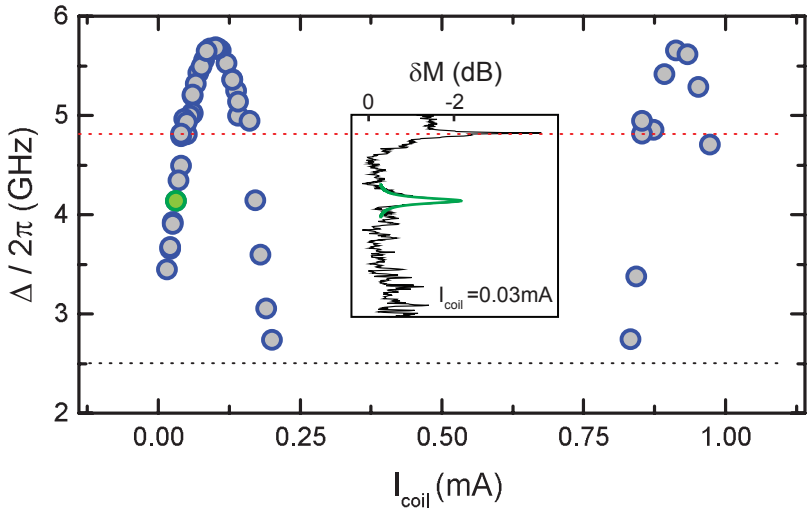

Figure 6.9: Tunability of the qubit gap by means of the external coil current frustrating the α-loop. The black and red dashed lines mark the frequencies of the first two resonator modes. The inset shows a single two-tone spectrum with Lorentzian fit (green) corresponding to the data point marked with the green circle.

which we associate with the periodicity of $\alpha(I_{\mathrm{coil}})$. Near $I_{\mathrm{coil}} = 0.2\,\mathrm{mA}$ and $I_{\mathrm{coil}} = 0.8\,\mathrm{mA}$, where one might expect the gap to be approximately $\Delta/2\pi \simeq 2\,\mathrm{GHz}$, we can still observe a weak signature of the qubit in the transmission spectra. However, the gap can no longer be determined due to the limited range of the cryogenic amplifier. In any case, the qubit is far detuned from the λ-mode of the resonator in this region. On the contrary, we can adjust the qubit gap very close to the resonant frequency of the λ-mode, maximizing the qubit-resonator interaction. With this controlled coupling/decoupling of resonator and qubit at its point of optimal coherence, we achieve the main goal for the realization of a tunable-gap gradiometric qubit inside a CPW resonator. In the following, we will analyze the tunability of the qubit gap in more detail.

Quantitative modelling of the tunable gap

Compared to the theoretically expected behavior (cf. Fig. 3.5), the general dependence $\Delta(I_{\mathrm{coil}})$ differs near the maximum observed gap values. There, the exponential increase of the gap stops. Furthermore, there is no region of abruptly vanishing qubit signal caused by a vanishing double-well potential. Thus, we conclude that no values $\alpha \leq 0.5$ are reached for this sample, meaning that the modulation depth of the α-SQUID is significantly reduced. In fact, we observe such a behavior for a test SQUID on another sample, that is fabricated with the same parameters and soon after the sample we investigate here. As one can see from the $I_{\mathrm{sw}}(f_{\mathrm{SQ}})$ curve in Fig. 6.10, the measured data cannot be approximated sufficiently well with a (vertically shifted) curve according to Eq. (2.28).

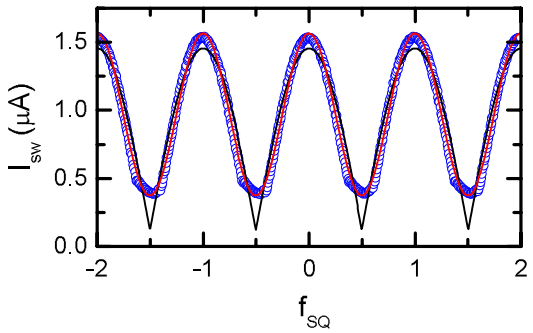

Figure 6.10: The switching current I_{sw} depending on the frustration f_{SQ} of a test SQUID measured at 500 mK. The data (blue circles) can be better described with a fit function of the type $a_1 + a_2 \cos(2\pi f_{\mathrm{SQ}})$ (fit parameters a_1, a_2, red line) than with a fit function of the type $a_1 + a_2 \left|\cos(\pi f_{\mathrm{SQ}})\right|$ (black line).

Instead, a fitting function with only a cosine term describes the real SQUID behavior much more accurately.

Thus, we assume an expression for the value α of the tunable-gap qubit of the form

$$\alpha(f_{\alpha,\mathrm{net}}) = a_1 + a_2 \cos\left(2\pi f_{\alpha,\mathrm{net}}\right) . \tag{6.6}$$

Here, $f_{\alpha,\mathrm{net}}$ denotes the net α-loop frustration as defined by Eq. (3.16) and Eq. (3.17), and a_1 and a_2 are parameters that determine the extreme values $\alpha_{\max} = a_1 + a_2$ and $\alpha_{\min} = a_1 - a_2$.

Before we fit the measurement data in Fig. 6.9 by calculating the qubit gap with the help of the expression in Eq. (6.6), we need to calibrate $f_{\alpha,\mathrm{net}}$ versus I_{coil}. This is easily achieved by adjusting the frustrations $f_{\alpha,\mathrm{net}} = \pm 0.5$, that involve minimum α and maximum Δ, to the I_{coil} values with maximum gap. We thus obtain a calibration factor

$$\zeta \equiv \frac{\partial f_{\alpha,\mathrm{net}}}{\partial I_{\mathrm{coil}}} = 1.22\,\mathrm{mA}^{-1} . \tag{6.7}$$

The fact, that this calibration factor is very similar to the calibration factor γ in Eq. (6.3), is the reason for the slightly changing qubit gap in Fig. 6.4.

The so calibrated measurement data $\Delta(f_{\alpha,\mathrm{net}})$ is shown in Fig. 6.11. together with a well matching fitting curve. For this fit, we first calculate $\alpha(f_{\alpha,\mathrm{net}})$ from Eq. (6.6) and then numerically determine Δ from a diagonalization of the qubit Hamiltonian. With four input parameters a_1, a_2, E_{J} and E_{c}, however, the fit cannot yield unambiguous results. Therefore, we set $E_{\mathrm{J}}/2\pi = 120\,\mathrm{GHz}$, which is calculated from Eq. (2.19) and Eq. (3.4) with the measured persistent current I_{p}. Here, we use the value $I_{\mathrm{p}} = 0.099\,\mu\mathrm{A}$ for maximum gap (minimum α) of Fig. 6.7**c** and, at first, estimate $\alpha_{\min} \simeq 0.55$. The latter is consistent with the obtained fit parameters $a_1 = 0.79$ and $a_2 = 0.23$, yielding

$\alpha_{\mathrm{min}} = 0.56$ and $\alpha_{\mathrm{max}} = 1.02$. The latter is very close to the design value of 1.0. The third fit parameter $E_{\mathrm{c}}/h = 1.1\,\mathrm{GHz}$ agrees very well with the value $E_{\mathrm{c}}/h \simeq 1\,\mathrm{GHz}$ derived from the Josephson capacitance measurements in Sec. 4.1.2.

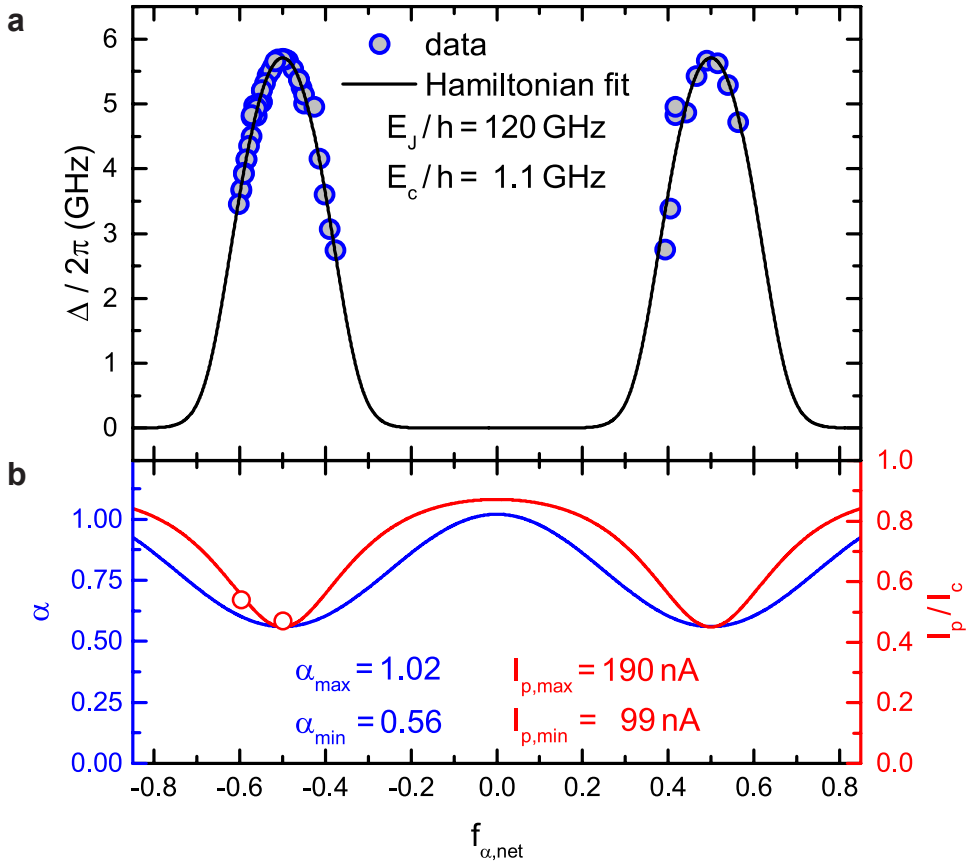

Figure 6.11: **a** Measured gap values $\Delta/2\pi$ versus the net α-loop frustration. The fit (black curve) to the data is based on the diagonalization of the qubit Hamiltonian. **b** Dependence of $\alpha(f_\alpha,\mathrm{net})$ (left blue axis) with reduced modulation depth according to Eq. (6.6) determined via the fit in **a**. Also shown is the persistent current $I_{\mathrm{p}}/I_{\mathrm{c}}(f_\alpha,\mathrm{net})$ (red right axis) calculated with Eq. (3.4). The two red circles mark the I_{p} values determined by the full Hamiltonian fits in Sec. 6.3.

6.5 Gradiometer quality

The fact that the qubit frustration can be varied over several periods with the external coil as shown in Fig. 6.4 creates doubts on the functionality of the gradiometer. Calculating the quality factor $Q_{\mathrm{grad,ex}}$ (cf. Eq. (3.21)) in the same way as in Sec. 5.2.3 and Sec. 5.3.3 is not possible here, as there is no direct measure (dc-SQUID) for the applied frustration f_{ex}. However, an alternative estimation of $Q_{\mathrm{grad,ex}}$ is realized with the calibration of the net α-loop frustration $f_{\alpha,\mathrm{net}}$ in the previous section.

Using Eq. (5.2), we calculate

$$Q_{\mathrm{grad,ex}}^{-1} = \frac{\partial \delta f_{\mathrm{imb}}}{\partial f_{\mathrm{ex}}} = \frac{\partial \delta f_{\mathrm{q}}}{\partial I_{\mathrm{coil}}} \frac{\partial I_{\mathrm{coil}}}{\partial f_{\alpha,\mathrm{net}}} \frac{\partial f_{\alpha,\mathrm{net}}}{\partial f_{\mathrm{ex}}} = \frac{\gamma}{\zeta} \frac{A_\alpha}{A_{\mathrm{tr}}} \frac{1}{1+\beta} \,. \tag{6.8}$$

Inserting the determined calibration factors γ (cf. Eq. (6.3)) and ζ [cf. Eq. (6.7)], the area ratio $A_\alpha/A_{\mathrm{tr}} = 0.18$ and the screening factor $\beta = 0.73$ (the value determined in Sec. 5.3.2 adapted to a larger cross-section of the lines for this sample), yields $Q_{\mathrm{grad,ex}} = 9.5$. This low value is very surprising, as the design of this qubit is almost unchanged compared to the one in Sec. 5.3.3 with $Q_{\mathrm{grad,ex}} = 97$. A possible explanation for this low gradiometer quality is a difference in the critical currents of the JJs of the α-SQUID, which is supported by the reduced modulation of the α-SQUID as discussed in the previous section. As the sample is still measured (cf. Chapter 7) we do not have SEM images of the qubit. Thus we can also guess, that a submicron-sized defect, e.g., a strong constriction in the line on one side of the gradiometer loop, might be the reason for this imbalance. Nevertheless, the determined quality factor means, that flux noise is still reduced by a factor of 9.5. Also, an operation of the qubit at the degeneracy point is still possible, as the imbalance of the gradiometer can be compensated by the ε-line for the full range of qubit gap from 0 up to 5.69 GHz.

6.6 Summary

In summary, we show the first successful implementation of a gradiometric tunable-gap qubit into a CPW resonator. We characterize the resonator to be well-suited for qubit readout and perform thorough calibrations of applied power and flux. We analyze the coupled qubit-resonator system and confirm to reach the regime of strong coupling. The qubit can be tuned in a controlled, reproducible way in a measured range of $\Delta/2\pi = 2.69\,\mathrm{GHz} \ldots 5.69\,\mathrm{GHz}$. We are able, e.g., to tune the qubit very close to the λ-mode of the resonator. Our calculations show, that also negligible gap values are reached, which cannot be detected by this measurement setup. Thus, the qubit can be biased to positions, where a coupling to the (λ-mode of the) resonator is effectively turned off. In total, this constitutes a valuable progress for the application of flux qubits in circuit QED experiments.

Chapter 7

Summary and outlook

This thesis deals with the fabrication and experimental characterization of gradiometric tunable-gap flux qubits and their integration into a circuit QED architecture. The basis for the realization of these advanced qubit designs is a thorough pre-characterization of the Josephson junction itself. Via the current-voltage characteristic of dc SQUIDs, we check the performance of our junctions. In particular, we determine their critical current density $j_c = 1.5 \ldots 3.5\,\mathrm{kA/cm^2}$ (dependent on the oxidation process) and specific junction capacitance $c_s \simeq 790\,\mathrm{fF/\mu m^2}$. With these parameters we can calculate the relevant energy scales E_J and E_c, which are important for modelling the tunability of the qubit gap. We first confirm these values as well as the functionality of the fabrication process by the characterization of two standard 3-JJ flux qubits. In a next step, we fabricate and characterize two fixed-gap qubits in a gradiometric layout. These systems are ideal to demonstrate the flux trapping process and the use of the on-chip ε-flux bias line for qubit frustration. Furthermore, we determine a high gradiometer quality $Q \simeq 500$ for these designs, where we reach the limits set by the accuracy of our fabrication process.

Then, we realize a gradiometric flux qubit with an in situ tunable α-SQUID. We demonstrate the tunability of the qubit gap by both the field of an external coil and an on-chip α-flux bias line. We tune the gap of a first sample between values $\Delta/2\pi \simeq 0 \ldots 5\,\mathrm{GHz}$. A second sample is optimized by fabrication to reach a high tunability of the gap, $\Delta/2\pi \simeq 0 \ldots 12\,\mathrm{GHz}$. From numerical fits we obtain a consistent set of parameters for the junction energies, the qubit persistent current and the value of α. We also investigate the gradiometer quality, which is reduced due to the implementation of a large α-SQUID to a – still sufficiently high – value $Q \simeq 90$. Moreover, spectroscopy of this qubit for different numbers of trapped flux quanta allows us to directly determine the inductance ratio $\beta = 0.52$.

Having thoroughly investigated the gradiometric tunable-gap qubit alone, we finally integrate it into a superconducting transmission line resonator, thereby forming a circuit QED architecture. Using a galvanic contact between qubit and resonator, we reach the regime of strong coherent coupling. We tune the qubit gap in a range $\Delta/2\pi \simeq 0 \ldots 5.7\,\mathrm{GHz}$.

In particular, we are thus able to adjust the qubit gap very close to the resonant frequency of a resonator mode for strong coupling. Also, the qubit gap can be tuned far away from this mode, effectively switching off the coupling. Although the gradiometer quality is found to be reduced to $Q_{\mathrm{grad,ex}} = 9.5$ for this particular sample, the qubit can still be operated at its degeneracy point via compensation with the ε-line while tuning the qubit gap. Thus, the coupling/decoupling of qubit and resonator can be performed at optimal qubit coherence. The investigation of quantitative qubit decoherence and relaxation by time-domain spectroscopy is ongoing work at the WMI.

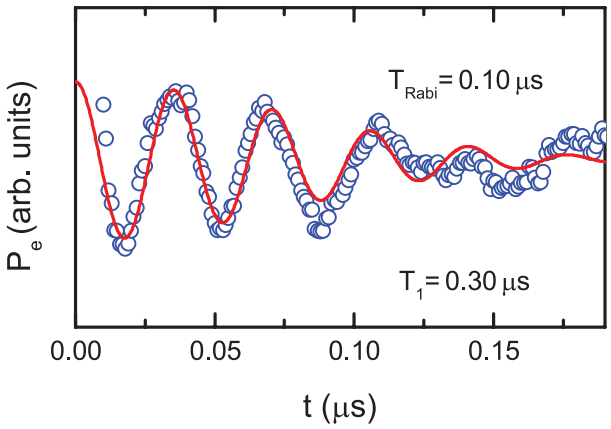

Figure 7.1: Driven Rabi oscillations of the gradiometric tunable-gap flux qubit at a temperature $T \simeq 15\,\mathrm{mK}$. Under the influence of a resonant microwave drive, the probability P_e to find the qubit in its excited state oscillates in time. These oscillation decay exponentially on a timescale T_Rabi. Data courtesy of M. Haeberlein and J. Goetz.

Meanwhile, time-domain measurements have been set up at the WMI [1]. In Fig. 7.1, we plot the result of a driven Rabi experiment [112], where the drive frequency $\omega_\mathrm{d}/2\pi$ is resonant with the qubit transition frequency at its degeneracy point, $\omega_\mathrm{d}/2\pi \approx \Delta/2\pi \simeq 3.51\,\mathrm{GHz}$. We find that the drive induces coherent oscillations of the qubit population between ground and excited state. These oscillations decay exponentially with a decay time $T_\mathrm{Rabi} \simeq 0.10\,\mu\mathrm{s}$. By a qubit relaxation measurement (data not shown), the qubit energy relaxation time $T_1 \simeq 0.30\,\mu\mathrm{s}$ is determined independently. Thus, we conclude that the qubit decay is still governed by dephasing even at the degeneracy point, at least at this particular gap frequency. A more detailed analysis via Ramsey fringes or spin echo measurements is currently in progress, but goes beyond the scope of this thesis. Nevertheless, these first results confirm the quantum coherence of our gradiometric tunable-gap flux qubit.

Good quantum coherence in combination with a tunability of the qubit gap throw the doors open to several interesting new experiments with coupled systems of flux qubits

[1] The author of this thesis gratefully acknowledges the work of M. Haeberlein and J. Goetz in setting up and performing these measurements.

and microwave resonators or transmission lines. For example, driving the gap of a flux qubit coherently coupled to a CPW resonator can be used to cool down a photon field into squeezed vacuum [113]. Increasing the coupling strength between tunable-gap flux qubit and CPW resonator into the ultrastrong coupling regime, e.g. by a longer and thinner shared line, could be applied to realize an ultrafast qubit gate [114]. Also, tunable-gap flux qubits can be operated at optimal coherence and still couple to other qubits or resonators via the qubit gap Δ instead of via ε. Thus, controllable coupling between qubits and high-fidelity quantum gates can be pursued [103].

The high degree of design tunability inherent to superconducting qubits – both by fabrication and *in situ* – make them ideal systems to realize quantum simulations [7–9]. There, quantum circuits consisting of only a few qubits and resonators are able to mimic the behavior of diverse physical systems not treatable on a classical computer. Among the large number of proposals are those suggesting the prediction of the critical temperature in superconductors, the computation of molecular energy levels [115] or the simulation of relativistic effects such as Zitterbewegung or Klein paradox [116].

Appendix A

Qubit sample parameters

Table A.1: Fabrication parameters and qubit/SQUID properties for samples with fixed gap.

qubit type	standard fixed-gap	standard fixed-gap	gradiometric fixed-gap	gradiometric fixed-gap
label	JG06B32	JG08B09	JG08B20	JGB09B16
α	0.75	0.55	0.77	0.65
area JJ [μm^2]	0.031 0.023(α)	0.020 0.012(α)	0.026 0.020(α)	0.027 0.018(α)
width Al-layer [nm]	506	506	506	506
thickness Al-layer [nm]	(40+50)	(40+50)	(40+50)	(40+50)
trap-loop area [μm^2]	-	-	20 x 15	20 x 15
qubit size [μm^2]	9.5 x 8.5	9.5 x 8.5	20 x 7.5	20 x 7.5
SQUID size [μm^2]	12 x 11.8	12 x 11.8	20 x 5	20 x 5
L-product [10^5Pa $\cdot$ s]	0.300	0.305	0.305	0.305
ox. time [min]	25:45	25:00	25:00	25:40
j_c [kA/cm^2]	2.73	3.46	3.91	2.91
R_n [Ω]	175	207	141	183
I_c^{AB} [μA]	0.82	0.69	1.01	0.78
E_j/h [GHz]	407	344	505	389
E_c/h [GHz]	1.3	1.3	1.5	1.4
$\Delta/2\pi$ [GHz]	0/(1.39)	10.76	0	5.1

Table A.2: Fabrication parameters and qubit/SQUID properties for samples with tunable gap.

qubit type	gradiometric tunable-gap	gradiometric tunable-gap	gradiometric tunable-gap + resonator
label	JG09B30	Z01B22	MS13A
α_0	1.1	0.7	1.0
area JJ [μm^2]	0.028 0.014(α)	0.028 0.01(α)	0.028 0.014(α)
width Al-layer [nm]	506	506	506
thickness Al-layer [nm]	(40+50)	(40+50)	(40+70)
trap-loop area [μm^2]	20 x 15	20 x 15	20 x 15
qubit size [μm^2]	20 x 7.5	20 x 7.5	20 x 7.5
SQUID size [μm^2]	20 x 5	20 x 5	-
α-SQUID size [μm^2]	4.5 x 12	4.5 x 12	4.5 x 12
L-product [10^5Pa $\cdot$ s]	0.305	0.285	0.36
ox. time [min]	25:40	23:30	30:00
j_c [kA/cm^2]	3.0	3.5	-
R_n [Ω]	197	86	-
I_c^{AB} [μA]	0.73	1.65	-
E_j/h [GHz]	200	800	120
E_c/h [GHz]	1.6	1.0	1.1
$\Delta/2\pi$ [GHz]	0-5	0-12	0-5.69

Bibliography

[1] T. Kadowaki and H. Nishimori, Quantum annealing in the transverse Ising model, *Phys. Rev. E* 58, 5355 (1998).

[2] M. A. Nielsen and I. L. Chuang, *Quantum Computation and Quantum Information (Cambridge Series on Information and the Natural Sciences)*, Cambridge University Press, 1 edn. (2004).

[3] S. W. Shin, G. Smith, J. A. Smolin, and U. Vazirani, How "Quantum" is the D-Wave Machine?, *ArXiv e-prints* (2014).

[4] T. F. Rønnow, Z. Wang, J. Job, S. Boixo, S. V. Isakov, D. Wecker, J. M. Martinis, D. A. Lidar, and M. Troyer, Defining and detecting quantum speedup, *Science* 345, 420 (2014).

[5] R. J. Schoelkopf and S. M. Girvin, Wiring up quantum systems, *Nature* 451, 664 (2008).

[6] A. Wallraff, D. I. Schuster, A. Blais, L. Frunzio, R.-S. Huang, J. Majer, S. Kumar, S. M. Girvin, and R. J. Schoelkopf, Strong coupling of a single photon to a superconducting qubit using circuit quantum electrodynamics, *Nature* 431, 162 (2004).

[7] R. Feynman, Simulating physics with computers, *International Journal of Theoretical Physics* 21, 467 (1982), 10.1007/BF02650179.

[8] I. M. Georgescu, S. Ashhab, and F. Nori, Quantum simulation, *Rev. Mod. Phys.* 86, 153 (2014).

[9] A. A. Houck, H. E. Tureci, and J. Koch, On-chip quantum simulation with superconducting circuits, *Nat Phys* 8, 292 (2012).

[10] J. M. Martinis, M. H. Devoret, and J. Clarke, Experimental tests for the quantum behavior of a macroscopic degree of freedom: The phase difference across a Josephson junction, *Phys. Rev. B* 35, 4682 (1987).

[11] Y. Nakamura, Y. Pashkin, and J. S. Tsai, Coherent control of macroscopic quantum states in a single-Cooper-pair box, *Nature* 398, 786 (1999).

[12] J. M. Fink, M. Göppl, M. Baur, R. Bianchetti, P. J. Leek, A. Blais, and A. Wallraff, Climbing the Jaynes-Cummings ladder and observing its $\sqrt{n}$ nonlinearity in a cavity QED system, *Nature* 454, 315 (2008).

[13] J. Majer, J. M. Chow, J. M. Gambetta, J. Koch, B. R. Johnson, J. A. Schreier, L. Frunzio, D. I. Schuster, A. A. Houck, A. Wallraff, A. Blais, M. H. Devoret, S. M. Girvin, and R. J. Schoelkopf, Coupling superconducting qubits via a cavity bus, *Nature* 449, 443 (2007).

[14] R. H. Koch, D. P. DiVincenzo, and J. Clarke, Model for $1/f$ Flux Noise in SQUIDs and Qubits, *Phys. Rev. Lett.* 98, 267003 (2007).

[15] M. Hofheinz, E. M. Weig, M. Ansmann, R. C. Bialczak, E. Lucero, M. Neeley, A. D. O'Connell, H. Wang, J. M. Martinis, and A. N. Cleland, Generation of Fock states in a superconducting quantum circuit, *Nature* 454, 310 (2008).

[16] J. M. Martinis, M. H. Devoret, and J. Clarke, Energy-Level Quantization in the Zero-Voltage State of a Current-Biased Josephson Junction, *Phys. Rev. Lett.* 55, 1543 (1985).

[17] M. H. Devoret, A. Wallraff, and J. M. Martinis, Superconducting Qubits: A Short Review (2004).

[18] V. E. Manucharyan, J. Koch, L. I. Glazman, and M. H. Devoret, Fluxonium: Single Cooper-Pair Circuit Free of Charge Offsets, *Science* 326, 113 (2009).

[19] I. Chiorescu, P. Bertet, K. Semba, Y. Nakamura, C. J. P. M. Harmans, and J. E. Mooij, Coherent dynamics of a flux qubit coupled to a harmonic oscillator, *Nature* 431, 159 (2004).

[20] J. E. Mooij, T. Orlando, L. Levitov, L. Tian, C. H. van der Wal, and S. Lloyd, Josephson Persistent-Current Qubit, *Science* 285, 1036 (1999).

[21] I. Chiorescu, Y. Nakamura, C. J. P. M. Harmans, and J. E. Mooij, Coherent Quantum Dynamics of a Superconducting Flux Qubit, *Science* 299, 1869 (2003).

[22] T. P. Orlando, J. E. Mooij, L. Tian, C. H. van der Wal, L. S. Levitov, S. Lloyd, and J. J. Mazo, Superconducting persistent-current qubit, *Phys. Rev. B* 60, 15398 (1999).

[23] J. Johansson, S. Saito, T. Meno, H. Nakano, M. Ueda, K. Semba, and H. Takayanagi, Vacuum Rabi Oscillations in a Macroscopic Superconducting Qubit *LC* Oscillator System, *Phys. Rev. Lett.* 96, 127006 (2006).

[24] O. Astafiev, K. Inomata, A. O. Niskanen, T. Yamamoto, Y. A. Pashkin, Y. Nakamura, and J. S. Tsai, Single artificial-atom lasing, *Nature* 449, 588 (2007).

[25] F. Deppe, M. Mariantoni, E. P. Menzel, A. Marx, S. Saito, K. Kakuyanagi, H. Tanaka, T. Meno, K. Semba, H. Takayanagi, E. Solano, and R. Gross, Two-photon probe of the Jaynes-Cummings model and controlled symmetry breaking in circuit QED, *Nat Phys* 4, 686 (2008).

[26] T. Niemczyk, F. Deppe, E. P. Menzel, M. J. Schwarz, H. Huebl, F. Hocke, M. Häberlein, M. Danner, E. Hoffmann, A. Baust, E. Solano, J. J. Garcia-Ripoll, A. Marx, and R. Gross, Selection rules in a strongly coupled qubit-resonator system, *ArXiv e-prints* (2011).

[27] L. Steffen, Y. Salathe, M. Oppliger, P. Kurpiers, M. Baur, C. Lang, C. Eichler, G. Puebla-Hellmann, A. Fedorov, and A. Wallraff, Deterministic quantum teleportation with feed-forward in a solid state system, *Nature* 500, 319 (2013).

[28] L. DiCarlo, J. M. Chow, J. M. Gambetta, L. S. Bishop, B. R. Johnson, D. I. Schuster, J. Majer, A. Blais, L. Frunzio, S. M. Girvin, and R. J. Schoelkopf, Demonstration of two-qubit algorithms with a superconducting quantum processor, *Nature* 460, 240 (2009).

[29] A. Dewes, R. Lauro, F. R. Ong, V. Schmitt, P. Milman, P. Bertet, D. Vion, and D. Esteve, Quantum speeding-up of computation demonstrated in a superconducting two-qubit processor, *Phys. Rev. B* 85, 140503 (2012).

[30] A. Dewes, F. R. Ong, V. Schmitt, R. Lauro, N. Boulant, P. Bertet, D. Vion, and D. Esteve, Characterization of a Two-Transmon Processor with Individual Single-Shot Qubit Readout, *Phys. Rev. Lett.* 108, 057002 (2012).

[31] M. D. Reed, L. DiCarlo, S. E. Nigg, L. Sun, L. Frunzio, S. M. Girvin, and R. J. Schoelkopf, Realization of three-qubit quantum error correction with superconducting circuits, *Nature* 482, 382 (2012).

[32] J. Clarke and F. K. Wilhelm, Superconducting quantum bits, *Nature* 453, 1031 (2008).

[33] A. Fedorov, A. K. Feofanov, P. Macha, P. Forn-Diaz, C. J. P. M. Harmans, and J. E. Mooij, Strong Coupling of a Quantum Oscillator to a Flux Qubit at Its Symmetry Point, *Phys. Rev. Lett.* 105, 060503 (2010).

[34] T. Niemczyk, F. Deppe, H. Huebl, E. P. Menzel, F. Hocke, M. J. Schwarz, J. J. Garcia-Ripoll, D. Zueco, T. Hummer, E. Solano, A. Marx, and R. Gross, Circuit quantum electrodynamics in the ultrastrong-coupling regime, *Nat Phys* 6, 772 (2010).

[35] P. Forn-Diaz, J. Lisenfeld, D. Marcos, J. J. Garcia-Ripoll, E. Solano, C. J. P. M. Harmans, and J. E. Mooij, Observation of the Bloch-Siegert Shift in a Qubit-Oscillator System in the Ultrastrong Coupling Regime, *Phys. Rev. Lett.* 105, 237001 (2010).

[36] P. Forn Diaz, *Superconducting qubits and quantum resonators*, Ph.D. thesis, TU Delft (2010).

[37] F. G. Paauw, A. Fedorov, C. J. P. M. Harmans, and J. E. Mooij, Tuning the Gap of a Superconducting Flux Qubit, *Phys. Rev. Lett.* 102, 090501 (2009).

[38] A. Fedorov, P. Macha, A. K. Feofanov, C. J. P. M. Harmans, and J. E. Mooij, Tuned Transition from Quantum to Classical for Macroscopic Quantum States, *Phys. Rev. Lett.* 106, 170404 (2011).

[39] X. Zhu, A. Kemp, S. Saito, and K. Semba, Coherent operation of a gap-tunable flux qubit, *Applied Physics Letters* 97, 102503 (2010).

[40] S. Poletto, F. Chiarello, M. G. Castellano, J. Lisenfeld, A. Lukashenko, C. Cosmelli, G. Torrioli, P. Carelli, and A. V. Ustinov, Coherent oscillations in a superconducting tunable flux qubit manipulated without microwaves, *New Journal of Physics* 11, 013009 (10pp) (2009).

[41] S. Gustavsson, J. Bylander, F. Yan, W. D. Oliver, F. Yoshihara, and Y. Nakamura, Noise correlations in a flux qubit with tunable tunnel coupling, *Phys. Rev. B* 84, 014525 (2011).

[42] X. Zhu, S. Saito, A. Kemp, K. Kakuyanagi, S.-i. Karimoto, H. Nakano, W. J. Munro, Y. Tokura, M. S. Everitt, K. Nemoto, M. Kasu, N. Mizuochi, and K. Semba, Coherent coupling of a superconducting flux qubit to an electron spin ensemble in diamond, *Nature* 478, 221 (2011).

[43] J. Bardeen, L. N. Cooper, and J. R. Schrieffer, Microscopic Theory of Superconductivity, *Phys. Rev.* 106, 162 (1957).

[44] J. Bardeen, L. N. Cooper, and J. R. Schrieffer, Theory of Superconductivity, *Phys. Rev.* 108, 1175 (1957).

[45] R. Doll and M. Näbauer, Experimental proof of magnetic flux quantization in a superconducting ring, *Phys. Rev. Lett.* 7, 51 (1961).

[46] B. S. Deaver and W. M. Fairbank, Experimental Evidence for quantized flux in superconducting cylinders, *Phys. Rev. Lett.* 7, 43 (1961).

[47] R. W. Cohen and B. Abeles, Superconductivity in Granular Aluminum Films, *Phys. Rev.* 168, 444 (1968).

[48] K. Steinberg, M. Scheffler, and M. Dressel, Quasiparticle response of superconducting aluminum to electromagnetic radiation, *Phys. Rev. B* 77, 214517 (2008).

[49] C. N. Lau, N. Markovic, M. Bockrath, A. Bezryadin, and M. Tinkham, Quantum Phase Slips in Superconducting Nanowires, *Phys. Rev. Lett.* 87, 217003 (2001).

[50] J. E. Mooij and C. J. P. M. Harmans, Phase-slip flux qubits, *New Journal of Physics* 7, 219 (2005).

[51] D. E. McCumber and B. I. Halperin, Time Scale of Intrinsic Resistive Fluctuations in Thin Superconducting Wires, *Phys. Rev. B* 1, 1054 (1970).

[52] B. Josephson, Possible new effects in superconductive tunnelling, *Physics Letters* 1, 251 (1962).

[53] D. E. McCumber, Effect of ac Impedance on dc Voltage-Current Characteristics of Superconductor Weak-Link Junctions, *Journal of Applied Physics* 39, 3113 (1968).

[54] W. C. Stewart, Current-voltage characteristics of Josephson junctions, *Applied Physics Letters* 12, 277 (1968).

[55] V. Ambegaokar and A. Baratoff, Tunneling Between Superconductors, *Phys. Rev. Lett.* 10, 486 (1963).

[56] R. Kleiner, D. Koelle, F. Ludwig, and J. Clarke, Superconducting quantum interference devices: State of the art and applications, *Proceedings of the IEEE* 92, 1534 (2004).

[57] J. Clarke and A. I. Braginski, *The SQUID Handbook. Vol. 2, Applications of SQUIDs and SQUID Systems*, vol. 2, Wiley-VCH (2006).

[58] J. Clarke and A. I. Braginski, *The SQUID Handbook. Vol. 1, Fundamentals and Technology of SQUIDS and SQUID Systems*, vol. 1, Wiley-VCH (2004).

[59] R. Gross and A. Marx, *Lecture Notes on "Applied Superconductivity"* (2010).

[60] B. Yurke and J. S. Denker, Quantum network theory, *Phys. Rev. A* 29, 1419 (1984).

[61] M. H. Devoret, *Quantum Fluctuations in Electrical Circuits*, Les Houches Session LXIII, Elsevier, Amsterdam (1997).

[62] M. Goeppl, A. Fragner, M. Baur, R. Bianchetti, S. Filipp, J. M. Fink, P. J. Leek, G. Puebla, L. Steffen, and A. Wallraff, Coplanar waveguide resonators for circuit quantum electrodynamics, *Journal of Applied Physics* 104, 113904 (2008).

[63] M. J. Schwarz, J. Goetz, Z. Jiang, T. Niemczyk, F. Deppe, A. Marx, and R. Gross, Gradiometric flux qubits with a tunable gap, *New Journal of Physics* 15, 045001 (2013).

[64] Y. Shimazu, Y. Saito, and Z. Wada, Spectroscopy of Josephson-Junction Flux Qubit with Controllable Energy Gap, *Journal of the Physical Society of Japan* 78, 064708 (2009).

[65] Y. Shimazu, Y. Saito, and Z. Wada, Characterization of double-loop four-Josephson-junction flux qubit, *Physica C: Superconductivity* 469, 1608 (2009).

[66] Y. Shimazu, Tunability of Excited-State Energy Levels of Four-Josephson-Junction Circuit in Crossover from Double-Well to Single-Well Potential, *Journal of the Physical Society of Japan* 80, 054701 (2011).

[67] E. Jaynes and F. Cummings, Comparison of quantum and semiclassical radiation theories with application to the beam maser, *Proceedings of the IEEE* 51, 89 (1963).

[68] D. I. Schuster, *Circuit Quantum Electrodynamics*, Ph.D. thesis, Yale University (2007).

[69] A. Blais, R.-S. Huang, A. Wallraff, S. M. Girvin, and R. J. Schoelkopf, Cavity quantum electrodynamics for superconducting electrical circuits: An architecture for quantum computation, *Phys. Rev. A* 69, 062320 (2004).

[70] P. Grangier, J. A. Levenson, and J.-P. Poizat, Quantum non-demolition measurements in optics, *Nature* 396, 537 (1998).

[71] G. Nogues, A. Rauschenbeutel, S. Osnaghi, M. Brune, J. M. Raimond, and S. Haroche, Seeing a single photon without destroying it, *Nature* 400, 239 (1999).

[72] S. Gleyzes, S. Kuhr, C. Guerlin, J. Bernu, S. Deleglise, U. Busk Hoff, M. Brune, J.-M. Raimond, and S. Haroche, Quantum jumps of light recording the birth and death of a photon in a cavity, *Nature* 446, 297 (2007).

[73] C. Guerlin, J. Bernu, S. Deleglise, C. Sayrin, S. Gleyzes, S. Kuhr, M. Brune, J.-M. Raimond, and S. Haroche, Progressive field-state collapse and quantum non-demolition photon counting, *Nature* 448, 889 (2007).

[74] B. R. Johnson, M. D. Reed, A. A. Houck, D. I. Schuster, L. S. Bishop, E. Ginossar, J. M. Gambetta, L. DiCarlo, L. Frunzio, S. M. Girvin, and R. J. Schoelkopf, Quantum non-demolition detection of single microwave photons in a circuit, *Nat Phys* 6, 663 (2010).

[75] T. Niemczyk, *From strong to ultrastrong coupling in circuit QED architectures*, Ph.D. thesis, TU München (2011).

[76] J. Goetz, *Gradiometric flux quantum bits with tunable tunnel coupling*, Master's thesis, TU München (2011).

[77] D. M. Müller, Atomic Force Microscopy on Nano Scale Josephson Contacts, Bachelor's thesis, TU München (2013).

[78] E. Xie, *Optimized fabrication process for nanoscale Josephson junctions used in superconducting quantum circuits*, Master's thesis, TU München (2013).

[79] M. Goeppl, *Quantenelektronik mit supraleitenden Bauelementen - Herstellung und Charakterisierung von Fluss-Qubits*, Master's thesis, TU München (2006).

[80] G. Wild, *Josephson Junctions with Ferromagnetic Interlayer*, Ph.D. thesis, TU München (2011).

[81] F. Deppe, S. Saito, H. Tanaka, and H. Takayanagi, Determination of the capacitance of nm scale Josephson junctions, *Journal of Applied Physics* 95, 2607 (2004).

[82] D. B. Tuckerman and J. H. Magerlein, Resonances in symmetric Josephson interferometers, *Applied Physics Letters* 37, 241 (1980).

[83] J. Magerlein, Specific capacitance of Josephson tunnel junctions, *Magnetics, IEEE Transactions on* 17, 286 (1981).

[84] M. Maezawa, M. Aoyagi, H. Nakagawa, I. Kurosawa, and S. Takada, Specific capacitance of Nb/AlOx/Nb Josephson junctions with critical current densities in the range of 0.1-18 kA/cm2, *Applied Physics Letters* 66, 2134 (1995).

[85] H. H. Zappe, Minimum current and related topics in Josephson tunnel junction devices, *Journal of Applied Physics* 44, 1371 (1973).

[86] H. Warlimont, Ceramics, in W. Martienssen and H. Warlimont (editors), *Springer Handbook of Condensed Matter and Materials Data*, 431–476, Springer Berlin Heidelberg (2005).

[87] J. B. Majer, J. R. Butcher, and J. E. Mooij, Simple phase bias for superconducting circuits, *Applied Physics Letters* 80, 3638 (2002).

[88] T. Orlando, *Foundations of Applied Suprconductivity*, Addison-Wesley (1991).

[89] A. J. Annunziata, D. F. Santavicca, L. Frunzio, G. Catelani, M. J. Rooks, A. Frydman, and D. E. Prober, Tunable superconducting nanoinductors, *Nanotechnology* 21, 445202 (2010).

[90] F. Terman, *Radio Engineers' Handbook*, Mc Graw-Hill (1950).

[91] H. Tanaka, S. Saito, H. Nakano, K. Semba, M. Ueda, and H. Takayanagi, Single-Shot Readout of Macroscopic Quantum Superposition State in a Superconducting Flux Qubit, *Science And Technology* 1, 5 (2004).

[92] C. H. van der Wal, *Quantum Superpositions of Persistent Josephson Currents*, Ph.D. thesis, TU Delft (2001).

[93] C. H. van der Wal, A. C. J. ter Haar, F. K. Wilhelm, R. N. Schouten, C. J. P. M. Harmans, T. P. Orlando, S. Lloyd, and J. E. Mooij, Quantum Superposition of Macroscopic Persistent-Current States, *Science* 290, 773 (2000).

[94] M. A. Araque Caballero, *A Setup for Quantum Signal Detection in a Circuit QED Architecture.*, Master's thesis, TU München (2008).

[95] T. Losinger, *Time-domain control of light-matter interaction with superconducting circuits*, Master's thesis, TU München (2012).

[96] E. Xie, Impedance matching of metal powder filters for experiments with superconducting flux quantum bits, Bachelor's thesis, TU München (2011).

[97] T. Ramirez, Optimization of impedance matched stainless steel powder filters, Bachelor's thesis, TU München (2011).

[98] A. Lukashenko and A. V. Ustinov, Improved powder filters for qubit measurements, *Review of Scientific Instruments* 79, 014701 (2008).

[99] A. Fukushima, A. Sato, A. Iwasa, Y. Nakamura, T. Komatsuzaki, and Y. Sakamoto, Attenuation of microwave filters for single-electron tunneling experiments, *IEEE Transactions on Instrumentation and Measurement* 46, 289 (1997).

[100] F. P. Milliken, J. R. Rozen, G. A. Keefe, and R. H. Koch, 50 Ohm characteristic impedance low-pass metal powder filters, *Review of Scientific Instruments* 78, 024701 (2007).

[101] K. Bladh, D. Gunnarsson, E. Hürfeld, S. Devi, C. Kristoffersson, B. Smalander, S. Pehrson, T. Claeson, P. Delsing, and M. Taslakov, Comparison of cryogenic filters for use in single electronics experiments, *Review of Scientific Instruments* 74, 1323 (2003).

[102] E. P. Menzel, *Propagating Quantum Microwaves: Dual-path State Reconstruction and Path Entanglement*, Ph.D. thesis, TU München (2013).

[103] A. J. Kerman and W. D. Oliver, High-Fidelity Quantum Operations on Superconducting Qubits in the Presence of Noise, *Phys. Rev. Lett.* 101, 070501 (2008).

[104] H. P. Gürtner, Interference Effects on Superconducting Coplanar Waveguide Structures, Bachelor's thesis, TU München (2013).

[105] J. Goetz, private communication.

[106] J. Gao, M. Daal, A. Vayonakis, S. Kumar, J. Zmuidzinas, B. Sadoulet, B. A. Mazin, P. K. Day, and H. G. Leduc, Experimental evidence for a surface distribution of two-level systems in superconducting lithographed microwave resonators, *Applied Physics Letters* 92, 152505 (2008).

[107] J. M. Sage, V. Bolkhovsky, W. D. Oliver, B. Turek, and P. B. Welander, Study of loss in superconducting coplanar waveguide resonators, *Journal of Applied Physics* 109, 063915 (2011).

[108] J. M. Martinis, K. B. Cooper, R. McDermott, M. Steffen, M. Ansmann, K. D. Osborn, K. Cicak, S. Oh, D. P. Pappas, R. W. Simmonds, and C. C. Yu, Decoherence in Josephson Qubits from Dielectric Loss, *Phys. Rev. Lett.* 95, 210503 (2005).

[109] C. M. Quintana, A. Megrant, Z. Chen, A. Dunsworth, B. Chiaro, R. Barends, B. Campbell, Y. Chen, I.-C. Hoi, E. Jeffrey, J. Kelly, J. Y. Mutus, P. J. J. O'Malley, C. Neill, P. Roushan, D. Sank, A. Vainsencher, J. Wenner, T. C. White, A. N. Cleland, and J. M. Martinis, Characterization and reduction of microfabrication-induced decoherence in superconducting quantum circuits, *Applied Physics Letters* 105, 062601 (2014).

[110] J. Gambetta, A. Blais, D. I. Schuster, A. Wallraff, L. Frunzio, J. Majer, M. H. Devoret, S. M. Girvin, and R. J. Schoelkopf, Qubit-photon interactions in a cavity:

Measurement-induced dephasing and number splitting, *Phys. Rev. A* 74, 042318 (2006).

[111] A. A. Abdumalikov, O. Astafiev, Y. Nakamura, Y. A. Pashkin, and J. Tsai, Vacuum Rabi splitting due to strong coupling of a flux qubit and a coplanar-waveguide resonator, *Phys. Rev. B* 78, 180502 (2008).

[112] C. Cohen-Tannoudji, B. Diu, and F. Laloe, *Quantum Mechanics*, no. 2 in Quantum Mechanics, John Wiley & Sons (2006).

[113] D. Porras and J. J. Garcia-Ripoll, Shaping an Itinerant Quantum Field into a Multimode Squeezed Vacuum by Dissipation, *Phys. Rev. Lett.* 108, 043602 (2012).

[114] G. Romero, D. Ballester, Y. M. Wang, V. Scarani, and E. Solano, Ultrafast Quantum Gates in Circuit QED, *Phys. Rev. Lett.* 108, 120501 (2012).

[115] A. Aspuru-Guzik, A. D. Dutoi, P. J. Love, and M. Head-Gordon, Simulated Quantum Computation of Molecular Energies, *Science* 309, 1704 (2005).

[116] R. Gerritsma, G. Kirchmair, F. Zahringer, E. Solano, R. Blatt, and C. F. Roos, Quantum simulation of the Dirac equation, *Nature* 463, 68 (2010).

List of publications

- M. J. Schwarz, J. Goetz, Z. Jiang, T. Niemczyk, F. Deppe, A. Marx, and R. Gross.Gradiometric flux qubits with tunable gap. *New Journal of Physics* **15**, 045001 (2013)

- T. Niemczyk, F. Deppe, H. Huebl, E. P. Menzel, F. Hocke, M. J. Schwarz, J. J. Garcia-Ripoll, D. Zueco, T. Hümmer, E. Solano, A. Marx, and R. Gross. Circuit quantum electrodynamics in the ultrastrong-coupling regime. *Nature Physics* **6**, 772-776 (2010)

- T. Niemczyk, F. Deppe, E. P. Menzel, M. J. Schwarz, H. Huebl, M. Häberlein, F. Hocke, M. Danner, A. Baust, E. Hoffmann, J. J. Garcia-Ripoll, E. Solano, A. Marx, and R. Gross. Selection rules in a strongly coupled qubit-resonator system. *arXiv preprint*, arXiv:1107.0810 (2011)

- A. Baust, E. Hoffmann, M. Haeberlein, M. J. Schwarz, P. Eder, E. P. Menzel, K. Fedorov, J. Goetz, F. Wulschner, E. Xie, L. Zhong, F. Quijandria, B. Peropadre, D. Zueco, J.-J. Garcia Ripoll, E. Solano, F. Deppe, A. Marx, and R. Gross. Tunable and Switchable Coupling Between Two Superconducting Resonators. *arXiv preprint*, arXiv:1405.1969, submitted for publication (2014)

Danksagung

Ich möchte mich herzlich bei all denen bedanken, die durch ihre fachliche Unterstützung diese Arbeit ermöglicht haben und auf persönlicher Ebene das "Leben am WMI" so angenehm gestaltet haben. Insbesondere danke ich: Prof. Rudolf Gross, der diese Doktorarbeit ermöglicht und betreut und immer wieder mit seiner Erfahrung inspiriert hat; Dr. Achim Marx und Dr. Frank Deppe für ihre alltägliche Unterstützung und vor allem für die so hilfreiche Korrektur dieser Arbeit; Dr. Tomasz Niemczyk, der als erster meine Begeisterung für qubits geweckt und mich vor allem bei deren Herstellung hervorragend angelernt hat; Jan Goetz, der mit enormen Einsatz während seiner Diplomarbeit und der weiteren guten Zusammenarbeit viel zu dieser Arbeit beigetragen hat; Zhaohai Jiang, der mir ebenfalls als Diplomand eine großartige Unterstützung gewesen ist; Max Haeberlein, für alle seine Ideen und Hilfen bei Fabrikation, IT und bei der Zusammenarbeit am Qubit-Kryo; Alex Baust für seine wichtige Hilfe bei Messtechnik und vor allem für die unterhaltsame Zeit im Büro; Dr. Elisabeth Hoffmann und Dr. Georg Wild vor allem für ihre Hilfe beim Bedienen der Kryostaten; Dr. Edwin Menzel für diverse Hilfestellungen vor allem zu Messtechnik; Dr. Hans Huebl für hilfreiche Diskussionen und Vorschläge; allen weiteren aktuellen und früheren Doktoranden und Studenten für Hilfen und die nette Atmosphäre; Thomas Brenninger für seinen unermüdlichen Einsatz in der Dünnschichttechnik; Dr. Christian Probst für seine Hilfe bei Tieftemperaturtechnik und der Konstruktion des Kryostaten; der mechanischen Werkstatt, Helmut Thies, Robert Müller, Georg Nitschke, Julius Klaus, Christian Reichlmeier und Alexander Rößl für die gute Zusammenarbeit beim Bau des Kryostaten; Ulrich Guggenberger für die kompetente Reparatur diverser Elektronik. Sepp Hoess für Hilfe bei der Konstruktion; der Helium-Mannschaft Peter Binkert, Jan Naundorf und Harald Schwaiger für (auch kurzfristige) Helium-Bereitstellung; Astrid Habel und Karen Helm-Knapp für optische Lithografie und die Materialversorgung im Reinraum; Dr. Matthias Opel und Dieter Guratzsch für IT support; Dr. Karl Neumaier und Dr. Kurt Uhlig für Hilfen bei der Tieftemperaturtechnik; Siegfried Wanninger für die Elektrik der Batterieversorgung der Messgeräte; Emel Dönertas für Administratives; den Reinigungskräften Sybilla Plöderl und Maria Botta; sowie allen, die ich vergessen habe. Zuletzt gilt mein großer Dank meinen Eltern und meiner Familie, meinen guten Freunden sowie meiner lieben Frau Michaela für ihre Unterstützung in allen Bereichen außerhalb der Physik.